EPFL

Thèse n°8721

Experimental investigation and analysis of sequential jet impingement concepts for enhanced turbine cooling

Présentée le 19 novembre 2021

Faculté des sciences et techniques de l'ingénieur
Laboratoire de conception mécanique appliquée
Programme doctoral en énergie

pour l'obtention du grade de Docteur ès Sciences

par

Michele GAFFURI

Acceptée sur proposition du jury

Prof. S. Haussener, présidente du jury
Prof. J. A. Schiffmann, Dr P. Ott, directeurs de thèse
Prof. B. Weigand, rapporteur
Dr M. Schnieder, rapporteur
Dr J. Van Herle, rapporteur

École
polytechnique
fédérale
de Lausanne

2021

Acknowledgements

Working on a PhD Thesis is considered a solitary endeavor, but the study presented hereafter would not have been possible without the help and support of many people and institutions, which I would like to publicly acknowledge here.

First and foremost, I would like to thank Dr. Peter Ott, who as been my thesis director for 4 years until his retirement, and thesis co-director for the last few months. Peter devoted an incredible amount of time to my study, discussing results, proposing new ideas, and finding creative solutions to problems in the experimental setup, all the while letting me run the study with the required independence. I am truly honored to have been a PhD candidate in his lab. I would also like to thank Prof. Jürg Schiffmann, who stepped in to fill the role of thesis director after Peter retirement, and gave much support for the final stages of the thesis. Many thanks to Prof. Alexandros Terzis, who introduced me to the experimental part of this work, and brought me up to speed in the first year of the project. This work would not have been possible without the knowledge he acquired and the facilities he developed during his thesis.

I would also thank the industrial partner of this project, Ansaldo Energia Switzerland, and in particular Dr. Marc Henze, Dr. Stefan Retzko, Dr. Shailendra Naik and Dr. Martin Schnieder for their precious collaboration and for the information they provided on industrial scale gas turbines. I would like to acknowledge the financial support of the Swiss Federal Office of Energy under the Pilot and Demonstration program. I am grateful to the jury committee who took time to read and evaluate my work, and gave suggestions to make the final version of this report more complete. Many thanks also to the team at the Institute of Aerospace Thermodynamics (ITLR) of the University of Stuttgart, and in particular to Prof. Jens von Wolfersdorf and Prof. Bernhard Weigand.

This work would not have been possible without the technical expertise of the people at the mechanical engineering workshop (ATME), in particular Marc Jeanneret and Laurent Chevalley, who helped with the design of the test models, as well as Christophe Zurmühle, Romain Baumer, and Nicolas Jaunin, who were always ready to help in case of "mechanical" problems with the facility or for last minute modifications. Likewise, many thanks to the team at the Additive Manufacturing Workshop (AFA), who manufactured some of the heat transfer enhancement devices investigated in this study. Of course, a big thank you goes to the team of the group of thermal turbomachinery: to Dr. Angelo Casagrande, Dr. Pénélope Leyland, as well as to Margarita Jotterand Jimenez and Petra

Bendel for their help in the day to day activities of the lab.
During the course of the thesis, several Master or semester projects have taken place; all students did solid work, parts of which have been useful for the experimental investigations: Francesco Bardi, Hermence Dewintre (École des Mines de Nancy), Thibault Macherel, Tim Dosso, and Julian Schmid (University of Stuttgart).
Many people, too many to recall here exhaustively, supported me during these 4 years. Of course, I would like to thank my girlfriend Jane, who was always beside me and encouraging to go on (and finish!). Without her I would probably not have made it this far. Her family was a big support also, and really became a second family for me during this time. I would also tell my gratitude to my family, my parents, my brother and sisters and their families. Although (relatively) far, their warm support was felt every step of the way. Last but not least, I would like to thank my friends Francesco, Mattia, Vasco, as well as the members of the penguin collective. Every minute spent with you is a moment of joy.

Lausanne, October 26, 2021 Michele Gaffuri

Abstract

With the future decarbonization of the electricity production, gas turbines will be an important tool for the stabilization of the electricity grid by meeting the peak of energy demand using zero-carbon fuels like synthetic gas and hydrogen. The combustion temperature in gas turbines has increased steadily over the years in a quest to increase the thermal efficiency of the machine, so that in modern gas turbines active cooling of blades and vanes is required to ensure safe operation. The need for cooling is exacerbated by the prospect of using hydrogen as fuel, since it has higher stoichiometric combustion temperature, and the combustion products include water vapor, which increases the load on parts exposed to the hot flow. For future turbines, therefore, the thermal management is of the utmost importance; this includes both the cooling system itself – internal cooling and film cooling – as well as protective coatings on the exposed surface of the parts. Additive manufacturing of metallic parts is already a reality for production of static turbine parts, and in the future rotating blades could also be produced by this method. This paradigm shift opens the design space of turbine cooling systems by reducing the manufacturing constraints of the parts, so that radically new cooling concepts can be implemented. For internal cooling, jet impingement achieves the highest local heat transfer and is therefore used in the most highly stressed regions of the turbine parts. The crossflow caused by the spent air of the jets, however, limits the number of jets that can be used in a channel while maintaining high cooling performances, especially in narrow channels with maximum crossflow configuration. The main objective of this work is the experimental investigation of a new impingement channel design that reduces the crossflow by stacking two consecutive shorter channels connected via a plenum. In total, 34 large scale models have been investigated at engine-relevant Reynolds numbers using a new transient liquid crystal technique. Experimental data include high resolution heat transfer coefficients on the target plates as well as pressure data at several locations, which allows to determine the pressure drop of each part of the channel. In a first, exploratory phase, the effect of the variation of the number of jets and of the length of the transition zone has been studied. Moreover, bypass holes that connect directly the two channels and allow for an initial crossflow in the second channel have been investigated. A low heat transfer region has been identified in the transition zone; therefore, several heat transfer enhancement devices have been installed in this zone. Ribs, pins, and cross-section reductions allow to increase the heat transfer coefficient levels. Combinations of these devices provide

higher heat transfer enhancement with a marginal increase of the pressure drop. An analytical approach has been used to estimate the metal temperatures of a part cooled by the sequential channels in comparison to a conventional narrow impingement channel at the same massflow, with the new concept achieving lower temperature when using high performance heat transfer enhancement designs. With the coolant mass flow reduction allowed by the new design, an improvement of the thermal efficiency of 0.7% has been estimated when considering the thermodynamic cycle of a modern gas turbine.

Zusammenfassung

Im Zuge der künftigen Dekarbonisierung der Erzeugung von elektrischer Energie werden Gasturbinen ein wichtiges Instrument zur Stabilisierung des Stromnetzes sein, indem sie die Spitzen des Energiebedarfs mit kohlenstofffreien Brennstoffen wie synthetischem Gas und Wasserstoff decken. Die Verbrennungstemperatur in Gasturbinen ist im Laufe der Jahre in dem Bestreben, den thermischen Wirkungsgrad der Maschine zu erhöhen, stetig gestiegen, so dass in modernen Gasturbinen eine aktive Kühlung der Turbinenschaufeln eingesetzt wird, um einen sicheren Betrieb zu gewährleisten. Die Notwendigkeit der Kühlung wird durch die Aussicht auf die Verwendung von Wasserstoff als Brennstoff noch verstärkt, da dieser eine hohe stöchiometrische Verbrennungstemperatur hat und die Verbrennungsprodukte Wasserdampf enthalten, was die thermische Belastung der der Hitze ausgesetzten Teile erhöht. Für künftige Turbinen ist daher das Wärmemanagement von größter Bedeutung; dies umfasst sowohl das Kühlsystem selbst – Innenkühlung und Filmkühlung – als auch Schutzbeschichtungen auf den freiliegenden Oberflächen der Teile. Die additive Fertigung von Metallteilen ist für die Produktion von statischen Turbinenteilen bereits Realität, und in Zukunft könnten auch rotierende Schaufeln mit dieser Methode hergestellt werden. Dieser Paradigmenwechsel erweitert den Gestaltungsspielraum für Turbinenkühlsysteme, indem er die Herstellungsbeschränkungen für die Teile verringert, so dass völlig neue Kühlkonzepte entwickelt und eingesetzt werden können. Bei der Innenkühlung wird mit der Prallkühlung der höchste lokale Wärmeübergang erzielt und daher in den am stärksten belasteten Bereichen der Turbinenteile eingesetzt. Die Querströmung, die durch die verbrauchte Luft entsteht, begrenzt jedoch die Anzahl der Düsen, die in einem Kanal unter Beibehaltung hoher Kühlleistungen eingesetzt werden können, insbesondere in engen Kanälen mit maximaler Querströmungskonfiguration. Das Hauptziel dieser Arbeit ist die experimentelle Untersuchung eines neuartigen Prallkühlungs-Kanal-Konzept, das die Querströmung reduziert, indem zwei aufeinanderfolgende kürzere Kanäle über ein Plenum verbunden werden. Insgesamt wurden 34 maßstäblich vergrößerte Modelle bei machinenrelevanten Reynoldszahlen unter Verwendung einer Variation der transienten Flüssigkristalltechnik untersucht. Zu den experimentellen Daten gehören hochauflösende Wärmeübergangskoeffizienten an den Zielplatten der Kanäle, sowie Druckmessungen an mehreren Stellen, die es ermöglichen, den Druckabfall in jedem Teil des Kanals zu bestimmen. In einer ersten, explorativen Phase wurden die Auswirkungen der Variation der Anzahl der Düsen und der Länge der Übergangszone

untersucht. Außerdem wurde der Einfluß von Bypass-Löchern untersucht, die die beiden Kanäle direkt miteinander verbinden und eine anfängliche Querströmung im zweiten Kanal ermöglichen. In der Übergangszone wurde ein Bereich mit geringem Wärmeübergang festgestellt; daher wurden hier mehrere Vorrichtungen zur Verbesserung des Wärmeübergangs installiert. Rippen, Stifte und Querschnittsverringerungen ermöglichen eine Erhöhung der Wärmeübergangskoeffizienten in diesem Bereich. Kombinationen dieser Verbesserungsvorrichtungen wurden untersucht und bieten im Allgemeinen eine höhere Wärmeübertragungsleistung bei einem nur geringfügig ansteigenden Druckabfall. Anhand eines analytischen Ansatzes wurden die Metalltemperaturen eines durch die sequenziellen Kanäle gekühlten Bauteils im Vergleich zu einem herkömmlichen engen Prallkanal bei gleichem Massenstrom abgeschätzt, wobei das neue Konzept bei Verwendung von Hochleistungs-Wärmeübertragungsverbesserungsvorrichtungen niedrigere Materialtemperaturen erzielt. Mit der durch das neue Design ermöglichten Reduzierung des Kühlmittelmassenstroms wurde eine Verbesserung des thermischen Wirkungsgrads von 0.7% unter Verwendung des thermodynamischen Zyklus einer modernen Turbine geschätzt.

Résumé

Les turbines à gaz vont être un outil important pour la stabilisation du réseau électrique lors de la future décarbonisation de la production d'énergie électrique, pouvant répondre aux pics de demande avec des combustibles durables comme le gaz synthétique et l'hydrogène. Pour augmenter le rendement thermique, la température de combustion dans les turbines à gaz n'a cessé d'augmenter au fil des ans, de sorte que dans les turbines à gaz modernes un refroidissement actif des aubes est nécessaire pour garantir un fonctionnement sûr. La perspective d'utiliser l'hydrogène comme combustible augmente l'importance d'un système de refroidissement performant, car il a une température de combustion stœchiométrique plus élevée, et son principal produit de combustion est la vapeur d'eau, ce qui augmente la charge thermique sur les parties soumises à l'écoulement chaud. Pour les futures turbines, la gestion thermique est donc de la plus haute importance ; elle comprend à la fois le système de refroidissement lui-même – refroidissement interne et refroidissement par film – et les revêtements de protection sur la surface exposée des pièces. La fabrication additive de pièces métalliques est déjà une réalité pour la production de certaines parties de la turbine et, à l'avenir, les pales rotatives pourraient également être produites par cette méthode. Ce changement de paradigme ouvre l'espace de conception des systèmes de refroidissement des turbines en réduisant les contraintes de fabrication des pièces, de sorte que des concepts de refroidissement radicalement nouveaux peuvent être conçus. Concernant le refroidissement interne, le refroidissement par impact de jets permet d'obtenir le transfert de chaleur local le plus élevé et est donc utilisé dans les zones les plus sollicitées des pièces à refroidir. L'écoulement transversal (crossflow) dû à l'air s'écoulant vers la sortie du canal limite cependant le nombre de jets pouvant être utilisés tout en maintenant des performances de refroidissement élevées, en particulier dans les canaux étroits avec une configuration de crossflow maximale. L'objectif principal de ce travail est l'étude expérimentale d'une nouvelle conception de canaux refroidis par impact de jets qui permet de réduire le crossflow en combinant deux canaux plus courts connectés en série via un plenum. Au total, 34 modèles à grande échelle ont été étudiés à des nombres de Reynolds équivalant à ceux d'un système réel, en utilisant une variation de la technique transitoire des cristaux liquides. Les données expérimentales comprennent des coefficients de transfert de chaleur à haute résolution sur les surfaces impactés par les jets, ainsi que des données de pression à plusieurs endroits qui permettent de déterminer les pertes de charge de chaque segment du canal. Dans une première phase exploratoire, les

effets du changement du nombre de jets et de la longueur de la zone de transition ont été évalués. En outre, des trous de bypass reliant directement les deux canaux et permettant un crossflow initial dans le second canal ont été étudiés. Une région à faible transfert de chaleur a été identifiée dans la zone de transition ; par conséquent, plusieurs dispositifs d'amélioration du transfert de chaleur ont été installés dans cette zone. Des pontets, des ailettes à picots et des réductions de section permettent d'augmenter les niveaux du coefficient de transfert de chaleur dans la zone de transition. La combinaison de ces dispositifs fournit généralement un transfert de chaleur plus élevé avec une augmentation marginale des pertes de charge. Une approche analytique a été utilisée pour estimer les températures d'une pièce refroidie par canaux séquentiels en comparaison avec un canal conventionnel à débit massique égal ; le nouveau concept permet d'obtenir des températures plus basses en utilisant des dispositifs d'amélioration du transfert de chaleur à haute performance. En considérant la réduction du débit massique du gaz de refroidissement réalisable avec la nouvelle conception, et en prenant en compte le cycle thermodynamique d'une turbine à gaz moderne, un gain d'efficacité thermique de 0.7% a été estimé.

Sommario

In futuro, le turbine a gas saranno uno strumento importante per stabilizzare la rete elettrica a basse emissioni di ossidi di carbonio, essendo in grado di soddisfare la domanda di picco con combustibili sostenibili come il gas sintetico e l'idrogeno. Per aumentare l'efficienza termica, la temperatura di combustione nelle turbine a gas è aumentata costantemente nel corso degli anni, così che nelle moderne turbine è necessario un raffreddamento attivo delle pale per garantire un funzionamento sicuro. La prospettiva di usare l'idrogeno come combustibile aumenta l'importanza di un sistema di raffreddamento efficiente, poiché ha una temperatura di combustione stechiometrica più alta, e il suo principale prodotto di combustione è il vapore acqueo, che aumenta il carico termico sulle parti soggette al flusso caldo. Per le turbine del futuro, la gestione termica è quindi della massima importanza; comprende sia il sistema di raffreddamento stesso – raffreddamento interno e raffreddamento a film – sia i rivestimenti protettivi sulla superficie esposta delle parti. La fabbricazione additiva di parti metalliche è già una realtà per la produzione di alcune parti di turbine, e in futuro anche le pale rotanti potrebbero essere prodotte con questo metodo. Questo cambio di paradigma apre lo spazio di progettazione per i sistemi di raffreddamento delle turbine, riducendo i vincoli di fabbricazione delle parti, in modo che possano essere realizzati concetti di raffreddamento radicalmente nuovi. Per quanto concerne il raffreddamento interno, il raffreddamento a getti fornisce il più alto trasferimento di calore locale e viene quindi utilizzato nelle aree più sollecitate delle parti da raffreddare. Tuttavia, il flusso trasversale (crossflow) dovuto all'aria in uscita dal canale limita il numero di getti che possono essere usati mantenendo alte prestazioni di raffreddamento, specialmente in canali stretti con un crossflow massimo. L'obiettivo principale di questo lavoro è l'indagine sperimentale di un nuovo systema di raffreddamento a impatto di getti che riduce il crossflow grazie all combinazione di due canali più corti collegati in serie tramite un plenum. Un totale di 34 modelli su larga scala sono stati studiati a numeri di Reynolds equivalenti a quelli di un sistema reale, utilizzando una variazione della tecnica della termografia a cristalli liquidi. I dati sperimentali includono coefficienti di trasferimento di calore ad alta risoluzione sulle superfici colpite dai getti, così come dati di pressione in diversi punti che permettono di determinare la perdite di carico di ogni segmento del canale. In una prima fase esplorativa sono stati valutati gli effetti del cambiamento del numero di getti e della lunghezza della zona di transizione. Inoltre, sono stati studiati dei fori di bypass che collegano direttamente i due canali e permettono un

crossflow iniziale nel secondo canale. Una regione con basso trasferimento di calore è stata identificata nella zona di transizione; di conseguenza, diversi dispositivi di miglioramento del trasferimento di calore sono stati installati in quest'area. Alette e chiodi di raffreddamento, così come riduzioni della sezione trasversale, sono utilizzati per aumentare il coefficiente di trasferimento del calore nella zona di transizione. La combinazione di questi dispositivi fornisce generalmente un maggiore trasferimento di calore con un aumento marginale della perdite di carico. Un approccio analitico è stato utilizzato per stimare le temperature di una parte raffreddata da canali sequenziali rispetto a un canale convenzionale a pari flusso di massa; il nuovo concetto permette di ottenere temperature più basse utilizzando aumentatori di trasferimento di calore ad alte prestazioni. Considerando la riduzione del flusso di massa del gas di raffreddamento ottenibile con il nuovo design, e prendendo in conto il ciclo termodinamico di una moderna turbina a gas, è stato stimato un guadagno di efficienza termica dello 0,7%.

Contents

List of Figures

List of Tables

Nomenclature

Roman symbols

A	Area	m^2
AR	Aspect ratio	–
C_D	Discharge coefficient	–
c	Specific heat capacity	$J/(kgK)$
c_p	Specific heat capacity at constant pressure	$J/(kgK)$
D	Jet diameter	m
D_H	Hydraulic diameter	m
e	Rib height	m
$\dot{E}_u$	Useful power	W
f	friction factor	–
h	Heat transfer coefficient	$W/(m^2K)$
H	Ramp height	m
k	Thermal conductivity	$W/(mK)$
L	Length	m
$\dot{m}$	Massflow	kg/s
n	Number of jets	–
Nu	Nusselt number	–
P	Pitch	m
p	Pressure	Pa
Pr	Prandtl number	–
$\dot{Q}$	Heat input rate	W
q	Heat flux	W/m^2
q_0	Heat flux rate of change	$W/(m^2s)$
q_{in}	Specific heat input	J/kg
Re	Reynolds number	–
T	Temperature	K
$\hat{T}$	Measured temperature	K
$T^\star$	Non-dimensional temperature	–
T_{C_i}	Coolant inlet temperature	K
T_{C_o}	Coolant outlet temperature	K

T_M	Metal temperature	K
t	Time	s
u	flow velocity	m/s
X	Jet-to-jet spacing	m
Y	Width of the channel	m
Z	Height of the channel	m

Greek symbols

α	thermal diffusivity	m^2/s
δ	thickness	m
ϵ	cooling effectivenes	–
η	cooling efficiency	–
η_{tp}	thermal performance	–
η_e	entrainment effect	–
η_{th}	thernal efficiency	–
η_{sk}	isentropic efficiency of the compressor	–
η_{st}	isentropic efficiency of the turbine	–
κ	heat capacity ratio	–
μ	dynamic viscosity	$Pa.s$
ν	kinematic viscosity	m^2/s
Π	pressure ratio	–
ρ	density	kg/m^3
τ	time constant	s

Subscripts

0	baseline
$1, 2, 3, 4$	entry/exit of the turbine/compressor
aw	adiabatic wall
C	coolant
c	total value
cf	crossflow
ext	external
i	initial
j	jet
g	gas
l	lateral conduction
k	compressor
r	recovery
t	turbine
ti	thermal inertia
$trans$	transition

Acronyms

BFM	Backflow margin
CFD	Computational Fluid Dynamics
CMOS	Complementary Metal-Oxide-Semiconductor
DAQ	Data Acquisition
DC	Direct Current
DNS	Direct Numerical Simulation
DSM	Demand Side Management
EBM	Electron-Beam Melting
HPT	High Pressure Turbine
HSL	Hue-Saturation-Lightness
LED	Light Emitting Diode
LES	Large Eddy Simulation
LFE	Laminar Flow Element
LPT	Low Pressure Turbine
NGF	Next Generation Fighter
P2G	Power-to-Gas
PMMA	Poly(methyl methacrylate)
PWM	Pulse Width Modulation
RANS	Reynolds-Averaged Navier-Stokes
RGB	Red-Green-Blue
SLM	Selective Laser Melting
SST	Shear Stress Transport
TBC	Thermal Barrier Coating
TBO	Time Between Overhaul
TET	Turbine Entry Temperature
TLC	Thermochromic Liquid Crystals
TSP	Temperature Sensitive Paint
UV	Ultra-Violet

Chapter 1

Introduction

In this chapter, the relevance of gas turbines in the current and future energy landscape is introduced. The importance of active cooling of the hot components is discussed, as well as the future trends in turbine cooling, with an emphasis on impingement cooling. Finally, the scope of the Thesis is outlined.

1.1 The gas turbine for carbon-free electricity production

The global warming resulting from anthropogenic emissions of greenhouse gases is one of the biggest challenges currently facing the scientific community. The solutions to limit the average temperature increase need to be found not only at a scientific level, but also at a political level through policy changes. In this respect, the European Union (EU) and 190 states signed the Paris Agreement in 2015 with the aim of limiting the temperature increase to 1.5°C compared to pre-industrial levels. To achieve this goal, each country sets its own roadmap, with the common goal of achieving net-zero carbon emissions for 2050. In the following the focus is on the Swiss policy, but very similar objectives have been set by other states, e.g. the EU.

The "Energy Strategy 2050" of the Swiss Confederation calls for the carbon neutrality of Switzerland for 2050, and for the shutdown of nuclear power plants that currently meet the base load on the electrical grid. The electricity need will be provided mainly by renewable energies. Hydroelectric plants are already the backbone of the Swiss electric grid and their expansion is limited. The generation capacity of wind and solar will need to be expanded considerably in order to meet the electricity demand, which is going to increase due to the ongoing electrification of the transport system and to the replacement of oil powered domestic heating systems with heat pumps. Solar panel installations in Switzerland are increasing exponentially, thanks to the steady reduction of panel costs. However, solar is an intermittent energy source, which provides excess generation during

the daytime, but is not available during the evening peak of consumption, leading to the characteristic "duck shape" of the energy demand curve (Denholm et al., 2015).

Although demand side management (DSM) systems – which control household loads and, if present, a battery for power storage – could reduce the problem (Medici et al., 2017), this peak needs to be met either by energy that has been stored during times of excess production (when supply exceeds demand), or by energy sources that can come online fast. Additionally, seasonal imbalance in electricity production must also be considered: solar energy is more plentiful during the summer, hydroelectric power has maximum generation after snow melt in late spring, etc.

While for short term storage (several hours) batteries are the most convenient solution and are gaining market share thanks to the steady price reduction, storage in chemical form (hydrogen, or synthetic gas) seems to be more appropriate for long term storage. To recover the energy stored in chemical form via a power-to-gas (P2G) approach (Gallandat et al., 2018; Wulf et al., 2018; Thema et al., 2019) or directly from solar to hydrogen (Hisatomi and Domen, 2019; Tembhurne et al., 2019), the usage of gas turbines is a good option since it is a well established solution, has a quick startup time (in the order of minutes), achieves high thermal efficiencies (more than 60% when deployed in a combined cycle power plant), is capable to produce high power in a very compact format, and can also work efficiently at partial load, thus can adapt rapidly to changes in the electricity demand.

Recently, the possibility of using hydrogen (H_2) as fuel in state-of-the-art gas turbines has been evaluated (Bothien et al., 2019), and this showed that it is possible to use a mixture of H_2 and natural gas as fuel while complying with the emission requirements in terms of NO_x. Moreover, the tests showed that also pure H_2 can be used, with only a small de-rating to comply with NO_x emissions. This opens the possibility of using P2G as a flexible and efficient method of energy storage for long term load balancing.

Gas turbines are internal combustion engines used for electricity generation, air and naval transportation, as well as for driving compressors in the gas and oil industry. The first commercial power generating machine based on the Brayton cycle, installed in 1939 in Neuchâtel, Switzerland, had an efficiency of 17.4%. In the last 80 years, gas turbines have steadily improved their efficiency. This has been accomplished by improving the aerodynamic flow using better design tools, reducing tip clearances and leakage flows, and increasing the overall pressure ratio and turbine entry temperature (TET). TET is especially important, since efficiency theoretically increases up to stoichiometric temperatures. In the Neuchâtel machine, TET was in the order of 540°C; on state-of-the-art gas turbines for electricity generation, like for example the GT36 machine in Figure 1.1, TET can reach approximately 1600°C, and this, in addition to other improvements, allows for a thermal efficiency of approximately 43%. In a combined cycle, where the residual heat at the exit of the gas turbine cycle is used to generate steam to drive a steam turbine, the efficiency can reach 64% (Vandervort et al., 2019), and even higher if the residual heat is used for e.g. district heating.

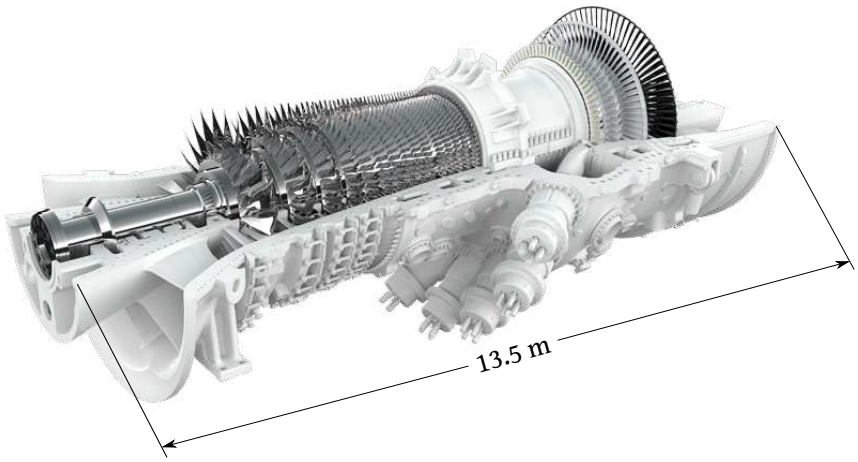

Figure 1.1 – Ansaldo GT36: a state of the art gas turbine in the 500 MW class, with a combined cycle efficiency of 62.6%. Courtesy of Ansaldo Energia Switzerland.

1.2 Turbine cooling problem

The increase of TET has been primarily driven by material improvements, both in terms of alloy composition – Nickel-based superalloys being the most common today – and manufacturing techniques (directional-solidification, single crystal casting). Additionally, thermal barrier coatings (TBC), generally ceramic based, improve the oxidation and corrosion resistance of the material and thermally insulate the part, with a reduction of the effective heat transfer coefficient of up to 50% (Downs and Landis, 2009). Using these techniques, turbine parts in contact with the hot gas flow can withstand temperatures in the order of 1150°C. To further increase the flow temperature, these parts – stator heat shield, guiding vanes, turbine blades – need to be actively cooled to avoid excessive thermal stresses that can result in catastrophic failure due to creep and thermal fatigue. Figure 1.2 shows the temporal evolution of the maximum allowable metal temperature of various alloys, as well as the evolution of the TET. Since the advent of cooled turbines in the '60s, TET has exceeded the metal temperature, with major improvements since the mid '70s. In recent times, the trend is an increase of TET of about 10 K/yr, and of the maximum metal temperature of about 3 K/yr (Kyprianidis, 2011), and consequently the gap between these 2 temperatures keeps widening and must be bridged with more effective cooling technologies.

Some of the compressed air is bypassed from the compressor exit and used to convectively cool the material by flowing in small passages inside the thermally loaded parts. Often, the coolant is then ejected in the hot gas path, in order to envelop the external surface with a film of cooling fluid that separates the surface from the hot flow. The use of bypass air from the compressor, which is driven by the turbine, has the direct effect of decreasing the overall efficiency: at some point, the performance gains of the temperature increase are counterbalanced by the performance reduction due to the increased coolant flow, and

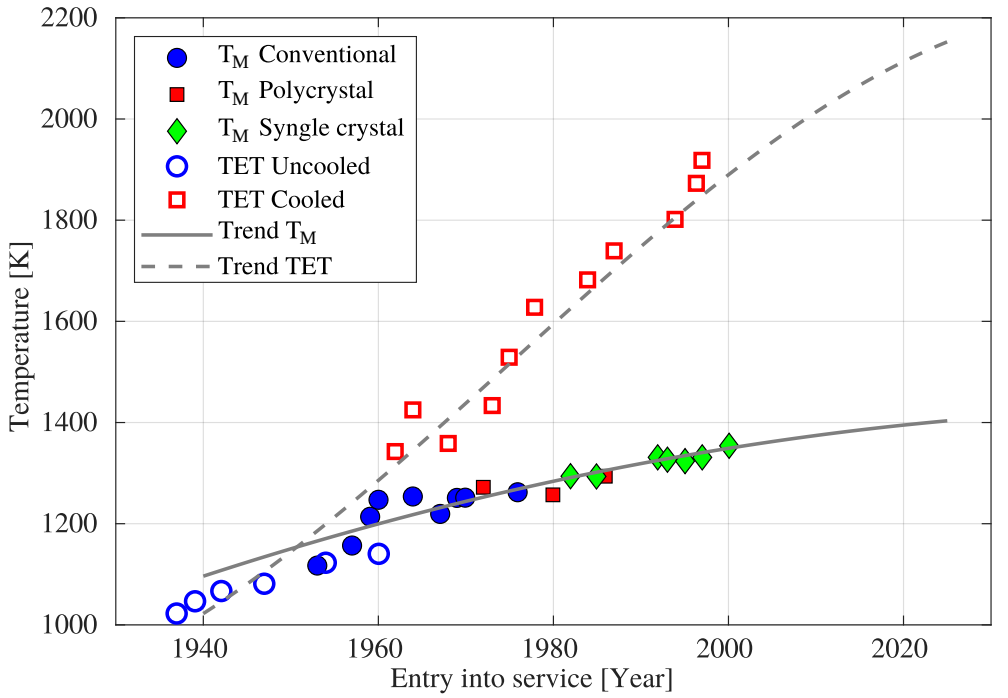

Figure 1.2 – Historical evolution of the maximum allowable metal temperature (T_M) and of the turbine entry temperature (TET) for aeroengines. TET of gas turbines for electricity production follow a similar trend. Data extracted from Kyprianidis (2011) and Terzis (2014).

this at TET below the temperature resulting by stoichiometric combustion (Horlock et al., 2001). For modern machines, the amount of air used for cooling can be as high as 30% of the total air flowing through the compressor. Therefore, there is a need to reduce the amount of cooling air as much as possible, and this can be accomplished by increasing the efficiency of the cooling system.

The move to hydrogen fuel brings with it several problems due to the different combustion characteristics, like autoignition and flashback due to the higher flame speed and lower ignition delay time, and possible thermoacoustic instabilities in the combustion chamber. Additionally, the higher adiabatic flame temperature in comparison to natural gas, and the increased heat transfer coefficient of the hot flow due to the added moisture content of the exhaust gas (the product of hydrogen combustion being water vapor), call for the development of more effective cooling solutions.

Convective cooling schemes range from simple, smooth channels inside a solid part, to more complex systems in which heat transfer augmentation devices (turbulence generators, ribs, pins) are added in the channels to increase the turbulence levels and promote flow mixing. Multi-pass channels can also be used to increase the cooling efficiency. Jet impingement cooling allows for high local heat transfer at the impingement location and is widely used on highly thermally loaded parts. Using state-of-the-art investment casting techniques, impingement cooling can be integrated into the wall of the blade allowing for

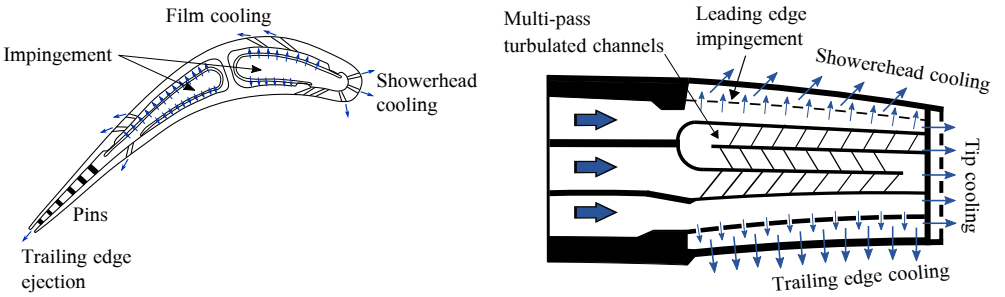

Figure 1.3 – Schematics of typical turbine cooling solutions for the stator vanes (left) and the rotor blades (right). Images drawn according to Han (2018).

a thickness reduction of the external wall, which increases the heat transfer considerably.

Generally speaking, the stator vanes are mostly cooled using impingement, with the exception of the trailing edge, which is too thin to integrate an impingement scheme and is therefore cooled using pin-fins (see Fig. 1.3). Similarly, the casing and heat shield are mostly cooled by jet impingement, which can achieve high local heat transfer coefficients with low pressure losses. Additionally, in both the stator vanes and rotor blades, the spent air is used for film cooling, by ejecting the coolant to form a protective layer of (relatively) cold air on top of the blade surface.

Using state-of-the-art cooling concepts, which combine several cooling strategies in a single blade, TET as high as 1600°C can be achieved (Hada et al., 2015). The problem of active component cooling is also a central point in turbomachinery for aerospace applications, for which power-to-weight ratio is favored over time between overhauls (TBO). In such applications, TET can reach 1750°C (Ballal and Zelina, 2004), and possibly more for military aircraft, although reliable data for fighter jets are difficult to obtain for obvious reasons. According to aircraft engine manufacturer MTU, the engine under development for the Next Generation Fighter (NGF) will target a TET of 2100°C for 2035-2040 (Kuzia, 2019). To achieve this ambitious goal, more effective cooling systems need to be developed. Moreover, the optimal (i.e. most efficient) overall pressure ratio increases with increasing TET, but increasing the pressure leads directly to an increase of the compressor exit temperature. This means that the coolant temperature tends to be higher in modern machines, which is an additional reason for the requirement of more effective cooling.

1.3 Future trends in turbine cooling

In recent years, novel additive manufacturing techniques like selective laser melting (SLM) and electron-beam melting (EBM) have been used to manufacture gas turbine components, most recently also on thermally loaded parts like fuel nozzles (Orcutt, 2016), which are already in commercial use, and even turbine blades: in 2019 Siemens successfully tested

3D-printed turbine blades at operating conditions with accelerations of $10^4 g$ at a temperature of 1250°C (Siebold, 2019). Additively manufactured stator vanes and heat shields have also been validated (Torkaman et al., 2021; Naik et al., 2021), although quality control and volume manufacturing are still open issues. Nevertheless, this constitutes a paradigm shift for the cooling design of turbine blades: while in the past manufacturing possibilities have put hard constraints and dictated the design of the cooling system, with additive manufacturing – and to a lesser extent advanced investment casting – the thermal engineer is given almost complete freedom in the design of the layout of the internal cooling passages. This allows for radically new concepts of blade cooling.

Additive manufacturing techniques can also advance the state of the art of film cooling: with more freedom in the integration of film holes, a more uniform film of the cooling air can be achieved on the blade surface. Beyond this, effusion cooling, which is essentially analogous to film cooling using a porous skin, has been under study for decades (the first patent is from Meginnis, 1972), but has not been implemented in industrial turbines yet. Here, additive manufacturing could play a role by better controlling the porous structure of the material. The size of the pores can be controlled by varying the diameter of the laser beam used in SLM; this has been demonstrated for burner tips (Kiener et al., 2019) and the same approach could be used for the stator vanes. Rotor blades are more challenging since the material has to withstand strong centrifugal forces. However, mixing losses due to the coolant flow entering the mainstream flow put a limit on the amount of air that can be used for film cooling without affecting the cycle efficiency (the so called Hartsel losses, see Hartsel, 1972). There is thus a need for better performing convective cooling solutions.

For impingement cooling, the focus in recent years has been on narrow channels; in contrast to a classical (rectangular) array of impinging jets, a narrow channel only has one or two rows of jets, bounded by sidewalls. The thermal performance of such a channel is better than an array, since the sidewalls – and to some extent the jet plate – contribute significantly to the heat transfer (Ricklick et al., 2010). However, for channels with a high number of jets, the crossflow of the spent air of the upstream jets interacts with the downstream jets thereby reducing their cooling capabilities (Chambers et al., 2005; Fechter et al., 2013; Llucià et al., 2015). Cooling air extraction for film cooling through holes in the external wall can reduce the crossflow velocity (Rao et al., 2018). As noted above, however, Hartsel aerodynamic losses limit the usage of external cooling in future turbine systems.

Recent work focused on the evaluations of ways to limit the crossflow, for example by using ribs on the target plate to divert the crossflow away from the jet (Chen et al., 2017), elongated-elliptical jet holes (Chambers et al., 2010), castellated channels to reduce the crossflow velocity (Kim et al., 2021), or divergent channel geometries (Terzis et al., 2016b), by varying the jet diameter (Uysal et al., 2006; Miller et al., 2013; Terzis et al., 2015), or by staggering the jet holes (Terzis et al., 2014b). These modifications, however, can only marginally improve the mean heat transfer levels of the cooling channel,

even with rib/pin roughened target plates (Miller et al., 2013; Rao, 2018), and therefore alternatives have to be considered.

1.4 The present study

To reduce the crossflow effect in a long narrow impingement channel, another possibility is to connect two (or more) shorter channels in series via a plenum, so that in the second channel the crossflow is reset (see Fig. 1.4). An additional advantage of this sequential arrangement is that the coolant is used two times for impingement, which has some beneficial repercussions:

- For a given coolant massflow the jet velocity is increased, since the number of jets is reduced.
- Conversely, for a given jet velocity, the total coolant massflow is strongly reduced.
- By using the coolant two times for impingement, the cooling efficiency η is increased.

The cooling efficiency is defined as follows:

$$\eta = \frac{T_{C_o} - T_{C_i}}{T_M - T_{C_i}} \tag{1.1}$$

in which T_{C_i} and T_{C_o} are the inlet and outlet temperature of the coolant, respectively, and T_M the temperature of the metal blade. In practice, higher efficiencies correspond to a better use of the coolant fluid, with a value that approaches $\eta = 1$ when the coolant outlet temperature approaches the metal temperature. By using the coolant multiple times, the heat pickup, and hence T_{C_o} increases.

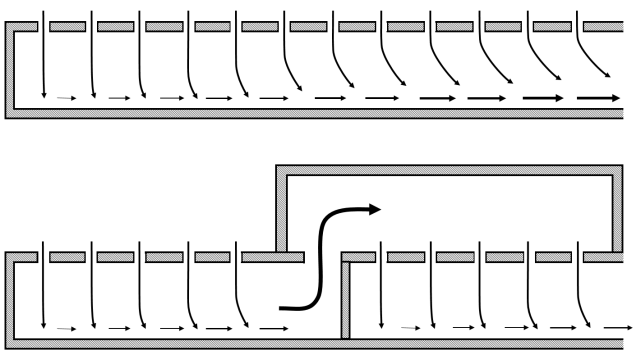

Figure 1.4 – Sketch of a classical impingement channel (top) and a sequential impingement channel (bottom). By connecting two shorter channels in series, the impact of the crossflow can be reduced.

The end goal is to increase the cooling effectiveness ϵ, defined as:

$$\epsilon = \frac{T_{ext} - T_M}{T_{ext} - T_{C_i}} \tag{1.2}$$

where T_{ext} is the hot path gas temperature. In practice, the objective is to achieve lower T_M, or conversely to increase T_{ext} (and hence TET) for a given T_M.

The proposed arrangement is expected to have two critical points. First, the more intricate passage results in higher pressure losses, or a lower jet velocity for the same pressure difference. As a first approximation, and neglecting the discharge into the second plenum, with two equal flow resistances in series the massflow is reduced by $\sqrt{2}$, for the same pressure difference, compared to a single resistance (Livesey, 1998). This is partially offset by the fact that a smaller massflow is needed to achieve the same jet velocity. In any case, care should be taken to ensure that sufficient backflow margin (BFM), defined as the difference between the pressure of the cooling flow in the channel and the pressure at the channel exit into the external flow (e.g. the film cooling hole), exists in all operating conditions. Second, the need to discharge the flow opposite the target plate implies that the most downstream part of the 1st channel – the so called transition zone – cannot be cooled with impingement jets. This is an area where the heat transfer coefficient is expected to be lower, resulting in higher temperatures and, more importantly, high temperature gradients that could cause thermal stresses in the material, possibly causing premature component failure in operation. For this reason heat transfer augmentation devices may be needed in this area.

Although some patents describing a similar sequential arrangement of impingement channels have been filed (Downs and Fedock, 2012; Plank et al., 2012; Jones et al., 2013), no studies have been published in the open literature about the performances of such an arrangement. Therefore, the objective of the present thesis is:

> *The experimental analysis of sequential impingement channels to assess the performances in term of heat transfer and pressure drop at engine representative Reynolds numbers, and the evaluation of various heat transfer enhancing features in the transition zone.*

The experiments have been performed on a scaled up geometry at EPFL's jet impingement test facility, which was developed for a previous project (Terzis, 2014), using a novel transient technique based on thermochromic liquid crystals (TLC). The development and validation of a new experimental technique was necessary to be able to reliably investigate the sequential channels.

Many studies in the literature deal with numerical simulations of impinging jets. RANS modeling still lacks the required accuracy, and depends heavily on the turbulence modeling used. Best results are currently obtained using Menter's SST k-ω model, but results can

be off by as much as 20% in terms of heat transfer coefficient (Zuckerman and Lior, 2006). Second order closures like RSM (Reynolds stress model) require very fine grids to obtain adequate results. Large eddy simulations (LES) are too costly to implement for many configurations, and direct numerical simulations (DNS) of impinging jets at high Reynolds numbers are out of reach of today's computational resources. This is the reason why the present study investigates the performances of impingement channels experimentally, with supporting CFD simulations to assess the flow characteristics.

1.5 Structure of the Thesis

In the next chapter, the most relevant bibliographic resources consulted during the study are presented. In Chapter 3, the experimental setups used for the validation of the experimental technique and for the heat transfer tests are presented, as well as the configurations that are investigated. Chapter 4 presents the experimental technique used and its validation, along with an estimation of the experimental uncertainties. Chapter 5 reports the experimental results obtained during the project. The results are then analyzed in Chapter 6 to assess the performance of the sequential impingement channel and the achievable improvement compared to traditional narrow impingement channels. Finally, Chapter 7 concludes with a summary of the main findings and suggestions for future investigations concerning these configurations.

Chapter 2

Literature review

This chapter gives an overview of the literature on impingement heat transfer starting from the fluid mechanics of free jets to the heat transfer of jet impingement arrays, and then highlights recent work in sequential impingement. Section 2.4 is devoted to the review of experimental techniques used for the determination of the heat transfer and a rationale for the devolpement of a new technique for the study presented here; parts of this Section have been published in Schmid et al. (2021). The chapter concludes with the contributions of the present work to the state of the art.

2.1 Introduction

Jet impingement is widely used in many industries, from the cooling of electronic devices or solar panels (Torbatinezhad et al., 2021) to the heat treatment of metallic pieces (e.g. quenching, Zuckerman and Lior, 2006), and most notably in the cooling of hot parts of gas turbines, which is the main driver for the high number of studies devoted to the fluid dynamics and thermal aspects of impinging jets. In turbomachinery applications, jet impingement is attractive because of the very high heat transfer achieved locally in the stagnation region of the jet, and is therefore used in the most thermally loaded parts, like inlet guide vanes, combustor liners, or the stator heat shield. The use on rotating blades has been limited for two reasons. First, the double-walled construction needed to integrate the impingement plate in the blade reduces the mechanical strength of the blade, which is subject to high mechanical stresses due to the centrifugal forces, although with advanced casting techniques this problem has been partially solved. Secondly, the centrifugal forces affect the flow characteristics of the jets; for this reason impingement cooling is only considered for the leading edge of the blade, which is the most thermally stressed part.

2.2 Impinging jets

2.2.1 Free jets

The fluid mechanics of a free jet has been studied extensively, starting in the 1930's with Ruden (1933), Forthmann (1934) and Kuethe (1933), motivated by the research on the jet engine, and later by Squire and Trouncer (1944), Heskestad (1965), Gutmark and Wygnanski (1976), and Kotsovinos (1978), among others.

A circular jet can be divided in three regions along the flow direction (Figure 2.1). First, the potential core region, in which the velocity at the center line is constant; an annular shear layer mixes the jet flow with the surrounding air at rest. This shear layer has the effect of increasing the jet diameter. In the second region (transition region), the shear layer reaches the center line, and the velocity at the center line starts to decrease. In the third region, the fully developed region, the center line velocity is inversely proportional to the distance from the nozzle, and the jet behavior is self-similar, i.e.the velocity profile at each axial location, scaled with the centerline velocity, has the same Gaussian distribution.

2.2.2 Impinging jets

In the case of a jet impinging on a flat surface, the flow can be subdivided in 3 zones: a free jet region, a stagnation zone, where the jet impinges on the surface and its vertical momentum is converted to horizontal momentum, and a wall jet region (Figure 2.2).

At first, the heat transfer characteristics of impinging jets have been studied for single jets configurations on a flat plate normal to the jet (Martin, 1977; Beltaos and Rajaratnam, 1973; Gutmark et al., 1978). Hoogendoorn (1977), as well as Lytle and Webb (1994),

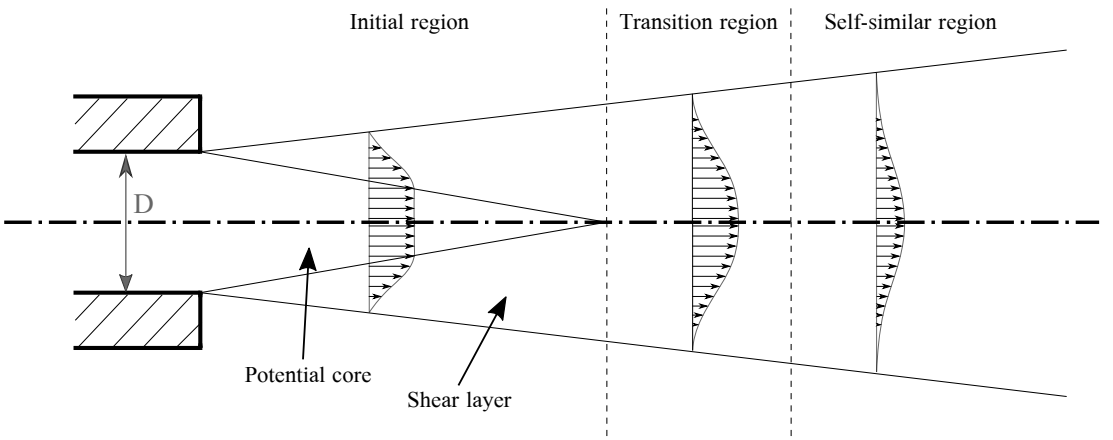

Figure 2.1 – Schematics of the evolution of a free jet.

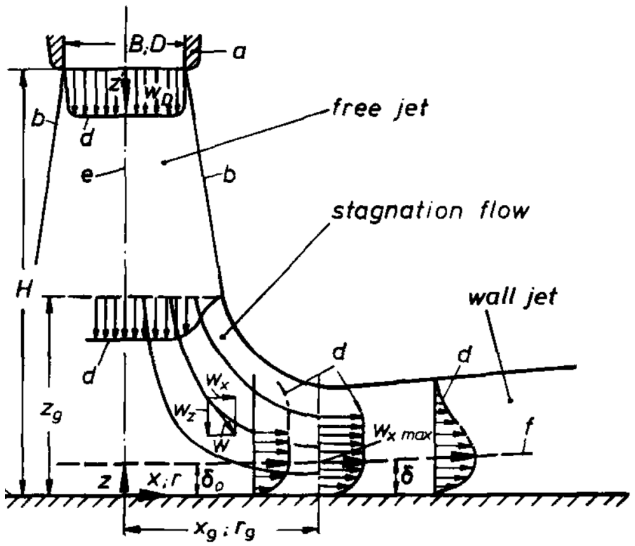

Figure 2.2 – Schematics of a jet impinging on a flat surface, image reprinted from Martin (1977) with permission.

showed that the heat transfer coefficient on the plate exhibits two radial minima: one near the stagnation point and one further away, whose location depends on the Reynolds number (Re), the jet to plate spacing (Z/D), and the nozzle shape. Researchers agree on the fact that the first peak is not at the stagnation point, but at a small radial distance from the stagnation due to the accelerated, thin boundary layer developing from the impingement region, while the second peak is due to the large-scale turbulence created in the shear layer of the jet (Viskanta, 1993).

The maximum heat transfer is achieved when the plate is placed at a distance corresponding to the start of the transitional zone of the jet, which is between 6 and 7 jet diameters from the nozzle (Livingood and Hrycak, 1973). This is usually more than what is feasible in turbomachinery cooling applications due to design constraints, unless the diameter of the jet is extremely small.

Many correlations exist in the literature for the maximum Nusselt number Nu, a non-dimensional heat transfer coefficient. They usually take the form $Nu \propto [Re^n, Pr^m]$ (e.g. Metzger, 1962; Walz, 1964; Brdlik and Savin, 1965), with n between 0.5 and 0.87, depending on the source. For the Prandtl numbrer exponent, the original Dittus-Boelter equation for circular tubes differentiated the scaling factor between heating (m=0.3) or cooling (m=0.4) the solid (Winterton, 1998). For impingement cases, m is usually set to $1/3$, although in some studies a value of 0.36 (Walz, 1964) or 0.37 (Metzger, 1962) is found to provide a better scaling. It has to be noted that these correlations are only applicable to the particular settings of the experiments used to gather the data, particularly the nozzle to plate diameter and the nozzle geometry.

More complex configurations like jets impinging on non-planar (Gau and Chung, 1991;

McDaniel and Webb, 2000; Choi et al., 2000) or inclined (Sparrow and Lovell, 1980; Goldstein and Franchett, 1988; Ward et al., 1991) surfaces have been studied, as well as non-circular jets (Ho and Gutmark, 1987; Sang-Joon et al., 1994).

2.2.3 Impingement arrays

In an array of impinging jets, the interaction between jets has to be taken into account. Several forms of interaction can take place depending on the configuration:

- Jet to jet interaction: if the jets are very close to one another, and the nozzle to plate distance is large, the shear layers of the jets can interact with each other.
- Wall jet flow interaction: the surface flows from adjacent jets interact with each other forming a second stagnation point. Depending on the conditions, large recirculations can form between the jets and a fountain flow can arise from the second stagnation.
- Crossflow: the wall jet from one jet interacts with the jets placed downstream. One can distinguish between minimum, partial and maximum cross-flow, based on how the spent air from the jets exits the channel (see Fig. 2.3).

For the case of a multi-jet configuration, additional parameters have an influence on mean and maximum heat transfer, most notably the arrangement and spacing of the jets. For example, Metzger et al. (1979) studied 2 dimensional arrays of jets (inline and staggered) with crossflow. Many researchers have come up with their own correlation for the mean Nusselt number on the plate Obot and Trabold (e.g. 1987), Van Treuren et al. (1996), Bailey and Bunker (2002), Meola (2009), usually as a function of the jet spacing, the Reynolds and Prandtl numbers, the jet to plate distance, the jet arrangement, and the crossflow. Again, each correlation is valid only under the conditions used in the tests. Today, the most applied correlation to predict the heat transfer of arrays of impingement

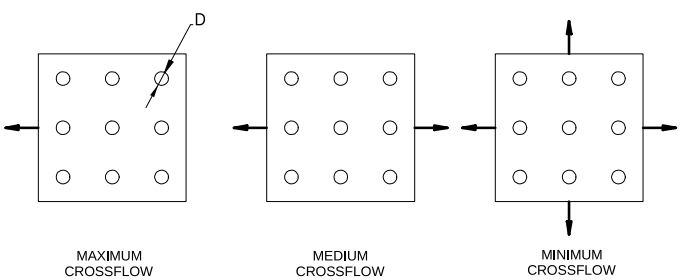

Figure 2.3 – Crossflow configurations of an impingement array are defined based on how the spent air exits the cooling channel (blue lines). Image adapted from Martínez-Filgueira et al. (2019) ©CC-BY.

jets is the one of Florschuetz et al. (1981). A thorough review of these correlations has been performed by Weigand and Spring (2011).

In general terms, the crossflow has a negative effect on the heat transfer of the impinging jets, since it can deflect them and reduce their impact angle on the surface. The degradation has more effect at large nozzle to plate distances. When considering the average Nu, however, the nozzle to plate distance has a minor effect, since two counteracting effects are at play: the detrimental effect of the crossflow is more pronounced at high jet to plate distances. At low jet-to-plate distances, however, the higher pressure losses along the channel have an influence on the massflow distribution between the jets: the upstream jets have lower massflow, which reduces the local heat transfer, and the downstream jets have higher jet velocity, counteracting the increased crossflow effect.

A particular case of impingement array is the so-called narrow impingement: a single or double row of impinging jets in which the effect of the lateral walls is non-negligible from a fluid dynamics or heat transfer point of view. The wall-jet region interacts with the lateral walls, as well as with the downstream jets, giving rise to complex flow features. This type of channels is frequently used for turbine blade cooling, and therefore subject to extensive studies. Al-aqal (2003) studied the heat transfer on the target plate and the jet plate of a narrow impingement channel, followed by Ricklick et al. (2010), who determined the contribution of the sidewalls on the total heat transfer capability of the channel. Terzis (2014) thoroughly investigated narrow impingement channels, including ways of reducing the detrimental effect of crossflow by means of varying the channel cross-section (Terzis et al., 2016b) or the jet diameter (Terzis et al., 2015). Investigations on staggered jets found that the average heat transfer is decreased compared to an inline arrangement; however, the heat transfer on the sidewalls is increased due to a more pronounced secondary impingement of the wall jet flow onto the sidewall, the stagnation points of the jets being closer to the sidewalls. According to Claretti et al. (2013), the maximum heat transfer is obtained at a jet to plate distance of 3 jet diameters, when considering the heat transfer contributions of both the target plate and the side walls.

2.2.4 Sequential impingement channels

To limit the detrimental effect of the crossflow on the downstream jets, after a certain number of jets the spent air can be brought to a second plenum and re-used for impingement. This has the effect of resetting the crossflow. Several patents have been filed on the subject (Downs and Fedock, 2012; Plank et al., 2012; Jones et al., 2013; Jones, 2017; Liu, 2017), but at the time of starting this investigation, no scientific studies were available in the open literature. In parallel to the present work, Siemens Industrial Turbomachinery also started investigating a similar impingement solution, which they call multi-stage impingement, with a numerical study of a triple sequential channel published at the end of 2020 (Liu and Zhang, 2020a,b). They report improved heat transfer distributions compared to a single channel but with much higher pressure losses. However, experimental data for this cooling solution, and analyses of different arrangements are still lacking.

2.3 Heat transfer enhancement devices

For internal convective cooling, ribs or pin-fins can be added to the channel to enhance the heat transfer. The increase of the total heat convected into the flow is due to two factors: on the one hand, the surface of the channel is increased, thus increasing the area available for heat transfer. On the other hand, the features disrupt the flow in the channel, and create vortices and turbulence that enhance the mixing of the flow, letting the bulk flow come into contact with the hot surface.

2.3.1 Ribs

Ribs are generally used in the central part of turbine blades in multipass convective channels, often on both the top and bottom surface of the passage. The most simple arrangement involves rectangular (often square) ribs placed at 90° with respect to the flow. The rib causes a separation of the flow, that then reattaches on the surface at some point downstream of it, increasing the heat transfer coefficient near the reattachment location. It also creates a recirculating flow between the rib and the reattachment line. Ribs with angles of less than 90° create vortices and secondary flows in the spanwise direction.

Among the most significant parameters for the ribs performance are the channel aspect ratio (AR), the rib height and pitch and the angle of the rib with respect to the incoming flow. Han and Park (1988) studied inclined ribs and found that the heat transfer increases significantly on one side of the channel, 30% to 50% higher than in the centerline, due to the secondary flow. In the same study they analyzed the influence of the channel AR, and found that for an aspect ratio Y/Z equal to 4, orthogonal ribs performed best, while for lower aspect ratios (Y/Z=1) the inclined ribs were better, with the 60° ribs showing the highest improvement. Han et al. (1991) then studied V-ribs and chevron ribs,

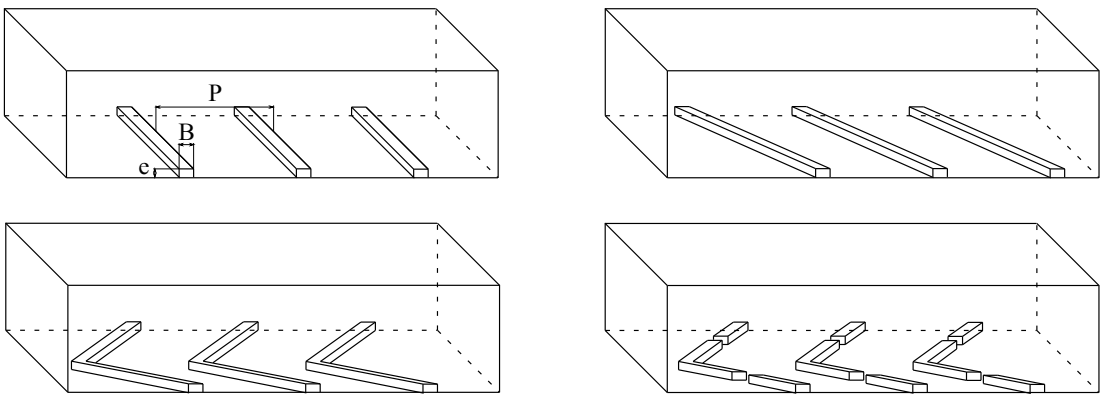

Figure 2.4 – Examples of ribbed configurations. From top to bottom, left to right: 90° ribs, inclined ribs, V-ribs, broken V-ribs. Flow from left to right.

among others, on a square channel finding that the 60° ribs produce more heat transfer enhancement and more pressure losses than their 45° counterparts.

To further increase the Nusselt number, the ribs can be separated in two or more segments ("broken ribs", see also Fig. 2.4, bottom right). Cho et al. (1999) analyzed this type of ribs and found that for 90° ribs the thermal performance increased slightly and for 45° it decreased slightly. Wright et al. (2004) found that discrete V-ribs (i.e. with one half of rib the moved half a pitch downstream) had higher performances than continuous V-ribs in non-rotating channels with AR=4.

Experimental studies often consider rib heights between 5 and 10% of the channel hydraulic diameter, and pitch over rib height ratios between 7 and 15. In a real blade, however, the rib is often higher and the pitch smaller (Han et al., 2012). This fact has been taken into account for the design of the rib configurations investigated in this study.

2.3.2 Pins

Pins act like a cylinder in cross-flow generating wake shedding. Contrary to the extensively studied cylinder flow, in this case, the cylinder is placed in an internal flow, so that it is bound by one (or two) surfaces, and consequently a horseshoe vortex is formed just above the pin-mounted surface (see Fig. 2.5). These 2 phenomena, and their interaction, increase the heat transfer on the target plate both upstream and downstream of the pin (Goldstein et al., 1985; Chyu and Natarajan, 1996). When placing pins in an array, the most common configurations are in-line and staggered. The staggered arrangement provides higher heat transfer augmentation but with higher losses (Sparrow and Lovell, 1980; Chyu et al., 1999). VanFossen (1982) studied short pins inclined on an axis parallel to the flow direction, with successive rows inclined in the opposite sense. He found that the performances with respect to the heat transfer coefficient on the target plate are

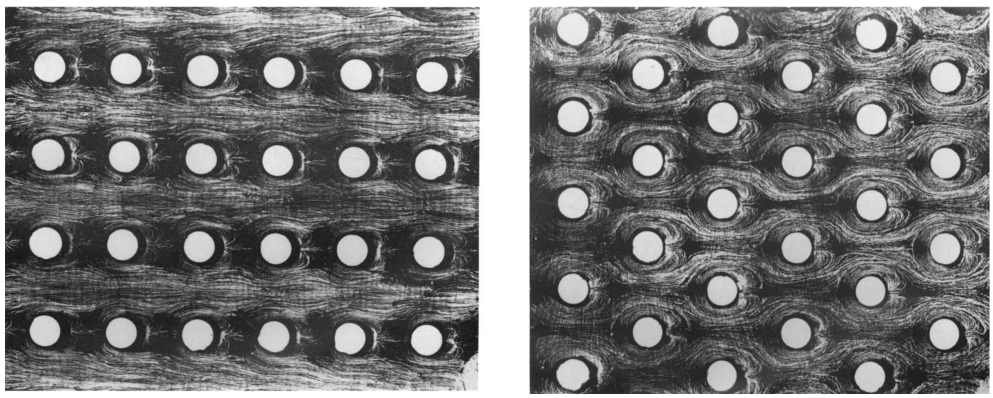

Figure 2.5 – Oil flow visualization of inline (left) and staggered (right) pin arrangments. Flow from left to right. Reprinted from Sparrow and Molki (1982) with permission.

similar to vertical pins, but the increased surface-area of the pin compared to the vertical arrangement makes this a favorable choice. No other studies with this interesting pin arrangement have been found, in particular for longer pins, with recent studies focusing on pins rotated around an axis normal to the flow direction (Chyu et al., 2007; Park et al., 2010).

2.4 Experimental techniques

Experiments that aim to investigate the convective cooling or heating properties of a flow on a solid generally look at the temperature evolution at the surface of the solid to infer the convective heat transfer coefficient of the flow at each point on the surface.

Thanks to the achievable spatial resolution and low intrusiveness, thermochromic liquid crystals have been extensively used for temperature measurement to determine the convective heat transfer coefficient of a fluid heating or cooling a solid (Waidmann et al., 2018), and the performances of heat exchangers (Fiebig et al., 1993) and cooling systems of gas turbine blades (e.g. Poser and von Wolfersdorf, 2009). Other important applications include the determination of the film cooling effectiveness (Vogel et al., 2003; Ekkad et al., 2004; Jonsson et al., 2008) and the measurement of the surface shear stresses (Reda et al., 1997; Buttsworth et al., 1998).

Alternative methods to determine the heat transfer coefficient with low intrusiveness and high resolution include temperature sensitive paint (TSP Lee et al., 2007; He and Liu, 2018), infrared thermography (Ay et al., 2002; Carlomagno and Cardone, 2010; Modak et al., 2017), and the naphthalene sublimation method, which determines the heat transfer coefficient via a heat/mass transfer analogy (Häring, 1995; Goldstein and Cho, 1995).

Many studies drive the experiment via a surface heat flux produced by electrically heating a thin metallic foil on low conducting materials to obtain local heat transfer data in steady state experiments. By considering appropriately the heat losses and lateral conduction effects (e.g. Satta and Tanda, 2014; Sarkar et al., 2016; Ratto et al., 2018) low uncertainty (about 5-8%) in the obtained heat transfer coefficients can be achieved. Less frequently, heat is provided by keeping the opposite side of the solid at a uniform temperature via a liquid bath (Hoogendoorn, 1977; Van der Meer, 1991; Goldstein and Franchett, 1988).

Alternatively, transient measurements can also be performed by instantaneously powering the heater foil, but this generally leads to higher uncertainties due to the additional transient effects. Instead, transient methods usually rely on a step change of the flow temperature (Jones and Hippensteele, 1988; Ekkad and Han, 2000; Ansu et al., 2017), and the time required to reach a certain color of the liquid crystals allows for the determination of the heat transfer coefficient, usually assuming one dimensional heat conduction into a semi-infinite solid, provided that the assumption is sound (Schultz and Jones, 1973; Vogel and Weigand, 2001), although corrections for lateral conduction have been proposed (Ling

et al., 2004; Kingsley-Rowe et al., 2005; von Wolfersdorf, 2007; Brack et al., 2016). Methodologies for more complex temperature evolutions have also been developed: a series of steps can be assumed (using Duhamel principle) to account for the temperature evolution at the beginning of the experiment which differs from an ideal step (Metzger and Larson, 1986; Terzis et al., 2014a); alternatively, a ramp (Ma et al., 2016) or a series of ramps can be prescribed, which can improve the accuracy of the method. Analytical solutions of the heat equation for flow temperature evolutions described as polynomials (Kwak, 2008) or as a sum of exponential functions (Newton et al., 2003) have been obtained; these allow to better approximate the real temperature evolution.

A transient method using a surface heat flux is appealing because it avoids several problems associated with a flow temperature based approach:

- the step change is almost instantaneous, which facilitates the implementation by eliminating the need for redirecting the hot flow or accounting for the thermal inertia of the heater mesh (Gillespie et al., 1998) and thermocouples (Terzis et al., 2012),
- the thermal inertia of the thermocouples has no effect on the experiment (the flow temperature being constant) and no correction is needed.
- the flow is kept at ambient temperature, eliminating the problem of the determination of the driving gas temperature, which can be a difficult task in complex flows, especially when mixing processes occur, for example in a multi-channel device with bypasses between channels, as is the case in the work presented here.

At the beginning of this project, heat transfer experiments in the laboratory relied on a transient technique based on a step change in the flow temperature. However, the very long passages of the sequential impingement channel and the bypasses between channels present in some of the configurations call for the development of a transient technique based on a surface heat flux.

2.5 The contribution of the thesis

The present study aims to investigate experimentally the sequential impingement channels and provide performance data in terms of heat transfer coefficients and pressure drop along the channels, which are currently missing from the literature. In order to accomplish this, the following tasks are required:

- Adaptation and improvement of the existing impingement test bench. The test bench needs to be re-validated because several critical parts have been changed (e.g. laminar flow element, vacuum pump) since the last project. Additionally, some modifications are required to install the sequential channels.

- Development and validation of a new experimental technique based on a surface heat flux to cope with the multi-channel configurations with possible bypasses between them (3 temperature problem).
- Determination of the heat transfer coefficient, with high spatial accuracy, on the target plates of both channels for a wide range of sequential impingement configurations, at engine representative Reynolds numbers, including heat transfer augmentation features like pin-fins, ribs, cross-section reductions, bypasses between channels, and combinations thereof.
- Determination of the pressure losses along the channel with emphasis on the impact of the choice of the heat transfer augmentation devices on the losses.

The present work contributes to the state of the art by providing high resolution experimental data regarding the heat transfer coefficient of sequential impingement channels, as well as pressure losses. These data, now available in the open literature, are useful for the design of cooling systems in gas turbines applications, as well as for the validation and calibrations of numerical tools.

Chapter 3

Experimental setup

In this chapter the experimental setup used for the tests is outlined, as well as the associated instrumentation. Since the validation of the experimental technique has been performed on a single impingement case, the associated setup is also described in Section 3.4; this section was first presented in Schmid et al. (2021). Additionally, Section 3.5 describes the geometries investigated.

3.1 Introduction

The experimental assessment of the sequential impingement channels is performed on EPFL's impingement cooling test rig, which has been developed in the frame of a previous project (Terzis, 2014). Several modifications have been made to the setup, in order to adapt it to the more complex geometries investigated in this work, to implement the new measurement technique, and to increase the accuracy of the acquired data.

3.2 Wind tunnel

A schematics of the wind tunnel is depicted in Fig. 3.1 (see also the image in Appendix D, page 111). It is an open circuit setup operated in suction mode by a vacuum pump controlled using a frequency converter. Air is brought into a plenum of rectangular cross-section via a bellmouth inlet. Stainless steel heater meshes are installed in the plenum and allow to heat the incoming flow if required. On top of the plenum the channel to be tested is installed. At the channel exit, a flange connects the channel with a laminar flow element (LFE), to measure the mass flow, which is then connected via a flexible pipe to the inlet of the vacuum pump. Care must be taken to ensure that suction pipes are used, which are able to withstand the under-pressure caused by the operation in suction mode. The various elements of the wind tunnel are briefly described hereafter.

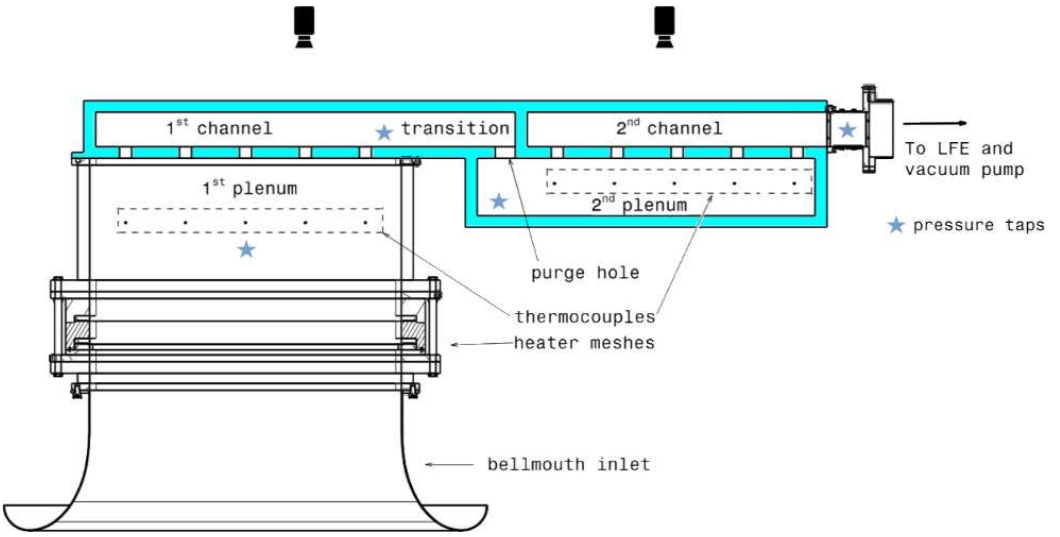

Figure 3.1 – Schematics of the experimental setup with the test channel in cyan.

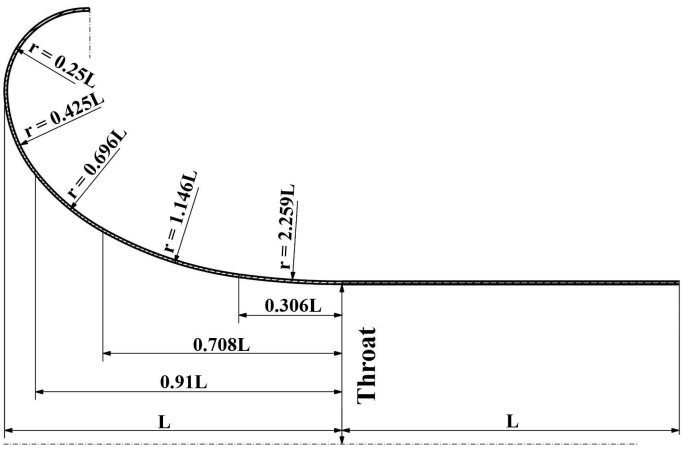

Figure 3.2 – Profile specifications of the bellmouth inlet, adopted from Terzis (2014).

3.2.1 Inlet

The bellmouth inlet has been designed according to McKenzie (1966); the general dimensions are shown in Fig. 3.2. The contraction ratio is 4.5. Downstream of the inlet an air filter and a honeycomb are installed to block particles possibly present in the incoming air (dust) and to smooth the flow.

3.2.2 Heater meshes

The stainless steel (DIN EN 1.4401) heater meshes were used in the previous project, in which the heat transfer experiments were driven by a step in the flow temperature. They are kept in the plenum for two reasons. First, the experimental technique developed in this project has been cross-validated by performing experiments with a step-change in the

flow temperature and comparing the results with those obtained with the new technique. Secondly, the very fine meshes (wire diameter 25μm, open area 25%) allow to eliminate the boundary layer of the bellmouth inlet and to reduce the turbulence length scale of the flow. The meshes are connected in parallel to a 30 kW DC power supply, (maximum rating of 500 A and 60 V) using copper bars at their extremities.

3.2.3 First plenum

The rectangular plenum, of dimensions 520 mm x 150 mm, is made of wood, whose low thermal conductivity allows to limit the heat losses and achieve a temperature increase as close to a perfect step as possible when heating the flow. A second honeycomb is installed downstream of the heater meshes. On top of the wooden section, an aluminum plate allows for the connection of the test channels.

3.2.4 Pump

A new vacuum pump has been purchased that is more adapted to the massflow required for the tests than the pump used in Terzis (2014). The Elektror HRD 60 FU-135/11 is a radial boosted high pressure blower driven by a three phase AC motor. The motor is controlled using an Omron MX2 pulse width modulation (PWM) frequency converter, which ensures a finer control of the volumetric flow than the throttle valve used previously. The main characteristics of the pump are the following:

Volumetric flow rate:	36 m^3/min
Total pressure difference:	14100 Pa
Voltage:	400 V (3-phase, triangle connected)
Frequency:	35-135 Hz
Max current:	21 A
Number of revolutions:	7965 min^{-1}
Power:	11 kW

Volumetric flow rate and total pressure difference refer to the vacuum side of the pump.

3.3 Instrumentation

To perform the heat transfer tests, knowledge of local temperatures and pressures is needed. For the determination of the Reynolds number, the mass flow must be known. Additionally the electrical power input to the heater foil has to be determined, and a video recording of the tests is needed to track the liquid crystal color change over time. Most of the instrumentation is controlled using a custom LabVIEW program using equipment connected via universal serial bus (USB) or via the network (Ethernet).

3.3.1 Pressure measurements

The pressure drop through the channel is measured with a digital pressure scanner (DSA 3217), which has an analog to digital converter with 16 bits of resolution and has an accuracy of ±8 Pa. For steady state measurements, repeated measurements can be performed and averaged to reduce the scatter of the results. It has a range of ±6.9 kPa. The device is zero-calibrated before each test, and the data are retrieved through a TCP/IP connection via LabVIEW. Since only pressure differences between various pressure probes are required, zero calibration is considered adequate.

Four pressure taps, one on each side of the wooden plenum, are connected together to provide the pressure level upstream of the test channel while reducing the effect of residual non-uniformities in the flow to obtain an average value of the static pressure. The same is done at the outlet, so that the pressure drop of the complete channel can be measured. Additionally, the channel itself is instrumented with static pressure taps to retrieve information on the pressure losses of selected parts of the channel. See Fig. 3.1 for the locations of the taps on the channel.

3.3.2 Temperature measurements

Temperature measurements are made using K-Type thermocouples, with very thin hot junctions (the wire diameter is 80 μm) to reduce the thermal inertia for tests driven with a temperature step. To correct for the thermal inertia, the temperature evolution data are post-processed assuming an ideal step in the temperature change; the response of the thermocouple is modeled as a first-order, linear time-invariant system. This is a reasonable assumption, since the thermocouple's hot junction is small and of high thermal conductivity, and can therefore be considered a lumped capacitance.

Under these assumptions the real temperature evolution T can be derived from the measured temperature $\hat{T}$ with the following formula:

$$T(t) = \hat{T}(t) + \tau \frac{d\hat{T}}{dt} \tag{3.1}$$

where τ represents the time constant of the first order system, and in practice is equal to the time required to reach 63.2% of the steady-state temperature. Obviously, the real temperature evolution is not a linear step, since the heater meshes have some thermal inertia of their own, and the side walls of the plenum are not perfect insulators. Nevertheless, this approach has been used satisfactorily in the past (Terzis et al., 2012).

Thermocouples are calibrated in a thermostatic bath (Lauda Eco E4S, temperature stability ±0.01K) using a precision platinum resistance thermometer (Omega DP251, resolution 0.001^oC, accuracy ± 0.01K). Thermocouple voltage signal acquisition, conditioning, and

processing are all performed using a National Instruments 9213 DAQ. The analog-to-digital conversion is done with full resolution when measuring a constant temperature and with reduced resolution but higher frequency when dealing with steep temperature gradients, namely when measuring temperature steps.

One thermocouple is placed upstream of each impingement hole (maximum 14 thermocouples). Additionally, two thermocouples are placed upstream of the heater meshes and directly upstream of the test channel, to detect the start of the experiment when it is driven by a step change in the flow temperature. Finally, one thermocouple is installed upstream of the LFE and is used to determine the massflow (see next section).

3.3.3 Mass flow measurement

The laminar flow element (Tetratec 50MH10-04) is mounted downstream of the channel outlet. Its function is to determine the mass flow through the test geometries with high accuracy and low pressure losses. The working principle is simple: the flow passes through a fine mesh, creating a pressure difference between the upstream and downstream sides of the mesh. Using a calibration curve, the measured pressure losses can be converted into the corresponding volumetric flow. A correction has to be made to take into account the viscosity variation of the fluid due to the flow temperature difference between the calibration data and the tests. For this, a thermocouple is installed upstream of the laminar flow element. The temperature information, along with the pressure level upstream of the LFE is also used to calculate the air density, which is then used to derive the massflow rate from the volumetric flow. The LFE has been purchased at the beginning of the project and was calibrated by the manufacturer. Stainless steel tubes (length 10x and 5x the inner diameter of the LFE) connect the LFE to the flexible tubing, ensuring that the flow is fully developed at the LFE inlet and that the conditions correspond to those of the calibration. The characteristics of the LFE are the following:

Inner diameter:	102.5 mm
Length:	203.2 mm
Volumetric flow:	0-4500 l/min
Massflow:	0-5.430 kg/min (at 1.013 bar and 21.1 ^oC)
Pressure losses:	0-20 $mbar$
Pressure connections:	1/4″ NPTF
Operating condition limits:	0.4-6.0 bar and 0-70 ^oC
Material:	stainless steel
Accuracy:	0.4% of full scale

The average jet Reynolds number, based on the jet diameter D and the average jet velocity u_j, can be derived directly from the massflow $\dot{m}$:

$$Re = \frac{\rho u_j D}{\mu} = \frac{4\dot{m}}{nD\mu\pi} \tag{3.2}$$

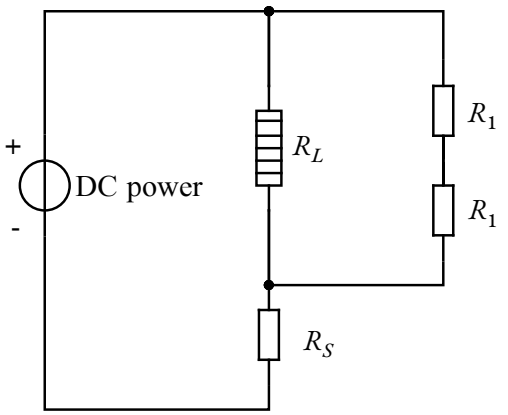

Figure 3.3 – Schematics of the electrical setup.

where n is the number of impingement jets and μ is the dynamic viscosity of the fluid.

For the determination of the ambient pressure, a precision barometer (Druck DPI 141, accuracy ± 8 Pa) was used while the flow temperature was measured using a K-type thermocouple directly upstream of the LFE; this results in a maximum uncertainty of 3% for the Reynolds number determination at the lowest Reynolds number investigated (Re=10,000). Higher Reynolds numbers have lower relative uncertainty.

3.3.4 Voltage and current measurements

When the experiment is driven by a surface heat flux, an accurate measurement of the applied heat flux is required. This is achieved by measuring the voltage drop and the current through the heater foil. Figure 3.3 shows a schematics of the electrical setup; the current is determined by measuring the voltage drop across a shunt resistance R_S (0.6 $m\Omega$ ± 0.5%) in series with the load R_L (i.e. the heater foil). The voltage drop through the load cannot be measured directly because its magnitude exceeds the limits of the instrumentation available. A voltage divider, consisting of 2 resistors R_1 (100 $k\Omega$) connected in parallel with the load, allows to measure the voltage drop across one of these resistors, which is equal to 1/2 of R_L.

Voltage across the shunt is measured with a NI 6211 DAQ, while the voltage across R_1 is measured with a NI 9201 DAQ. The DC power supply used (Agilent 6684A) can deliver up to 128 A at 40 V and is controlled via its analog input module through a NI 9263 DAQ.

3.3.5 Video capture

The temporal evolution of the liquid crystal colors on the surface under investigation is required in order to determine the moment at which the liquid crystals show their maximum

green intensity, which is then used to derive the heat transfer coefficient via the heat equation. Two CMOS (Complementary metal–oxide–semiconductor) digital cameras are used for the video recording.

Cameras (IDS-imaging UI-3180CP) have a 5.3 Mpixel, 1 inch sensor, allowing a highly resolved image of the surface, and are connected to the computer via a USB 3.1 connection, directly writing to a NVMe connected solid state storage device to allow a high frame rate. The frame rate was set to 50 fps to limit the storage space required, since increasing it further would not have had any meaningful increase of accuracy (see Section 4.4.1).

A fairly long-focus lens is used (Kowa, 25mm F1.4, C-mount version, approximate angle of view 28°) to eliminate the barrel distortion often associated with wide-angle lenses. This requires to place the camera at a certain distance from the subject. The high aperture of the lens allows to increase the amount of light reaching the sensor in order to achieve high frame rates without increasing the gain, which can introduce numerical noise in the acquired images. However, the high aperture translates to a small depth of field, and consequently, care must be taken to ensure that the surface is in focus.

Two LED lights (Philips WT120C G2), placed above the surface, one on each side, provide the required illumination and avoid shadows. LED lights usually provide continuous illumination, but the power supply integrated in these specific units does not provide a perfect direct current to the LED, probably due to a low quality rectifier, which is adequate for normal use, but creates a noticeable flicker when recording at high frame rate. The typical 100 Hz ripple of a full wave rectifier has been reduced by placing a capacitor (capacitance: 1.5 mF) in parallel with the LED.

The video recording begins before the start of the experiment; a LED light placed into the field of view and commanded from the same DAQ system as the power supply is used to detect the precise start of the experiment (i.e. the start of the heating phase). For the experiments performed using a step heating of the flow (heater mesh method), the LED light is turned on when a temperature difference is detected between the upstream and downstream sides of the heater meshes.

3.3.6 Thermochromic liquid crystals

In order to obtain a spatially resolved indication of the surface temperature, thermochromic liquid crystals are used. Liquid crystals change color from red to blue in a certain range of temperatures and are transparent outside of the range (see also Section 4.1.1 for a more detailed description). In this project narrow band liquid crystals (Hallcrest R38C01W) are used to ensure maximum precision in the temperature determination. The bandwidth (from red to blue) is $1K$ and the red color starts at approximately 38^oC.

3.4 Single impingement facility

The impingement test facility used for the validation of the experimental technique is depicted in Fig. 3.4. It consists of an open-circuit, low-speed wind tunnel operated in blowing mode using two counter-rotating axial fans. A settling chamber with honeycombs, a convergent bell mouth and a straight square section (100 mm side) complete the wind tunnel. A 15 mm thick jet plate is mounted at the end of the tunnel. The jet hole has a diameter D=15 mm resulting in a nozzle of length-to-diameter ratio equal to one (L/D=1). The large hole diameter was mainly chosen in order to increase the spatial magnification ($pixels/D$) in the measurement and to avoid compressibility effects (Fénot et al., 2019).

The mass flow was determined by means of the discharge coefficient using the difference between the pressure upstream of the jet and the ambient pressure.

$$\dot{m} = C_D A \sqrt{2\rho\Delta p} \tag{3.3}$$

where A is the jet area, and the discharge coefficient C_D was determined a priori by measuring jet velocity profiles with a traversing Pitot probe and Δp at various mass flows (Figure 3.5). The pressure is measured with the same scanner as for the multi impingement setup (Scanivalve DSA 3217). The Reynolds number, based on the jet diameter, follows directly from Eq. 3.3:

$$Re_D = C_D D \frac{\sqrt{2\rho\Delta p}}{\mu} \tag{3.4}$$

The uncertainty in the Reynolds number determination was estimated at or below 4%, similar to previous experiments carried out on this setup (Caggese et al., 2013).

3.5 Test models

To comply with the semi-infinite hypothesis assumed to post-process the experimental results (see Section 4.2), the test models are built using 20 *mm* thick PMMA plates, in

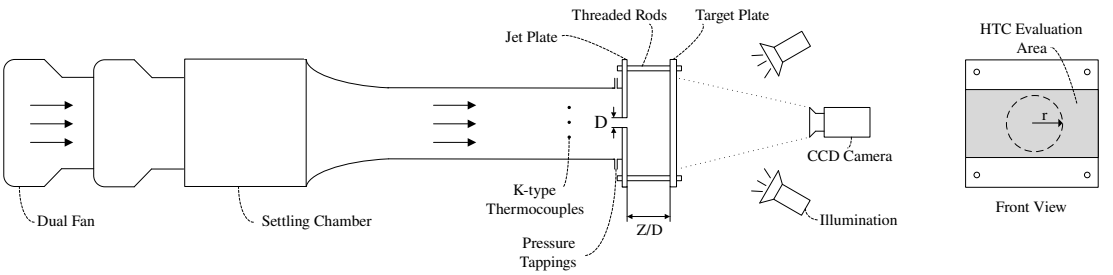

Figure 3.4 – Schematic representation of the experimental setup used for the validation of the experimental technique and front view of the target plate.

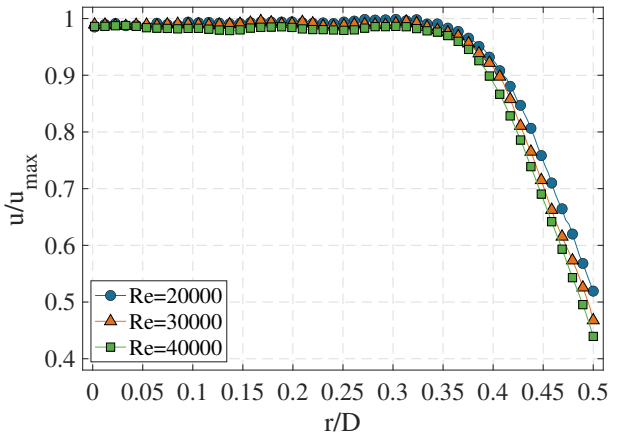

Figure 3.5 – Traversed velocity profiles for different Reynolds numbers at Z/D=6.

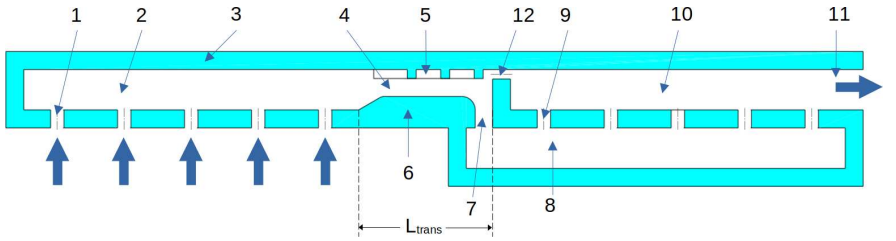

Figure 3.6 – General layout of the impingement channels tested.

a modular way to be able to easily swap parts and modify the channel characteristics. A view of a generic channel which includes most of the features investigated is depicted in Fig. 3.6. First, the cooling air flows through the impingement holes (1) into the first channel (2) and impinges on the target plate (3). It then flows in the transition zone (4), which can be equipped with ribs (5), ramps (6) and/or pins (not pictured here). The air then discharges through a purge hole (7) into the second plenum (8). It can then pass through the second level impingement holes (9) into the second level impingement channel (10) before discharging (11). A bypass hole (12) is present in some configurations to allow some of the flow to go directly from the first to the second channel.

The internal surface of the target plate of both channels is painted with a thin layer of TLCs of approximately 10 μm (measured with an Elcometer 456 Coating Thickness Gauge), and a layer of black paint of the same thickness (see Fig. 3.7). On top of it, a 30 μm thick metallic foil is attached using a 127 μm thick thermal pad (3M 8805). The foil material is an iron-chromium-aluminum alloy with low temperature coefficient (alloy 1.4767, α_T=0.0193x10^{-3} K^{-1}). Therefore, the resistivity of the material can be considered constant during the experiment, and the current density can be considered uniform across the foil even if the temperature field is not. Electrical contacts are provided by copper bars that sandwich the ends of the foil. The bars are placed in a slot in the endwalls.

The channel cross-section is held constant for all configurations, although the transition zone height can vary; the channel width Y/D is equal to 5 (D being the jet diameter), while

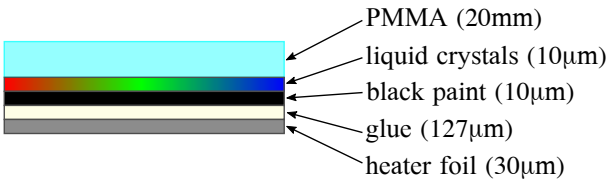

Figure 3.7 – Instrumentation of the target plate for the heater foil method. Thicknesses are not to scale.

the jet-to-plate distance Z/D is equal to 3. This jet-to-plate distance has been chosen since it was shown that it maximizes the thermal performances of the channel when considering both the target plate and the sidewalls (Claretti et al., 2013). The jet-to-jet spacing X/D is equal to 5. The flow discharges into the second plenum via an obround purge hole with a surface area 10 times bigger than the jet hole area.

In total, 34 different geometries were tested at three engine relevant Reynolds numbers of 10,000, 20,000, and 40,000. The baseline geometry has 5 jets per channel, a transition zone of length $10D$, and no additional features. In a first step, the number of jets per channel and the length of the transition zone were varied, and for some configurations bypass holes or cross-section reductions were added. In a second phase, heat transfer enhancing features like ribs and pins were added to the baseline configuration. Finally, based on the results of the first two test campaigns, various features were combined to improve the performances of the channel in terms of heat transfer and pressure drop. Table 3.1 lists the configurations tested; the configuration name is built using the number of jets in the 1st and 2nd channel, and the length of the transition zone. An alphanumerical code is appended for the enhancing features.

Configuration codename	# holes 1st channel	# holes 2nd channel	Transition length	Enhancing features / Notes
5510	5	5	10D	None, baseline geometry
5505	5	5	5D	None
5515	5	5	15D	None
7505	7	5	5D	None
7510	7	5	10D	None
7705	7	7	5D	None
7710	7	7	10D	None
5505B1	5	5	5D	Central bypass
5505B2	5	5	5D	2 lateral bypasses
5510B4	5	5	10D	4 bypasses
5510BR	5	5	10D	Baseline ribs (inclined ribs 45°)
5510VR45	5	5	10D	V-ribs 45°, 1st rib upstream of last jet
5510VR45B	5	5	10D	V-ribs 45°, 1st rib downstream of last jet
5510VR45R	5	5	10D	V-ribs 45° + short ramp, height 2D
5510VR60	5	5	10D	V-ribs 60°,1st rib upstream of last jet
5510VR60B	5	5	10D	V-ribs 60°, 1st rib downstream of last jet
5510CR45	5	5	10D	Chevron ribs 45°
5510DV45	5	5	10D	Discrete V-ribs 45°
5510DV45BP	5	5	10D	Discrete V-ribs 45° + central bypass
5510DV60	5	5	10D	Discrete V-ribs 60°
5510DCR	5	5	10D	Discrete chevron ribs
5510VP	5	5	10D	Vertical pins (baseline pins)
5510VPS	5	5	10D	Small vertical pins
5510IP	5	5	10D	Inclined pins
5510R1	5	5	10D	Short ramp, height 2D
5510R2	5	5	10D	Long ramp, height 2D
5510RS	5	5	10D	Short ramp, height 1D
5510DCRR	5	5	10D	Discrete chevron ribs short ramp, h=1D
5510DCRR1	5	5	10D	Discrete chevron ribs short ramp, h=2D
5510DVRR	5	5	10D	Discrete V-ribs short ramp, h=1D
5510DVRR1	5	5	10D	Discrete V-ribs short ramp, h=2D
5510PR	5	5	10D	Pin-ribs
5510PRR	5	5	10D	Pin-ribs, with short ramp, h=1D
5510PRBP	5	5	10D	Pin-ribs + bypass

Table 3.1 – List of the configurations tested, divided into 3 test campaigns.

Chapter 4

Measurement technique

This section describes the measurement technique that has been developed during this study. First, a short introduction to thermochromic liquid crystals is given, after which the newly developed experimental technique is presented in Section 4.2. In Section 4.3, the procedure used for the calibration of the liquid crystals is outlined, while Section 4.4 reports the validation of the experimental method. Parts of Sections 4.2 and 4.4 have been published in Schmid et al. (2021).

4.1 Introduction

Many methods exist to retrieve spatially-resolved temperature information from a surface of interest, without resorting to integrate an array of temperature sensors directly into the solid. These include infrared thermography (Ay et al., 2002; Carlomagno and Cardone, 2010; Modak et al., 2017), temperature sensitive paint (TSP) (Lee et al., 2007; He and Liu, 2018), phosphor thermometry and thermochromic liquid crystals (TLC) (Stasiek and Kowalewski, 2002). In this project TLCs are chosen due to their better performances and accuracy compared to TSP, while infrared thermography is difficult to apply to internal flows since materials that are transparent in the IR spectrum are extremely expensive.

4.1.1 Thermochromic liquid crystals

TLC are cholesteric (sterol derived) or chiral nematic (non-sterol derived) molecules that have the propriety of reflecting selected wavelengths of the incident light based on their temperature. The reflection happens because these compounds aggregate in successive sheets of aligned molecules, with a distance between the sheets that is of a similar length as the wavelength of visible light, with the result that only a single wavelength of the incident white light is reflected, depending on the angle between the alignment of successive sheets, which varies with temperature: an increase in temperature corresponds

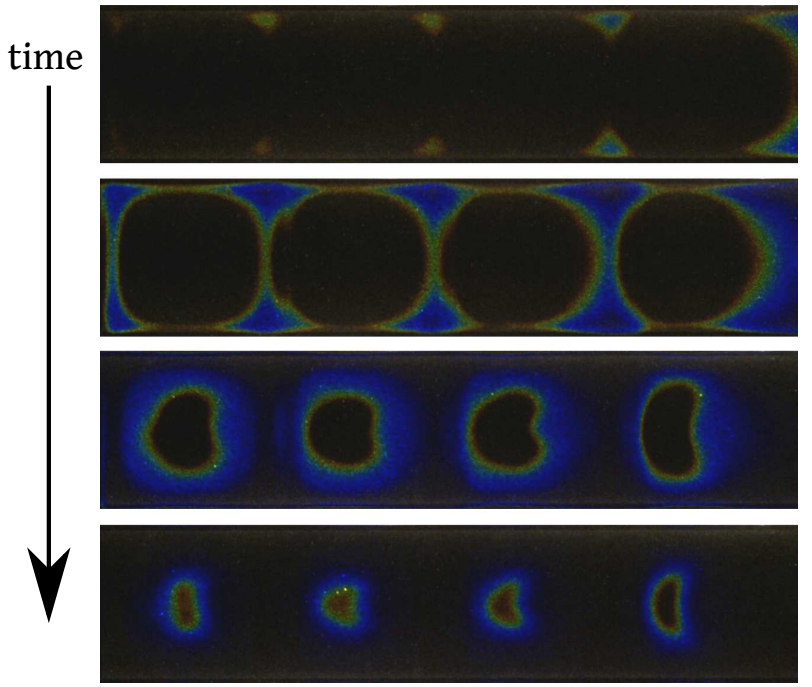

Figure 4.1 – Example of the liquid crystal evolution on the target plate during a heat transfer test. The first image is taken after approximately 45 s. from the start of the experiment, and the last after 65 s.

to a decrease of the wavelength of the reflected light. The response time to a change in temperature is in the order of milliseconds (Ireland and Jones, 1987). Since these compounds degrade quickly when exposed to air, chemicals, or UV light, they are microencapsulated (Dubey, 2009). The choice of the temperature at which the liquid crystals reflect visible light, and their bandwidth, i.e. the temperature range between the start of the red color to the start of the blue color, is application specific; narrow-band TLC can have a bandwidth as low as $1K$, while wide-band TLC can have a bandwidth up to $20K$. When a global temperature map is required, wide-band liquid crystals are favored, and the actual color is used. This is done by converting the color information, usually obtained as an RGB (red-green-blue) representation, to a HSL (hue-saturation-lightness) representation, and calibrating the correspondence of the hue to the temperature. For the experimental technique presented hereafter, only the time to reach a certain temperature is required (the temperature corresponding to the maximum green intensity is used), and narrow-band liquid crystals are chosen in order to achieve a very precise calibration of the color-temperature relationship. To reduce the uncertainty of the results, one could exploit both the red and green maximum intensity indications and/or multiple layers of TLCs with different temperatures (Terzis et al., 2016a) using a least square approach (Tran and Slabaugh, 2019). Figure 4.1 illustrates the time evolution of the TLCs during a typical test as performed in this study.

In aerodynamics, TLCs were first used by Klein and Margozzi (1969) to detect the bound-

ary layer transition. Later, their use for quantitative studies in aerodynamics and heat transfer have become common thanks to the pioneering work of Cooper et al. (1975), Hoogendoorn (1977), and Hippensteele et al. (1983), among others. Today, many groups around the world use liquid crystals for temperature mappings and heat transfer research in many areas, although its most widespread use is for turbine cooling research.

4.2 Transient heater foil technique

The sequential impingement channels that are the object of this study present a challenge with respect to the experimental technique. The heater mesh method previously developed in the laboratory is difficult to apply in this case for two reasons:

- The jet temperature evolution in the second impingement channel is very slow, since the walls of the first channel and of the second plenum are being heated during the transient experiment. The temperature can also differ between the jets in the second channel. This makes it difficult to determine the reference temperature for the convection problem.
- Some of the configurations have a bypass between the first and second channel. Due to the transient nature of the experiment, the bypass flow will be at a different temperature than the jet flow in the second channel, making the determination of the reference temperature difficult (3 temperature problem) and location specific.

To avoid these drawbacks, a new experimental technique is used: instead of heating the flow, the experiment is driven by applying a heat flux on the surface under study; the flow is kept at ambient temperature, avoiding the 3 temperature problem altogether. In the following, the new transient heater foil technique is introduced. The solution of the heat equation is also reported for the existing heater mesh technique, since it has been used to validate the experimental setup by redoing tests on geometries investigated in previous projects.

The surface heat flux is obtained by gluing a thin metallic foil on the surface under study, which is transparent (PMMA) and prepared beforehand with TLCs and black backing paint to observe the temperature evolution. By using a high resistance material with low temperature coefficient for the foil, it is ensured that the required heat flux is achieved with relatively low values of the electrical current, and that the heat flux is equally distributed across the foil, regardless of the local temperature. In this setup, the internal wall of the channel is painted with TLCs and it is observed through the PMMA.

Convective heating (or cooling) can be characterized by the heat transfer coefficient, which relates the heat flux at the surface to the temperature difference between the fluid and the solid:

$$h = \frac{q}{T_s - T_\infty} \left[\frac{W}{m^2 K}\right] \tag{4.1}$$

where q is the wall heat flux, T_s is the temperature of the solid at the wall, and T_∞ is the fluid temperature. This can also be expressed as the ratio of the convective to conductive heat transfer, a quantity known as the Nusselt number:

$$Nu = \frac{hL}{k} \tag{4.2}$$

in which k is the thermal conductivity of the fluid and L is a characteristic length of the problem. For impingement cooling, the jet diameter D is generally used as the reference length.

Fundamentally, in the transient experiment one looks at the conduction into the solid to infer the convective heat transfer. If the thermal diffusivity α of the material is sufficiently low, the lateral conduction can be neglected, so that the conduction problem can be modeled with the one-dimensional heat equation:

$$\frac{\partial^2 T(z,t)}{\partial z^2} = \frac{1}{\alpha}\frac{\partial T(z,t)}{\partial t} \tag{4.3}$$

in which the spatial coordinate z is defined from the solid-fluid interface, with the positive direction into the solid.

Suitable initial and boundary conditions are needed. Initially the solid is at a uniform temperature T_i, so that the initial condition is

$$T(z, t = 0) = T_i \tag{4.4}$$

The first boundary condition is imposed with the assumption of a semi-infinite solid (i.e. $T(z \rightarrow \infty, t) = T_i$). This assumption limits the allowed experiment duration for a given wall thickness δ or, conversely, dictates the minimum wall thickness for a given experiment duration. The criterion generally used for justifying the semi-infinite assumption is that the increase in temperature at the outer boundary is negligible; in other words, the propagation distance of the heat input must be less than the wall thickness. Schultz and Jones (1973) require that the increase of both temperature and heat flux at $x = \delta$ be less than 1%. This results in the following expression for the time-thickness relationship:

$$\delta > 4\sqrt{\alpha t} \tag{4.5}$$

With similar reasoning, but disregarding the heat flux requirement, Boelter (1946), and later Schack (1969), proposed a limit of:

$$\delta > 3.6\sqrt{\alpha t} \tag{4.6}$$

More recently, Vogel and Weigand (2001) assessed these requirements for transient liquid crystal applications by comparing the finite and semi-infinite approaches. Since in this

type of experiment one is only concerned with the temperature evolution near the fluid-solid interface (i.e. at $z = 0$), the criterion is less strict, and it was concluded that a semi-infinte assumption yelds satisfiying results if:

$$\partial > 2\sqrt{\alpha t} \tag{4.7}$$

Assuming a maximum experiment time of 2 minutes, the most stringent criterion imposes a wall thickness of 14.4 mm. In this project, PMMA plates of thickness 20 mm are used; the semi-infinite assumption is thus sound, and the maximum experiment time would be 230 seconds using the most stringent criterion.

Essentially, the experimental methods differ on the boundary condition at $z = 0$, i.e. on how the experiment is driven. For the heater mesh method developed e.g. in Terzis et al. (2016a), the gas temperature suddenly increases from T_i to T_g at the beginning of the experiment, and the boundary condition becomes:

$$-k\frac{\partial T(z=0,t)}{\partial z} = h[T_g - T(z=0,t)] \tag{4.8}$$

Radiation effects are neglected since the temperatures involved are low. With the boundary condition 4.8, Eq. 4.3 can be solved according to Carslaw and Jaeger (1959) to obtain the following expression:

$$\frac{T(z,t) - T_i}{T_g - T_i} = \operatorname{erfc}\left(\frac{z}{2\sqrt{\alpha t}}\right) - \mathrm{e}^{\left(\frac{hz}{k} + \alpha t \frac{h^2}{k^2}\right)} \operatorname{erfc}\left(\frac{z}{2\sqrt{\alpha t}} + \frac{h}{k}\sqrt{\alpha t}\right) \tag{4.9}$$

By inserting the calibrated liquid crystal temperature and the time required to reach the liquid crystal indication color (i.e. $T(z,t) = T_{LC}$, $t = t_{LC}$), and z the depth at which the TLCs are installed, the heat transfer coefficient h can be determined numerically. In practice, the step in the gas temperature is not instantaneous, and Duhamel's principle can be used to superpose a series of temperature steps that approximate the real gas temperature evolution (Terzis et al., 2012). Note that to achieve an acceptable accuracy, the temperature data acquired with the thermocouples needs to be post-processed to account for their thermal inertia as explained in Section 3.3.2.

For the heater foil method, the imposed surface heat flux $q(t)$ is equal to the heat transfer into the fluid by convection plus the heat conducted into the solid:

$$-k\frac{\partial T(0,t>0)}{\partial z} - h[T_{aw} - T(0,t)] = q(t) \tag{4.10}$$

where T_{aw} is the adiabatic wall temperature, which can be considered equal to the initial/ambient temperature T_i if the jet is at ambient condition. If not, T_{aw} must be determined considering the entrainment effect that mixes the jet at temperature T_g and the

surrounding air at temperature T_i. The entrainment effect is defined in analogy to the film cooling effectiveness:

$$\eta_e = \frac{T_{aw} - T_r}{T_g - T_i} \tag{4.11}$$

where T_r is the recovery temperature, which is defined as the adiabatic wall temperature T_{aw} when the jet total temperature is equal to the ambient temperature. In the present work, the recovery temperature T_r is assumed to be equal to the ambient temperature T_i, similarly to Baughn et al. (1991); the potential error of this simplification is negligible due to the low jet Mach number ($M_{max} \approx 0.1$).

In Eq. 4.10, $q(t)$ is the time evolution of the surface heat flux; the technique developed for this study uses a linearly increasing surface heat flux: $q(t) = q_0 t$. In this case, the solution of Eq. 4.3 reads:

$$\begin{aligned} T(z,t) = T_i + \eta_e (T_g - T_i) \left[\mathrm{erfc}(a) - \mathrm{e}^b \mathrm{erfc}(a+c) \right] \\ + \frac{q_0}{k\alpha^2} \left[\frac{\alpha}{(-\frac{h}{k})^3} \mathrm{e}^b \mathrm{erfc}(a+c) - \frac{\alpha}{(-\frac{h}{k})^3} \sum_{r=0}^{2} (-2c)^r \, i^r \mathrm{erfc}(a) \right] \end{aligned} \tag{4.12}$$

where $a = \frac{z}{2\sqrt{\alpha t}}$, $b = \frac{hz}{k} + \alpha t \frac{h^2}{k^2}$, and $c = \frac{h}{k}\sqrt{\alpha t}$ are introduced to simplify the expression. Additionally, the term $i^r \mathrm{erfc}(a)$ denotes the r$^{\text{th}}$ successive integration of the complementary error function, which can be defined iteratively as follows (see Appendix 2 in Carslaw and Jaeger, 1959):

$$i^n \mathrm{erfc}(x) = \int_x^\infty i^{n-1} \mathrm{erfc}(\xi) \, d\xi \tag{4.13}$$

$$i^0 \mathrm{erfc}(x) = \mathrm{erfc}(x) \tag{4.14}$$

Detailed resolution steps are reported in Appendix A.

Equation 4.12 is used for the validation of the experimental technique, since the wind tunnel used (see Section 3.4) has fans upstream of the test section, whose motor increases the flow temperature above the ambient temperature. The actual tests on the sequential impingement are setup in suction mode, so that T_g=T_i. In this case, Eq. 4.12 reduces to:

$$T(z,t) = T_i + \frac{q_0}{k\alpha^2} \left[\frac{\alpha}{(-\frac{h}{k})^3} \mathrm{e}^b \mathrm{erfc}(a+c) - \frac{\alpha}{(-\frac{h}{k})^3} \sum_{r=0}^{2} (-2c)^r \, i^r \mathrm{erfc}(a) \right] \tag{4.15}$$

In principle, any arbitrary function can be used for the heat flux term $q(t)$ in Eq. 4.10, provided that the heat conduction equation can be solved analytically with such a boundary condition. The choice of a linearly varying heat flux is justified by the almost linear relationship achieved between the measured variable (the time to reach the TLC indication temperature) and the variable of interest which is computed via the heat conduction

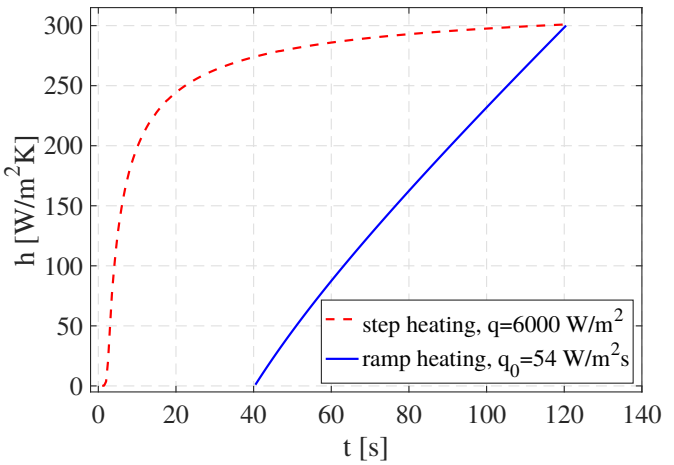

Figure 4.2 – Relationship between the heat transfer coefficient and the liquid crystal indication time for a constant heat flux experiment (step heating method from Gaffuri et al., 2018, dashed line), and the linearly increasing heat flux (ramp method, solid line).

equation (the heat transfer coefficient). Figure 4.2 shows the h-t relationship when using a linearly increasing heat flux (obtained using Eq. 4.15) and a constant heat flux, for which an analytical solution is also available. The heat flux is set in such a way that a heat transfer coefficient h=300 $W/(m^2K)$ can be measured in t=120 s. With a linearly increasing heat flux two issues present in the step heating case are avoided:

- The initial gradient is very steep, so that a small error in the time measurement leads to a big error in the evaluation of the heat transfer coefficient. With a ramp heating, the gradient is nearly constant.
- The h-t curve has an asymptotic shape; h values higher than the asymptote cannot be determined (the TLCs never reach the indication color), unless the experiment is setup with a higher heat flux, but this further reduces the accuracy in the low heat transfer region. With ramp heating, one can simply increase the experiment time, within the limits of the semi-infinite assumption.

4.3 TLC calibration

A device for the calibration of the liquid crystals, inspired by work in Poser and von Wolfersdorf (2010) and Waidmann et al. (2013), has been developed in the frame of this study. It consists in an insulated copper bar (see Fig. 4.3) whose ends are held at constant temperature by water recirculating from 2 thermostatic baths, so that a temperature gradient is achieved through the bar's length. Ten calibrated type-K thermocouples, installed below the surface, allow to determine the temperature along the bar; the thermocouples can be recalibrated simply by inserting the copper bar in a thermostatic bath togheter with a precision platinum resistance thermometer and varying the liquid temperature in steps.

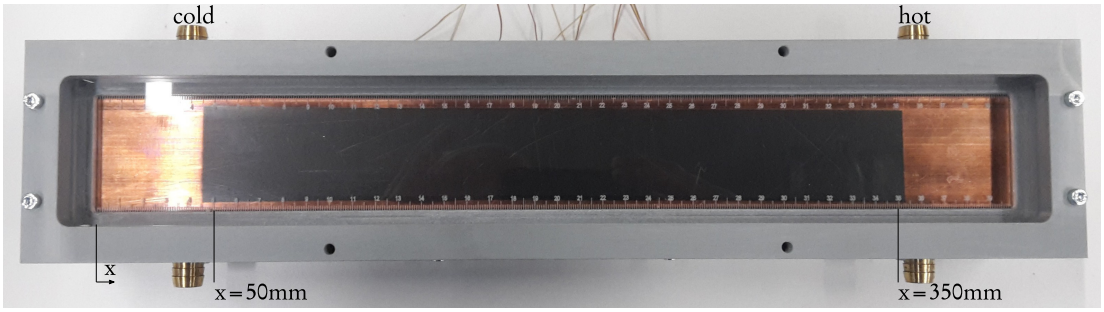

Figure 4.3 – TLC calibration device.

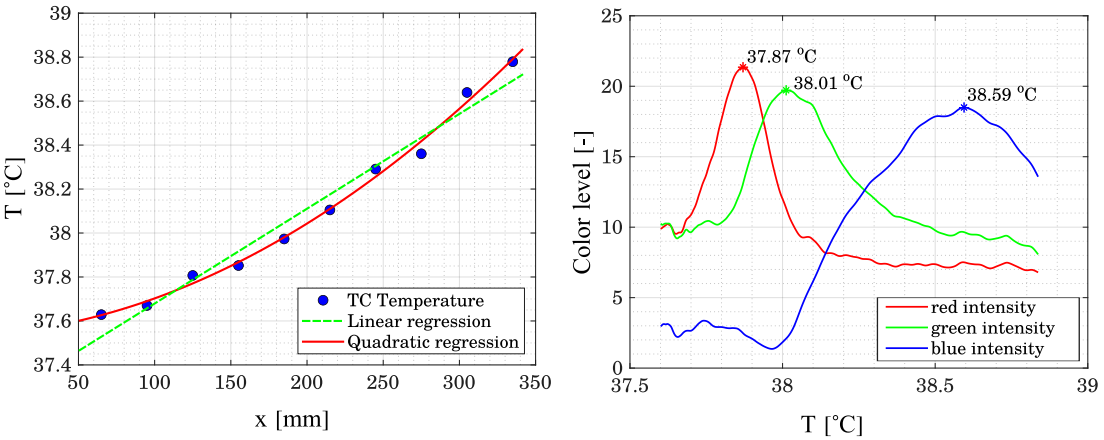

(a) **(b)**

Figure 4.4 – Example of a TLC calibration. **(a)** Thermocouple temperature data with a linear and quadratic fitting. **(b)** RGB calibration.

One side of the bar is painted with black paint and TLCs, so that a relationship between temperature and color hue of the liquid crystals can be established.

Figure 4.4 shows an example of a calibration for TLCs with a nominal temperature of 38°C and a bandwidth of 1 degree. In Fig. 4.4 (a), temperature data acquired using the thermocouples along the copper bar are shown. Ideally, the temperature distribution in a perfectly insulated bar would be linear; this is not the case, and to retrieve the temperature value at the location of the TLC maximum green intensity (which may lay in between TC locations) a quadratic interpolation is performed.

Calibration results are very similar to the results obtained with the method used previously in the laboratory (see Terzis et al., 2016a), which consisted in heating a TLC coated copper block in a water bath and taking images at small temperature intervals. The new device enables significant time savings, since only one measurement is needed.

4.4 Validation of the experimental technique

4.4.1 Single impingement tests

The newly developed experimental technique has been applied to a single impingement case using the setup shown in Fig. 3.4, with variations of the jet-to-plate distances Z/D from 4 to 10 and Reynolds numbers, based on the jet diameter, from 20,000 to 40,000. The data reduction consists in the determination of the Nusselt number as a function of the radial position from the stagnation point; for this, pixels at a common distance r/D from the stagnation point are averaged. To validate the experimental implementation, results were compared with the correlation of Goldstein and Franchett (1988) which is based on experiments for a similar jet hole geometry.

Reynolds variation

Figure 4.5 (a) shows results for the case Z/D=6 obtained with a rate of increase of the heat flux (q_0) equal to 50 $W/(m^2 s)$. The results are in very good agreement with the correlation. Only close to the stagnation point a discrepancy can be observed. This can be attributed to the lateral conduction in the foil, which is expected to be maximal at the stagnation point, and to the chamfer of the jet hole, which can have an impact on the jet velocity profile which in turn can affect the development of the jet shear layer. The Reynolds number scaling of the heat transfer is found to be consistent with the correlation, which assumes that Nu scales with $Re^{0.7}$; the curves for the three Reynolds numbers investigated are superposed in the graph of Fig. 4.5 (a), which shows Nusselt number normalized by $Re^{0.7}$.

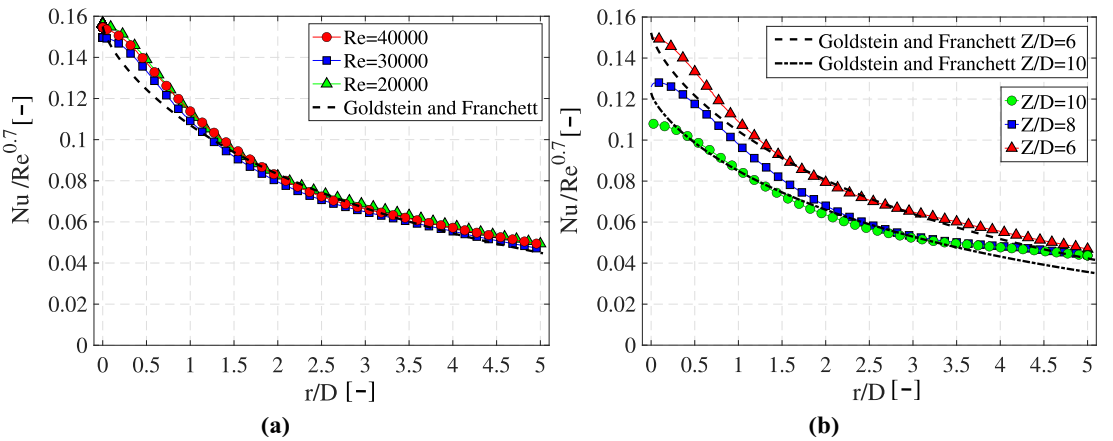

Figure 4.5 – Normalized Nusselt number as a function of the radial distance for Z/D=6 for varying (a) Reynolds numbers and (b) jet to plate distances and comparison with the correlation of Goldstein and Franchett (1988). A ramp slope q_0 of 50 $W/(m^2 s)$ has been used.

Jet-to-plate distance variation

In Fig. 4.5 (b), results at three jet-to-plate distances are shown for Re=30,000 and q_0=50 $W/(m^2s)$. For two of the configurations, namely Z/D=6 and Z/D=10, results are compared with the correlation used as reference. For the case Z/D=8, however, the correlation is not available, since the scaling parameter (A, in Goldstein and Franchett (1988)) is only defined at certain distances.

Results at Z/D=10 are in good agreement with the correlation; similar to the Z/D=6 case, the stagnation point heat transfer is slightly lower than the correlation. For the case Z/D=8, the heat transfer level at the stagnation point is between the other two cases, as expected. At higher radial distances, however, results are shifted to similar levels as the case Z/D=10. Note that for radial distances r/D greater than 3.5, the entrainment effect correlation used (Goldstein et al., 1990) does not depend on the jet to plate distance Z/D, which can lead to increased uncertainty in the adiabatic wall temperature determination. Also the pixel averaging of the results for common r/D distances is based on fewer points with increasing r/D, due to the rectangular geometry of the area which is examined (Fig. 3.4). At higher radial distances, all cases show similar heat transfer, which could be expected in the wall jet region, and is in agreement with the literature (Baughn and Shimizu, 1989).

The correlation used as reference is defined only for jet to plate distances Z/D equal to 4, 6, and 10. Using the data obtained through these experiments, an extension to arbitrary Z/D in the range [4 10] has been proposed (see Appendix B).

Influence of the ramp slope

The advantage of the linearly varying heat flux method over the constant heat flux is the freedom in choosing the heat flux value, or more accurately, the rate of increase of the heat flux, provided that the total experiment time is consistent with the semi-infinite condition assumed in the solution of the heat conduction equation.

In Fig. 4.6, results for the case Z/D=6 at Re=30,000 with three different heat flux slopes are presented: 50 $W/(m^2s)$ (ramp 1), 75 $W/(m^2s)$ (ramp 2), and 150 $W/(m^2s)$ (ramp 3). Results are independent of the ramp slope chosen. While this is obviously expected, it confirms the consistency of the method.

In the same figure, the result accuracy is plotted (see Section 4.4.1 for the approach used for the determination of the uncertainty, as well as for the uncertainty sources); the accuracy of the method increases when reducing the rate of increase of the heat flux, especially in the wall jet region, where the 2σ error can be reduced from 13.5% to 10%. A further reduction of the heat flux slope, however, does not improve much in terms of accuracy, as can be inferred from the similar accuracy of ramp 2 and ramp 3.

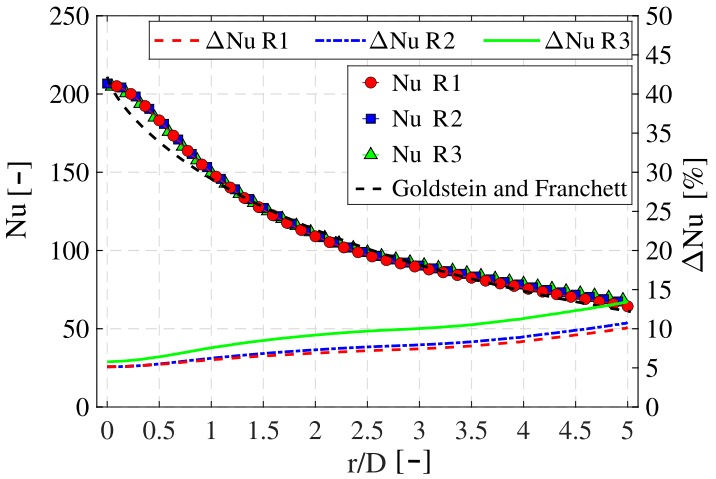

Figure 4.6 – Nusselt number values for the case Z/D=6 and Re=30,000 with 3 different rates of increase of the surface heat flux, and 2σ accuracy expressed as a percentage of the local Nu_D (right axis).

Thermal inertia of the foil and lateral conduction

To estimate the thermal inertia of the foil and its effect on the results, the experimental data are post-processed as follows: a) the temperature evolution of the surface during the experiment is computed using Eq. 4.12 with the experimentally determined h value; b) the time evolution of the heat flux absorbed by the foil during the experiment is computed using the equation

$$q_{ti} = \rho_s c \frac{\partial T}{\partial t} \delta \tag{4.16}$$

where δ is the thickness of the foil and c is the specific heat capacity of the foil material c) q_{ti} can be expressed as a percentage of the applied heat flux. In this case, we consider the jet temperature to be equal to the ambient temperature T_i, to better evaluate the method itself.

Fig. 4.7 (a) shows the heat flux absorbed by the foil during the experiment, expressed as a function of the instantaneous applied heat flux, for a point in the wall jet region (r/D=5). This is the location where the thermal inertia shows the biggest influence on the results, since the temperature increases the fastest.

The thermal energy absorbed by the foil is high, relative to the applied heat flux, for the first few seconds of the experiment. This is due to the fact that the applied heat flux is low at the beginning of the experiment, since it is linearly increased from 0. The absorbed heat then quickly drops below 1% of the applied heat flux. Interestingly, the absorbed heat relative to the applied heat does not depend on the ramp slope; this can be deduced by the superposed lines in Fig. 4.7 (a). Subtracting the thermal inertia to the applied heat flux gives an insight into the effect that the thermal inertia has on the results. A linear fit of the modified heat flux has a very similar slope as the applied heat flux but with an intercept at -25 W/m^2 instead of 0. This is analogous to a shift in the time of the start

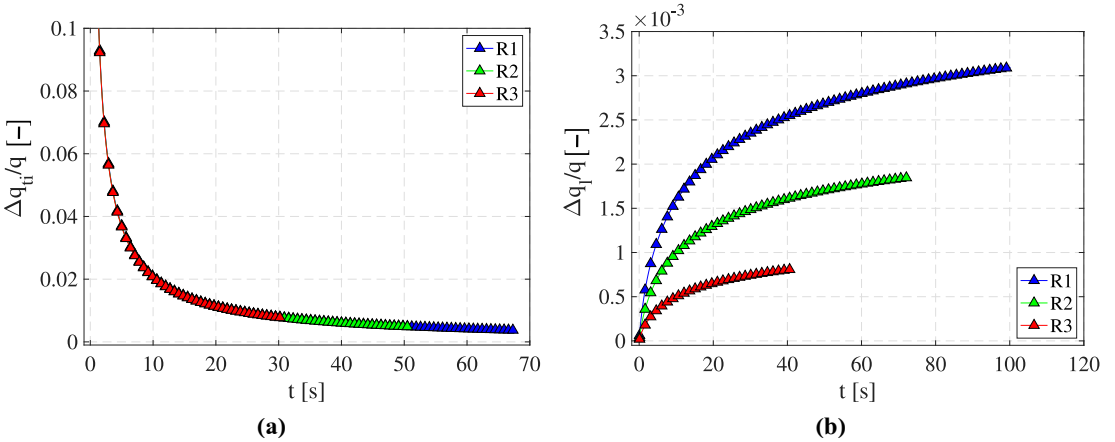

Figure 4.7 – (a) Time evolution of the thermal inertia of the foil, relative to the applied heat flux, for the position r/D=5 at Z/D=6 and Re=30,000. Ramp 1, 2, 3 have a slope of 50, 75, and 150 $W/(m^2 s)$, respectively. (b) Time evolution of the lateral conduction, relative to the applied heat flux, at the stagnation point for the case Z/D=6 and Re=30,000, for the 3 heat flux ramps.

of the experiment of $25/q_0$ seconds. As discussed in Section 4.4.1, the error due to the uncertainty of the time value is very small, which means that the effect of thermal inertia can be neglected.

Due to the much higher thermal diffusivity of the metal foil compared to the PMMA material, the evaluation of the lateral conduction is mainly relevant for the foil. The evaluation is performed by post-processing the experimental data: after finding the temperature evolution at each radial location as a function of time using Eq. 4.12, the second derivative of the temperature as a function of the radial coordinate can be obtained numerically. A pre-smoothing of the heat transfer coefficient might be necessary to reduce the noise of $\partial^2 T/\partial r^2$. Finally, the lateral conduction can be computed with the following formula:

$$q_l = k\frac{\partial^2 T}{\partial r^2}\delta \tag{4.17}$$

In Fig. 4.7 (b), the ratio of the lateral conduction to the applied heat flux is shown as a function of time for the case Z/D=6 at the stagnation point, which is where lateral conduction is expected to be maximal. The lateral conduction in the foil is maximal at the end of the experiment for the slow ramp case, and its value is approximately 0.3% of the applied heat flux. This value is small enough for the lateral conduction to be neglected.

Experimental uncertainties

The experimental uncertainties are calculated based on the method of small perturbations, which uses the root sum square technique to combine single uncertainty terms of the

	Error	High-h 350 $W/(m^2K)$	Low-h 120 $W/(m^2K)$
T_i	$\pm 0.1K$	0.06%	0.20%
T_g	$\pm 0.1K$	0.10%	0.01%
T_{LC}	$\pm 0.1K$	0.30%	0.13%
q_0	$\pm 0.5W/(m^2s)$	1.15%	1.61%
η	$\pm 4.3\%$	3.02%	0.16%
α	$\pm 7.5\%$	0.42%	1.63%
k	$\pm 7.5\%$	1.00%	5.04%
z	$\pm 10^{-5}m$	0.08%	0.09%
t_{LC}	$\pm 0.0667s$	0.01%	0.01%
Δh		6.14%	8.88%

Table 4.1 – Detailed uncertainties for Re=30,000, Z/D=6.

measured parameters to estimate the overall uncertainty of the heat transfer coefficient (Kline, 1953; Moffat, 1988).

$$\Delta h = \sqrt{\sum_{i=0}^{n} \left(\frac{\partial h}{\partial x_i} \right)^2 \Delta x_i^2} \tag{4.18}$$

Assuming that the uncertainty of each parameter is statistically independent and normally distributed, the error can be calculated using Eq. (4.18), in which a 2σ (95%) confidence interval is considered.

Table 4.1 shows the calculated individual components contributing to the overall uncertainty of the heat transfer coefficient at Z/D=6 and Re=30,000 for a heat flux slope of 50 $W/(m^2s)$. The error at the stagnation point is 6%, and 9% in low heat transfer regions, which is similar to the state of the art for the heater mesh method (see Terzis et al., 2014a).

At the stagnation point, the overall uncertainty is dominated by the uncertainty on the entrainment correlation, by the ramp slope and by the thermal properties of the solid (thermal conductivity, thermal diffusivity). In the impingement array facility, which is operated in suction mode, both the jet flow and the solid are initially at ambient temperature; the entrainment correlation would not be required in this case, and the uncertainty at the stagnation would be reduced by half in the high heat transfer region. In the low heat transfer regions, the uncertainty is mainly due to the thermal properties, and to a minor extent to the ramp slope. The results show good repeatability, with variations of the results always below 2%.

4.4.2 Impingement array

Since several components of the experimental setup have been changed after a former project – most notably the laminar flow element and the vacuum pump – a validation of

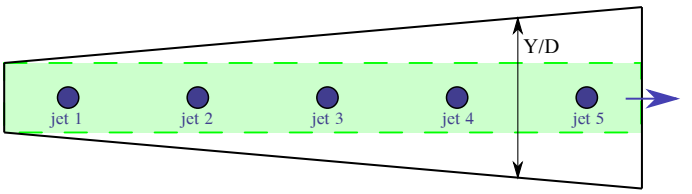

Figure 4.8 – Schematics of the divergent impingement channel used for the validation of the experimental facility. The green rectangle shows the area used for the comparison of the heat transfer coefficients in Fig. 4.9. The channel width Y increases from $3D$ to $6.67D$.

the setup itself was needed. Moreover, the test facility has been moved to a different building, and consequently a check of the instrumentation was required.

For this validation, a divergent impingement array, whose test results were reported by Terzis et al. (2016b), was chosen. This study was performed by applying the most up to date experimental procedure using the heater mesh technique; this includes:

- multiple layers of liquid crystals,
- correction for the thermocouple thermal inertia,
- Duhamel's superposition principle to account for the measured temperature evolution.

The geometry has a jet-to-plate spacing Z/D=2 and a width Y/D that varies linearily from 3 at the upstream wall to 7 at the channel exit; the streamwise spacing of the jets is X/D=$6.\bar{6}$ (see Fig. 4.8). Tests were carried out using the same experimental procedure, namely the heater mesh method (see also Eq. 4.9), with a double layer of TLCs. The target plate thickness is 20 mm.

Figure 4.9 shows the spanwise-averaged Nusselt number, normalized by $Re^{0.7}$ and $Pr^{1/3}$, for the central strip of the channel of width 3D, for the validation tests (colored lines) and for the reference data from Terzis et al. (2016b), shown as black lines, at various Reynolds numbers. Good agreement is found in terms of heat transfer, with the new results slightly lower than the reference data. This can be attributed to a more accurate (and precise) Reynolds number derivation, since the new LFE is more adapted to the actual massflows used and freshly calibrated. It is to be noted that the experimental uncertainties of the heater mesh method are in the range of 10%, in line with the state of the art for this technique, so that the two sets of data are within this confidence interval.

For the pressure measurements, the validation is performed on a rectangular channel with 5 jets and dimensions X/D=5, Y/D=5, and Z/D=3. The pressure drop is expressed in terms of discharge coefficient, which essentially is a ratio of the massflow to the theoretical massflow of a fluid expanding isentropically between the same pressures through a nozzle

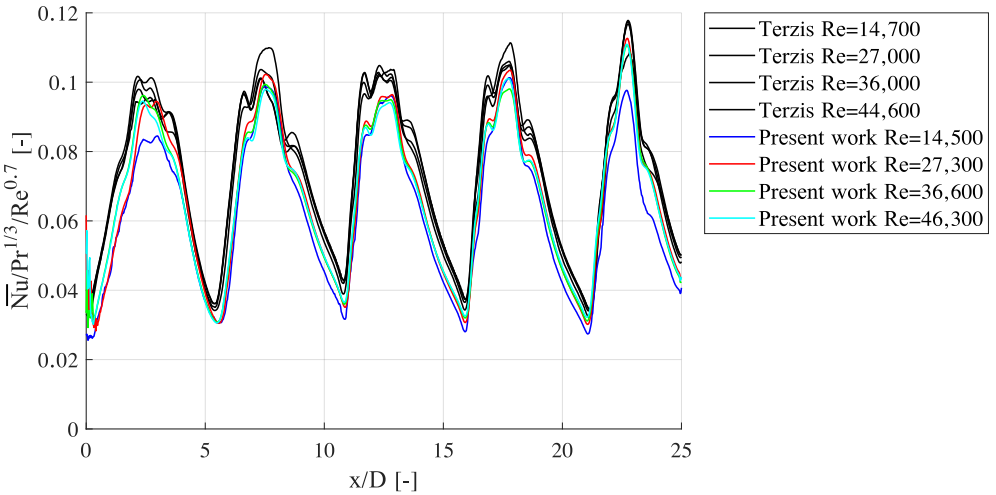

Figure 4.9 – Comparison of the normalized, spanwise-averaged Nusselt number along the channel for the divergent impingement channel with previous data (Terzis et al., 2016b) on the same geometry. Only the inner rectangular part of the channel is considered for the averaging.

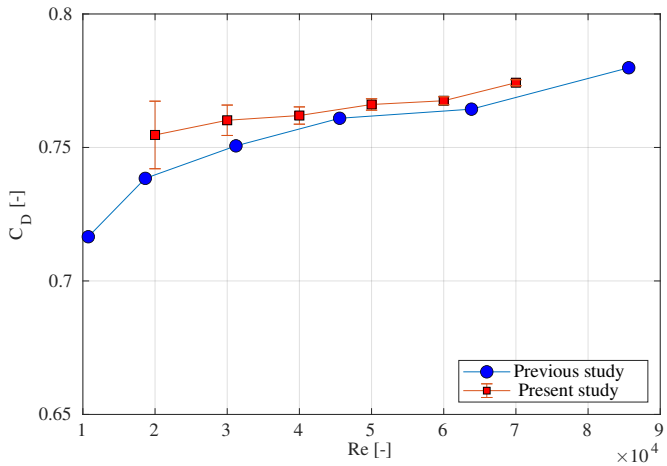

Figure 4.10 – Discharge coefficient of a 5 jets, single row impingement channel with dimensions X/D=5, Y/D=5, and Z/D=3, measured with the current setup and comparison with previous data for the same geometry (Terzis, 2014).

with the same throat area. With a known massflow $\dot{m}$, jet hole area A, and pressure drop Δp, the discharge coefficient C_D can be computed as follows:

$$C_D = \frac{\dot{m}}{A\sqrt{2\rho\Delta p}} \tag{4.19}$$

in which ρ is the fluid density determined via the temperature and pressure data assuming a perfect gas.

For the validation, the measured data are compared to data obtained in a previous project on the same geometry and published in Terzis (2014). Slightly higher discharge coefficients (lower losses) are found with the new setup. Again, this hints at a difference in

the massflow determination due to the new LFE. Nevertheless, the results are within the confidence interval of the measurements.

4.5 Conclusions

The improved measurement technique applied in this thesis has been presented. The newly developed experimental technique avoids several complications of the more common transient heater mesh technique, namely the need to correct the measured temperature to account for the thermocouples thermal inertia and the determination of the reference flow temperature for the convection. This technique could prove useful in the heat transfer community for cases that are complex from a fluid dynamics point of view (e.g. cases in which the flow can take different paths leading to mixing flows at different temperatures), provided that the metallic foil can be attached to the surface under study. The application of thin films via vapor metal deposition (Hippensteele et al., 1983; Mayhew et al., 2003) could make this technique more accessible also for more complex geometries.

The new technique is validated by comparing the results on a single impingement heat transfer problem to correlations from the literature. Results show excellent agreement and an uncertainty which is similar to (or lower than) the heater mesh technique.

Chapter 5

Experimental results

This chapter presents the results obtained during the experiments on the multi-impingement test rig. First, the results on the baseline geometry are analyzed in detail, also by comparing to literature data and correlations for impingement jets. A parametric analysis for the number of jets and the length of the transition zone follows in Section 5.2. The analysis then focuses on the heat transfer enhancement devices installed in the transition zone, and in particular on the impact of their addition on both the heat transfer and the pressure drop. The main findings are presented in this chapter, while a comprehensive assessment of the performances of the sequential channels is available in Chapter 6. Some of the results have been presented at the European Turbomachinery Conference (Gaffuri et al., 2021a) and at the ASME Turbo Expo (Gaffuri et al., 2021b). They are reported here in an expanded form with more details along with other geometries like pins and combinations of heat transfer enhancement devices.

5.1 Baseline geometry

The baseline geometry has 2 channels, each with a single row of 5 jets, with a jet-to-jet spacing X=5D, and a transition zone of length 10D in the first channel. The rectangular channel cross-section has a width Y=5D and a height (jet-to-plate spacing) Z=3D. All tests are performed on one channel at a time, with a cooling phase of approximately 40 minutes to bring the channel walls back to a uniform temperature equal to the ambient. This is done to avoid a changing flow temperature in the second channel due to the heat pickup in the first channel. The analysis focuses on two aspects of the results: the heat transfer coefficient on the target plates, expressed as Nusselt number, in which the jet diameter D is used as reference length, and the pressure losses of each component of the geometry, which can be expressed as a discharge coefficient C_D. All tests are conducted at 3 Reynolds numbers (10,000, 20,000, and 40,000) similar to those encountered in a real gas turbine cooling system.

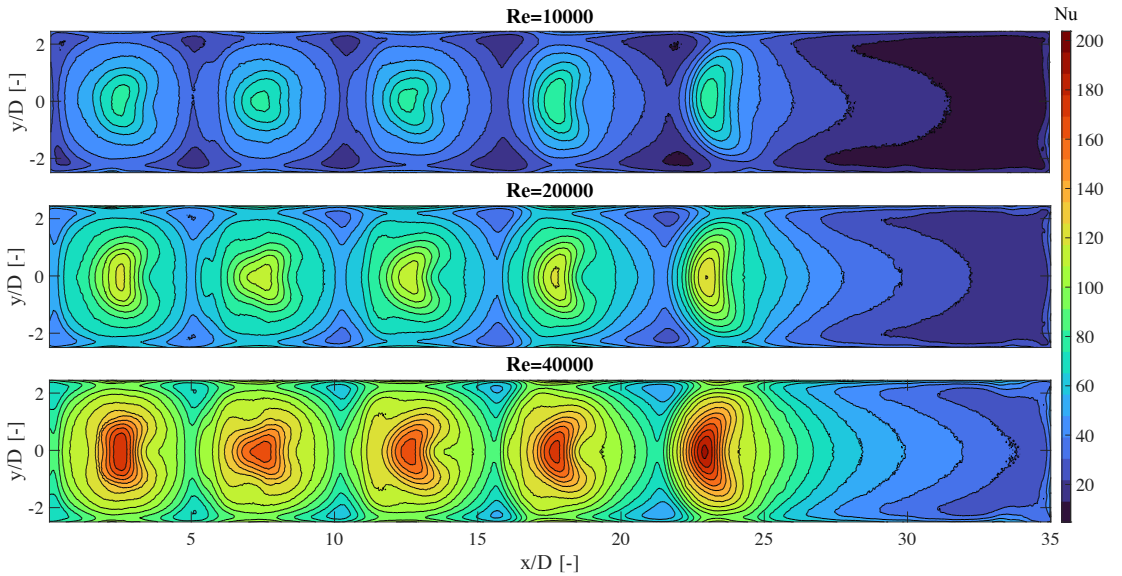

Figure 5.1 – *Nu* distribution on the target plate of the 1st channel of the baseline geometry for 3 Reynolds numbers. Crossflow from left to right.

5.1.1 Heat transfer distribution

The Nusselt number distribution at the 3 Reynolds numbers investigated for the first and second channel is presented in Figure 5.1 and 5.2, respectively, and gives a qualitative view of the results. As expected, the overall heat transfer levels are similar in both channels. One has to keep in mind that in a real case scenario, however, the cooling air temperature in the second channel would be higher than in the first due to the heat transfer in the first channel, leading to a reduction of the cooling capacity of the flow in the second channel. This is not reflected in the test results, since the reference temperature for the heat transfer coefficient determination is based on the jet temperature in the respective channel. The maximum heat transfer at the stagnation zone increases steadily until the 5th jet, with the exception of the 1st jet, which shows higher heat transfer than the 2nd. At high *Re*, the heat transfer levels of the upstream jets in the first channel show a flattened shape; this can be attributed to flow unsteadiness in the plenum for high jet Reynolds numbers.

In the downstream part of the 1st channel ($x > 25D$), the transition zone experiences low levels of heat transfer, with a minimum of approximately 10% of the jet stagnation value; in a real case scenario this can create issues with the thermal stresses associated with the large temperature gradients arising in the material of the part to be cooled. This is a critical zone and for this reason it is one the focal points of the present study.

In the second channel (Fig. 5.2) the heat transfer patterns around the stagnation points are more regular. Unlike in the first channel, the stagnation point Nusselt number increases from the 1st to the 4th jet, where it is maximum, then starts to decrease. This is due to the different flow in the second plenum compared to the first: the discharge flow

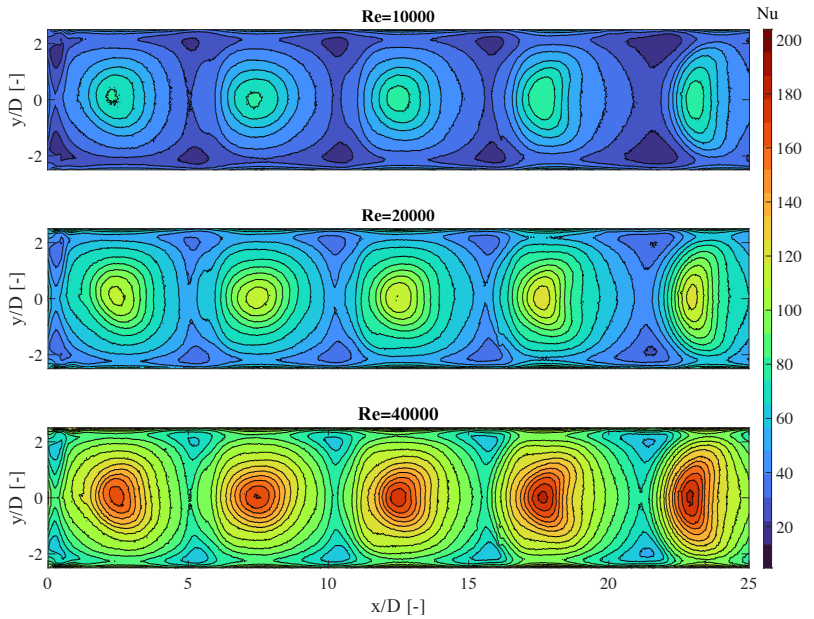

Figure 5.2 – *Nu* distribution on the target plate of the 2nd channel of the baseline geometry for 3 Reynolds numbers. Crossflow from left to right.

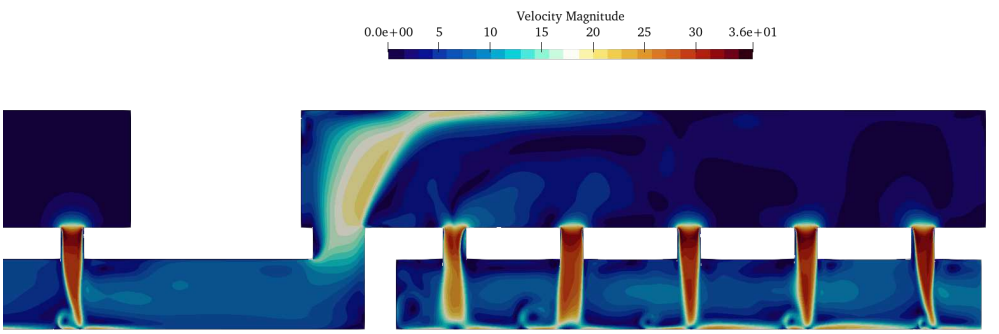

Figure 5.3 – CFD results showing the velocity magnitude in the channel center plane for the baseline geometry at *Re*=20,000. The upstream part of the 1st channel is omitted.

from the transition zone enters the second plenum via the purge hole; its relatively small area, 2 times the open area of the first channel, results in a mean flow velocity of the discharge equal to half the mean impingement jet velocity. This causes a jet-like flow into the second plenum, which impinges on the surface opposite the jet plate, resulting in a complex recirculating flow in the second plenum. The effect of this is a flow detachment at the inlet of the 1st jet that reduces its massflow. This is illustrated in Fig. 5.3, which presents computational fluid dynamics (CFD) results of a simulation solving the Reynolds-averaged Navier-Stokes (RANS) equations using a k-ω turbulence model. Details of this setup are available in Appendix C.

Figure 5.4 presents the same *Nu* data as a spanwise-averaged value along the channel, which allows for a more quantitative assessment of the results. Here, both channels are on the same graph to allow for a more direct comparison. The same observation about

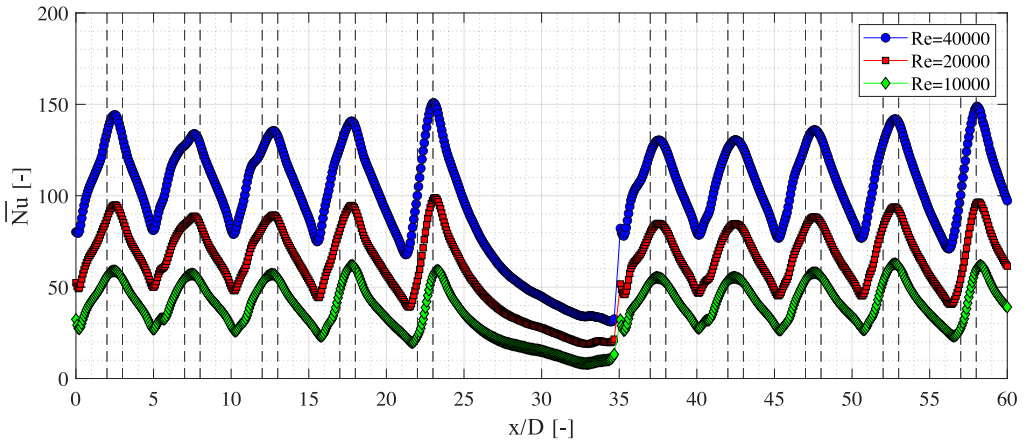

Figure 5.4 – Spanwise-averaged Nu on the target plate of the baseline geometry for 3 Reynolds numbers. The dashed vertical lines show the jet hole locations.

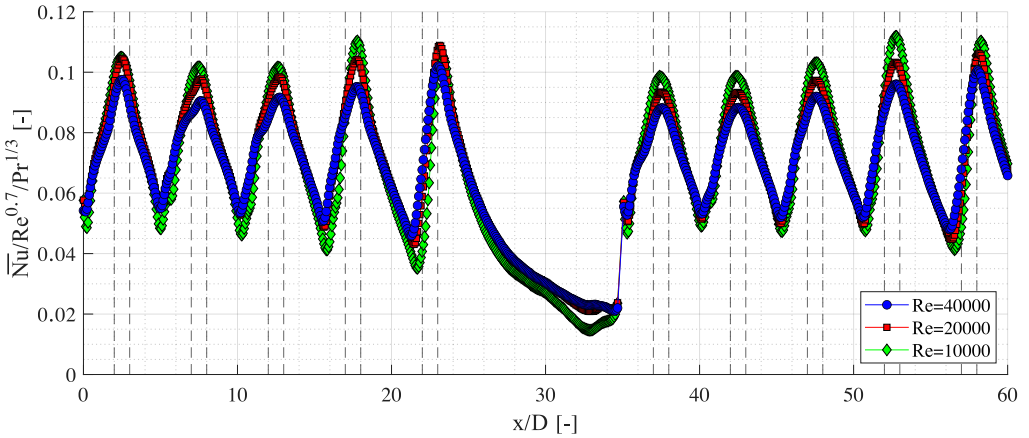

Figure 5.5 – Spanwise-averaged Nu divided by $Re^{0.7}$ and $Pr^{1/3}$ on the target plate of the baseline geometry for 3 Reynolds numbers. The dashed vertical lines show the jet hole locations.

the evolution of the stagnation heat transfer can be made. However, in the 2nd channel, the maximum peak when considering the complete width of the channel occurs at the last jet; this is due to the fact that the crossflow changes the shape of the Nu pattern on the plate. The more "flattened" pattern shows higher heat transfer near the sidewalls. The dashed lines in Fig. 5.4 indicate the locations of the jet holes. With this reference it can be noted how the crossflow shifts the stagnation point of the downstream jets (especially the last one of each channel, which is convected downstream more than half jet diameter). This is supposed to be the cause of the reduction of the Nu values in the wall jet region (the valleys in the graphs of Fig. 5.4) when moving downstream.

It is common to scale data with the Reynolds number of the experiment and the Prandtl number of the cooling fluid, both raised to a specific exponent, as noted in Section 2.2.2. In this way, the obtained data may be used directly for the design even if the gas conditions – thermal conductivity, viscosity, specific heat – and the size of the channel differ from the test conditions. In the following, Nu will be scaled with $Re^{0.7}$, which was shown to

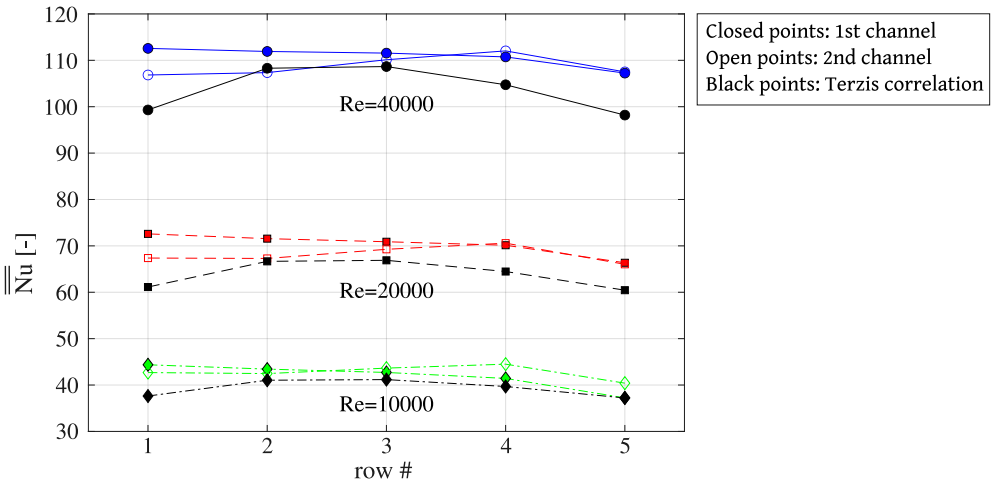

Figure 5.6 – Row-by-row averaged Nu for the baseline geometry and comparison with Terzis correlation (Terzis et al., 2014a).

be an appropriate scaling factor for narrow impingement channels (Terzis et al., 2014a) at fully turbulent Reynolds numbers. The Prandtl number will be assumed to be $Pr^{1/3}$, as is common in the literature.

Figure 5.5 presents the spanwise-averaged data scaled in this way. The Re^m scaling seems appropriate, since the different curves are on top of each other. In the stagnation zone (peaks), the normalized Nu decreases with increasing Re; this means that the proper scaling would be with a lower exponent m, and can be explained by the fact that the wall jet flow originating at the stagnation point is initially laminar. This flow quickly transitions, and at these Reynolds numbers is fully turbulent when it reaches the zones corresponding to the valleys of the curves in Fig. 5.5. For a fully turbulent flow, it is assumed that Nu scales with $Re^{0.8}$ (see for instance the Nu correlations for a turbulent flow over a flat plate, e.g. Incropera et al., 2006), and this is the reason why the low Reynolds numbers, particularly at Re=10,000, show lower minima at this location.

To assess the contribution of each jet in the channel, results can be area-averaged for each jet location. This is presented in Fig. 5.6 for both channels at the 3 Re investigated. For the 1st channel, the transition zone is omitted. Results compare well with Terzis correlation (Terzis et al., 2014a), which has been developed for narrow impingement channels. Globally, the results are slightly higher than the correlation, but within the experimental uncertainty; the Nu reduction in the last rows is qualitatively similar. However, the 1st channel, whose flow should be topologically similar to a single impingement channel, shows the same average Nu for the 4 upstream rows, and does not show the heat transfer reduction at the 1st jet predicted by the correlation; one reason to explain this could be the fact that the discharge coefficient of the jet is higher (see next Section), so that the massflow discrepancy between the jets is reduced. In the second channel, the average Nu increases steadily up to the 4th jet, where it reaches the maximum value; as noted above, the reason for this is the flow topology in the second channel (see Fig. 5.3).

5.1.2 Pressure drop

To evaluate the pressure drop of the sequential configurations, pressure taps are installed in the plenum and at the outlet; for both, taps are installed at different locations of the perimeter and the pneumatic lines are connected together in order to measure an average value of the pressure. Additionally, taps are installed on the channel itself, at the beginning of the transition zone and in the 2nd plenum, to be able to assess the contribution on the pressure losses of each component of the channel. At the beginning of the transition zone, 2 taps are installed at 1/3 and 2/3 of the channel height on one side of the channel, and their values are averaged. In the second plenum, 5 taps are placed in the chordwise direction on one side and pneumatically averaged to get a single value for the plenum pressure. Note that the pressure values are measured for a higher range of Reynolds numbers: from 10,000 to 50,000 with an interval of 5000. For some configurations, however, a massflow corresponding to a Reynolds number of 50,000 cannot be reached due to higher pressure losses and/or a higher number of jets per channel. In this case the Reynolds number is limited to 40,000 or 45,000 for the pressure loss measurements.

Figure 5.7(a) reports the pressure losses as a function of *Re*; the biggest contributor to the losses is the flow through the impingement holes, with the losses in the 2nd channel slightly higher than in the 1st. The flow through the purge hole, defined as the pressure difference between the beginning of the transition zone and the second plenum, accounts for only a small part of the losses, thanks to the higher passage area, the purge hole having a surface equal to 2 times the total jet hole area of the first channel.

In order to give more information on the performances of the channel, Fig. 5.7 shows the same data expressed as a discharge coefficient, which is the ratio between the measured massflow and the massflow of a perfect nozzle with the same throat area, isentropically

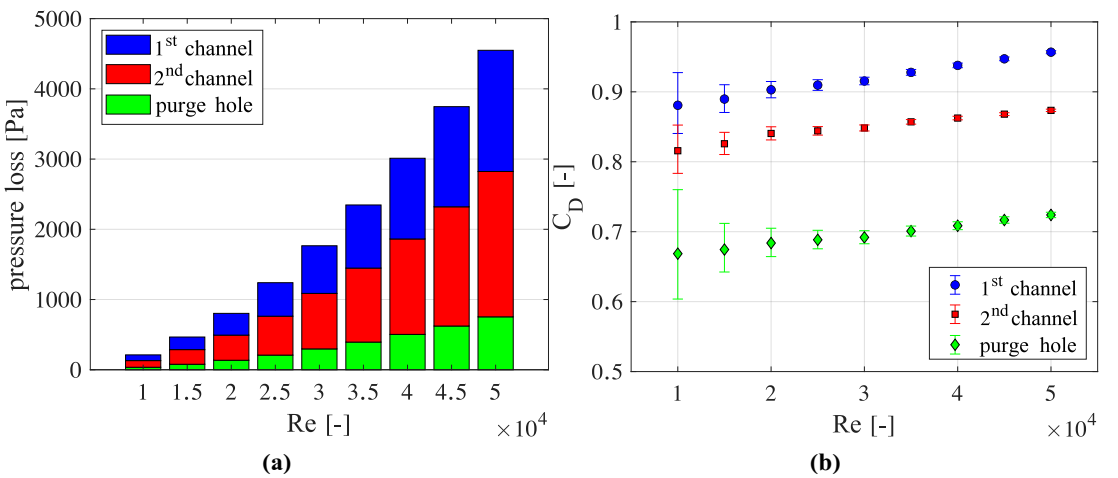

Figure 5.7 – (a) Pressure losses of the baseline channel as a function of *Re*, with breakdown of the main components: impinging flow in the 1st channel, in the 2nd channel, and discharge through the purge hole. (b) Discharge coefficient of each component as a function of *Re*.

expanding a flow between the same pressures. In short, an isentropic expansion would have a discharge factor C_D of 1. The discharge coefficient can be computed as follows:

$$C_D = \frac{\dot{m}}{A\sqrt{2\rho\Delta p}} \tag{5.1}$$

in which A is the area of the component considered, i.e. the total jet hole area for the impingement losses and the purge hole area for the purge hole losses. The discharge coefficient of the impingement jets is higher than that measured on the single impingement channel (see Fig. 4.10 for the discharge coefficient found during the validation of the setup); this is due to the fact that the jet holes are chamfered, thus reducing the losses. This is confirmed by the fact that the discharge of the single impingement jet facility (see Section 3.4), where the jet hole is also chamfered, has similar values. Additionally, tests on a narrow impingement channel with and without chamfered holes showed a similar impact of the chamfer on the discharge coefficient. Despite the small losses in absolute terms, the flow through the purge hole exhibits a relatively low discharge coefficient, due to the bigger surface area of the hole. Therefore, there is a margin of improvement in this part of the channel.

5.2 Geometric variations of the channel

A first batch of tests was run to assess the impact of various geometrical parameters to the overall heat transfer rate. These include the number of jets, the length of the transition zone, and the addition of bypass holes between the channels.

5.2.1 Transition zone length variation

Three different lengths of the transition zone have been investigated. In addition to the baseline geometry (L_{trans}=10D), a shorter (L_{trans}=5D) and a longer (L_{trans}=15D) version have been selected to assess the sensitivity of the Nusselt number, especially in the transition zone, to this parameter.

Figure 5.8 shows the Nu distribution for the 3 cases at Re=10,000 (other Reynolds numbers are qualitatively similar and are omitted here). It can be noted that the length of the transition zone has no effect on the impingement area heat transfer. With a short transition zone (L_{trans} = 5D), a secondary impingement of the wall jet flow to the endwall of the channel can be seen in the Nusselt number distribution. The long transition zone shows similar behavior as the baseline, with lower heat transfer on the sides of the channel. The Nusselt number reduction, along the transition zone, shows the same evolution, at least in the center line, as can be inferred by the superposed lines in the graph of Fig 5.9 (a). The second channel shows no effect of the variation of the transition zone length and is therefore not shown here; this implies that the discharge flow is similar for the 3 cases.

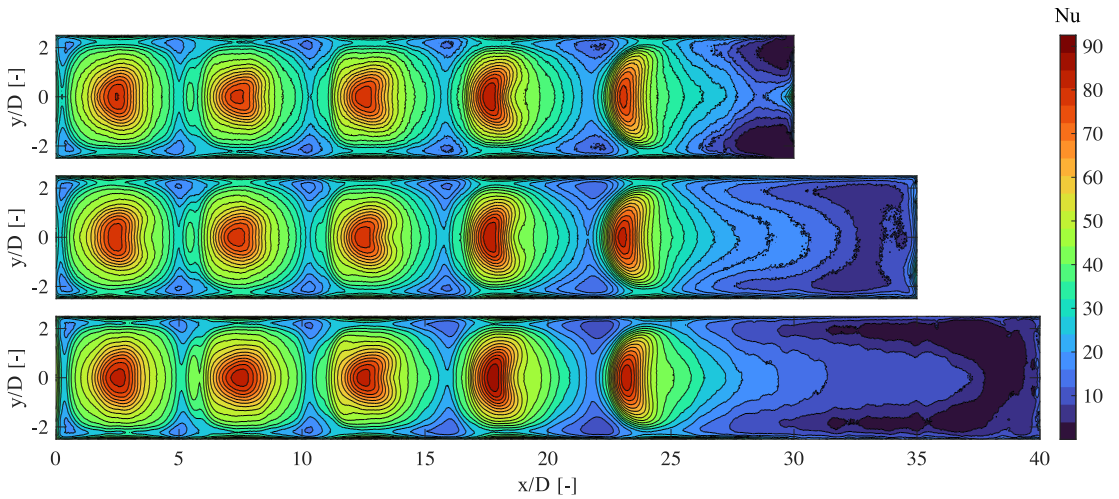

Figure 5.8 – Nu distribution on the target plate of the 1st channel for different lengths of the transition zone at Re=10,000. From top to bottom: L_{trans}=5D, L_{trans}=10D (baseline), and L_{trans}=15D.

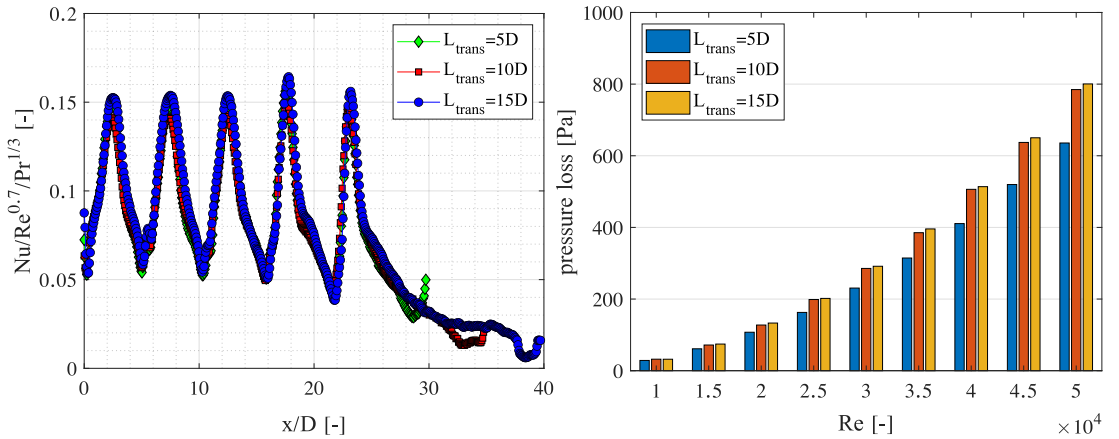

(a) **(b)**

Figure 5.9 – (a) Normalized Nu in the centerline of the 1st channel for different lengths of the transition zone at Re=10,000. (b) Pressure loss between the start of the transition zone and the second plenum, as a function of Re, for varying length of the transition zone.

Regarding the pressure losses, the length of the transition zone does not impact the discharge coefficient of the impingement flow. Figure 5.9 (b) shows the pressure difference between the beginning of the transition zone and the second plenum, which corresponds to the losses in the transition zone and in the purge hole.

The losses increase with increasing the transition length. This is expected, since a longer channel implies higher friction losses. Nevertheless, the difference between the baseline and the longer transition zone is very small. The gap between the baseline and the shorter transition is larger, especially at higher Reynolds numbers.

5.2.2 Variation of the number of holes

Several tests were performed to assess the influence of the number of jets. In particular, 3 configurations were analyzed:

- 5 jets per channel: geometries 5510 (baseline) and 5505.
- 7 jets in the 1st channel and 5 jets in the 2nd: geometries 7505 and 7510.
- 7 jets per channel geometries: 7705 and 7710.

Two transition zone lengths were chosen for each hole configuration; due to the similarity of the results, only the data for the geometries with a short transition zone are reported here. Data for geometries with L_{trans}=10D are available in Gaffuri et al. (2021a).

Figure 5.10 depicts the Nusselt number distributions for the three jet configurations under consideration. Consistently with what was reported by Llucià et al. (2015), the presence of two additional jets does not affect the Nusselt number distribution of the upstream jets. Since the Reynolds number is defined using the mean jet velocity, by increasing the number of jets the total massflow is higher; this leads to a proportional increase of the crossflow velocity in the transition zone, leading to slightly higher Nu, at least in the centerline. This effect was found to be more pronounced for configurations with a longer transition (Gaffuri et al., 2021a), since for the short transition the flow of the last impingement jet affects the heat transfer on the majority of the transition.

Figure 5.11 shows the spanwise-averaged Nusselt number for the first and second channel at a Reynolds number equal to Re=20,000; results at other Re are qualitatively similar. In

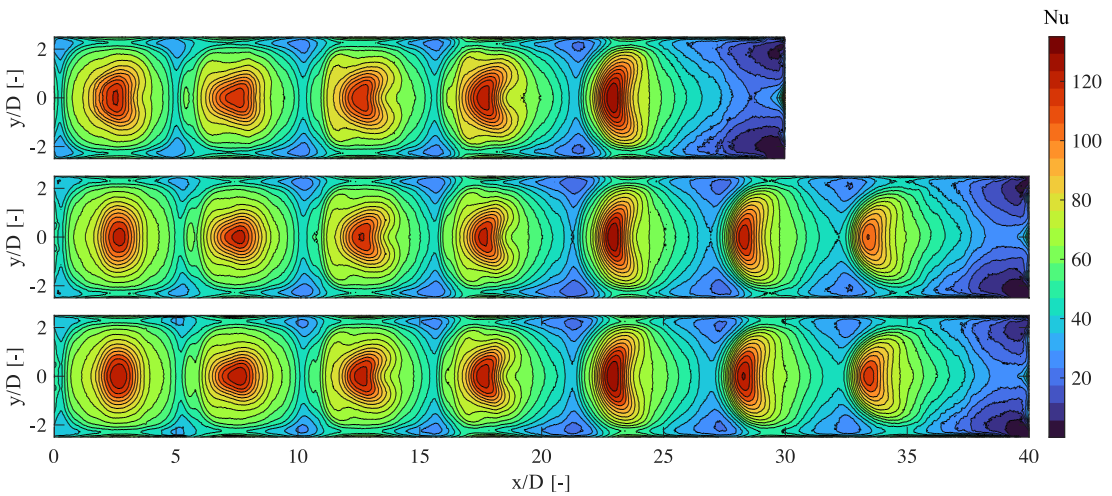

Figure 5.10 – Nu distribution on the target plate of the 1st channel for different number of jets at Re=20,000. Top: 5 jets per channel. Center: 7 jets in the first channel, 5 in the second. Bottom: 7 jets for both channels.

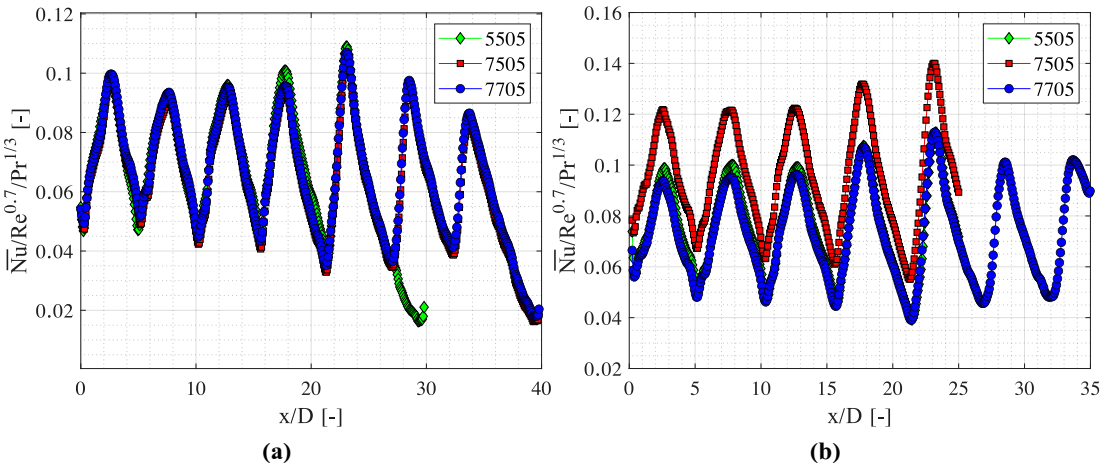

Figure 5.11 – Spanwise-averaged normalized *Nu* at *Re*=20,000 for (a) the 1st channel and (b) the 2nd channel.

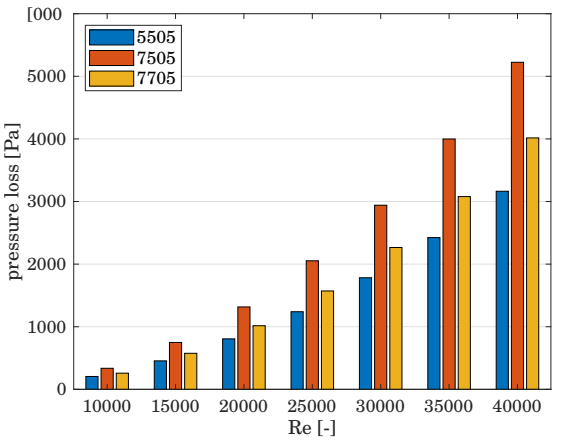

Figure 5.12 – Pressure losses of the complete channel for configurations with different number of jets per channel.

the left graph, the independence of the heat transfer to the total number of holes can be observed.

Since the Reynolds number is based on the average jet velocity in the 1st channel, if the number of jets differs between the channels, then the jet velocity is also different between the channels. Thus, by reducing the number of jets in the second channel the Nusselt number can be increased (see configuration 7505 in Fig. 5.11 (b)). This can be beneficial, since due to the heat pickup in the first channel, the cooling capacity in the second channel becomes lower. Increasing the average heat transfer coefficient can compensate the lower temperature difference driving the convective heat transfer. Of course, this strategy has some drawbacks: first, the covered area is smaller than a channel with 7 jets, and second, the smaller passage area (5 jets versus 7 jets) for the same massflow increases the pressure losses. This can be clearly seen in Fig. 5.12, where the geometry 7505 shows the highest losses. The configuration with 7 jets per channel has higher losses than the configuration

with 5 jets per channel; the difference is mainly due to the higher massflow passing through the purge hole, which has the same area for all configurations. The discharge coefficient of the impingement holes is similar for both configurations.

5.2.3 Effect of bypass holes

A bypass can be added to allow some of the flow to pass directly from the first channel to the second. This can bring some benefits to the overall performances of the cooling channel:

- the total passage area between 1st and 2nd channel is increased by the area of the bypass, potentially decreasing the pressure losses of the flow;
- the flow in the upstream part of the 2nd channel is modified, with the bypass flow providing enhanced heat transfer in this region of the target plate.

Three layouts of the bypass holes were tested (see Fig. 5.13); in all cases the bypass holes are circular and placed as close as possible (i.e. tangent) to the target plate. The configuration 5505B1 has 1 central bypass hole, configuration 5505B2 has 2 bypass holes placed at 1/3 and 2/3 of the width, and configuration 5510B4 has 4 bypass holes at 1/5, 2/5, 3/5 and 4/5 of the width. In all cases the total bypass area is equal to 1/2 of a single jet hole area, in order to keep the bypass massflow approximately constant for all configurations.

Results of the 1st channel show no noticeable impact of the bypass on the Nusselt number distribution. In the second channel, the addition of bypasses causes important changes in the *Nu* distributions (see Fig. 5.14). First, the bypass flow is essentially a jet flow parallel, and very close to, the target surface. This creates a local *Nu* increase. The bypass flow, however, disturbs the wall jet flow of the 1st impingement jet, and causes a drop of the Nusselt number in between the bypass flows, or in the case of the single bypass case, left and right of the bypass. This effect is mitigated by increasing the number of bypass jets, as can be seen in the case of 4 bypasses. The single bypass hole is placed on the channel centerline, and thus it is aligned with the jets. This causes a strong interaction between

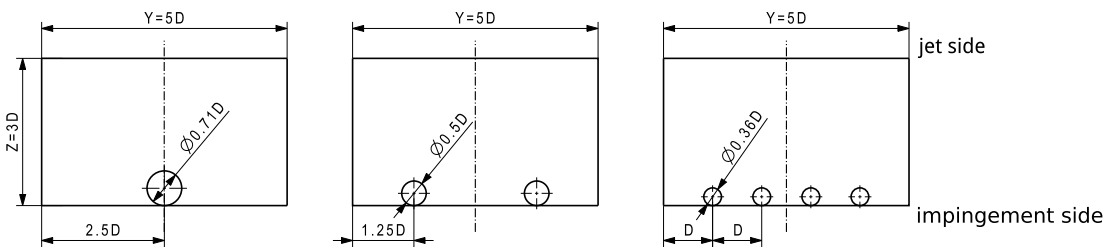

Figure 5.13 – Schematics of the bypass hole configurations investigated.

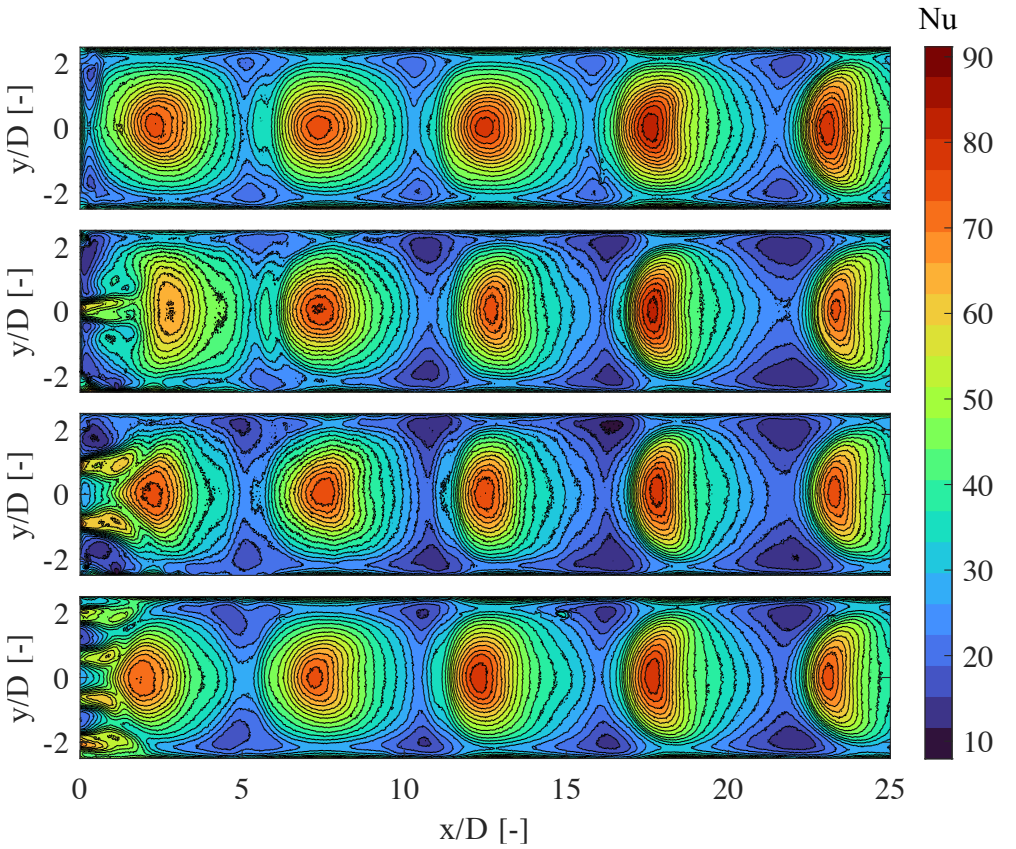

Figure 5.14 – *Nu* distribution on the target plate of the 2nd channel at Re=10,000 for the bypass cases. From top to bottom: no bypass, 1 bypass hole, 2 bypass holes, 4 bypass holes.

the jet and the bypass flow for this case, reducing noticeably the Nusselt number at the stagnation point and changing the *Nu* pattern.

Since a portion of the flow is bypassed, not all the air flows through the second plenum and the impingement holes of the second channel, and consequently the average jet velocity in the second channel is lower; this translates in lower Nu values both at the jet stagnation point, especially at jets 4 and 5 (see also Fig. 5.15 (a)), and in the wall jet region. The higher crossflow to jet flow ratio for the bypass cases results in an increased interaction of the crossflow with the jets, leading to a less round shape in the Nusselt number distribution and a shift downstream of the stagnation point (see the last jet). Additionally, the 1st jet is highly impacted by the bypass, leading to lower heat transfer, especially in the single bypass case where the bypass is aligned with the jet, and a deformed *Nu* pattern around the stagnation region (2 bypass case in particular). The 4 bypass case has increased values of the average Nu upstream of the 1st jet, and sees the least amount of reduction of the heat transfer in the impingement region. Thus, it seems that increasing the number of bypass holes improves the performances of the channel. However, if one aims to keep the total bypass area constant, the holes become smaller, and the manufacturability of such a feature quickly becomes challenging.

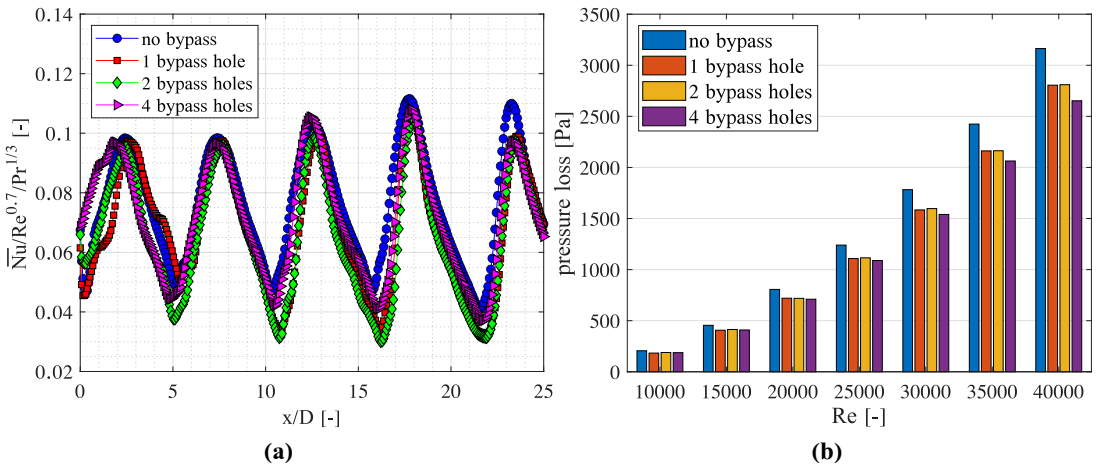

Figure 5.15 – (a) Spanwise-averaged normalized Nu at Re=10,000 for the bypass cases. (b) Pressure losses of the complete channel as a function of Re.

As expected, the pressure difference required to drive the flow decreases slightly with the addition of the bypass holes; this is due to the increased passage area between the first and second channel.

5.3 Heat transfer enhancement devices

If the baseline channel was to be installed in a hot component, the low heat transfer coefficients obtained in the transition zone would cause unacceptable temperature levels in this region. Moreover, the temperature gradient arising from the great difference of heat transfer coefficients between the impingement portion of the channel and the transition zone could cause excessive thermal stresses in the part, resulting in a shorter durability of the component, or even breakage. For a quantitative assessment of the resulting temperatures see Section 6.1.

Three main strategies for increasing the heat transfer in the transition zone are explored here: addition of ribs, addition of pins, and reduction of the cross-section of the channel by inserting a ramp in the transition zone on the jet plate side of the channel, with the aim of increasing the average flow speed in this zone. These strategies are evaluated using the baseline channel as a starting point for comparison of the heat transfer effectiveness and pressure losses.

5.3.1 Ribs

The function of the ribs is to generate a vortical flow that increases the mixing of the mainstream air with the boundary layer to increase the overall convection process. The

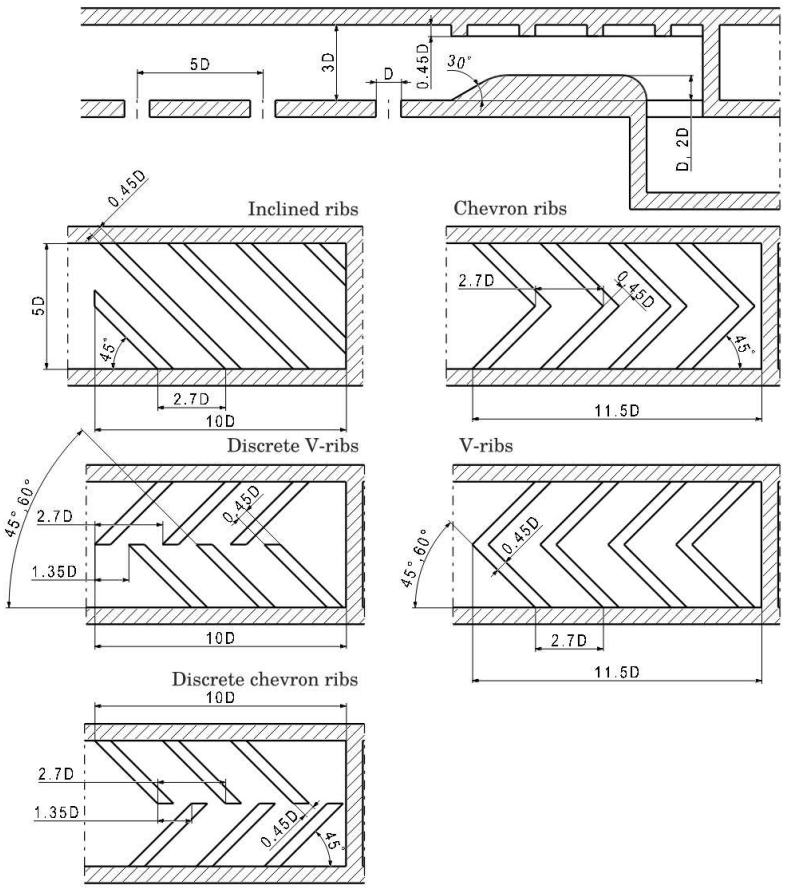

Figure 5.16 – Schematics and dimensions of the ribs tested. The side-view on top also depicts one version of the ramp analyzed in Section 5.3.3.

flow separates due to the presence of the rib, and at the reattachment point higher heat transfer can be achieved. Key parameters are the height e of the ribs and the pitch P, which have a great effect on the topology of the flow and consequently on the achievable heat transfer. Although experimental studies generally consider rib heights between 5 and 10% of the hydraulic diameter D_H, and P/e ratios from 7 to 15, the trend in modern gas turbine cooling designs is to use higher blockages and closer pitch (Han et al., 2012). Therefore, for the present study, ribs with a square section with e=0.45D have been chosen. This corresponds to 12% of the hydraulic diameter of the channel and 15% of the channel height. For the same reason, the pitch is set to P=2.7D, giving a ratio P/e equal to 6.

Another important parameter is the angle of the rib with respect to the incoming flow. As shown e.g. by Park et al. (1992), angles between 45° and 60° achieve the highest heat transfer augmentation at channel aspect ratios similar to the one investigated here (W/H=5/3), with the 60° angle providing higher heat transfer and the 45° lower losses. These two angles were therefore selected. The last parameter is the type of rib. This choice was mainly driven by the actual interest of the industrial partner and resulted in 5 types of ribs being analyzed: inclined ribs, V-ribs, chevron ribs, and discrete V-ribs and

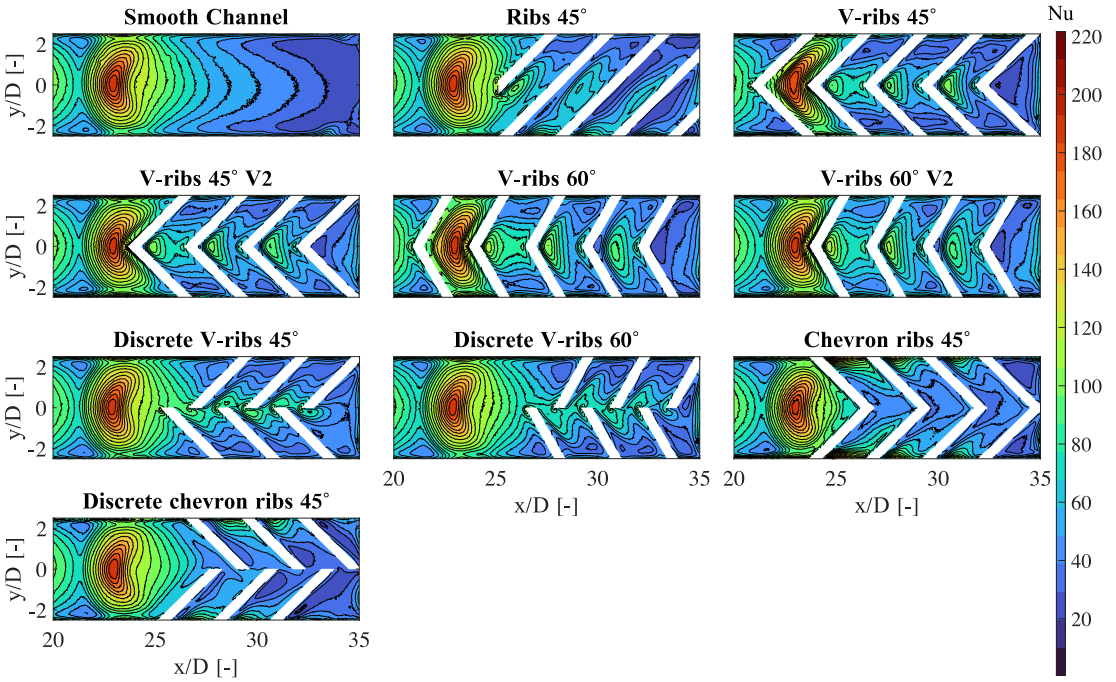

Figure 5.17 – Nusselt number distribution in the downstream part of the 1st channel (last impingement jet and transition zone) at Re=40,000 for the ribbed configurations.

chevron ribs. Details of these rib arrangements are presented in Fig. 5.16.

Figure 5.17 reports the Nusselt number distributions for the investigated ribbed configurations; only the last impingement jet of the first channel and the transition zone are shown, since the addition of ribs has no effect on the impingement zone heat transfer, apart from the last jet. All ribs allow for an increase of the Nu values in the transition zone. For all configurations, the discharge through the purge hole, which is on the opposite side of the channel, reduces the efficiency of the last rib, since the flow does not reattach to the target plate. This causes a reduction of Nusselt number near the end wall of the channel.

The V-ribs provide an increase in the central part of the transition zone, while the chevron ribs increase the Nu near the sidewalls; this is due to the different rotation direction of the vortices generated by the ribs (Boonloi, 2014), which move cool air from the mainstream to the target plate. This effect can be seen more clearly in Fig. 5.18, where the streamwise-averaged Nu values of the transition zone are shown for all 45° ribs (60° ribs are omitted for clarity). The average is computed by considering only the area not covered by the ribs, since experimental data for the ribs themselves are not available.

The last jet is in most cases largely unaffected by the ribs. Only the V-ribs interact with the jet flow near the stagnation region, changing the shape of the heat transfer pattern of the jet; this does not have a significant effect on the overall heat transfer in the impingement area of the last jet. Two versions of the V-ribs are investigated: one with the first rib upstream of the last jet, and one without (V2 in Fig. 5.17). The idea behind the choice of placing a rib upstream of the last jet is to protect the jet from the crossflow, but this

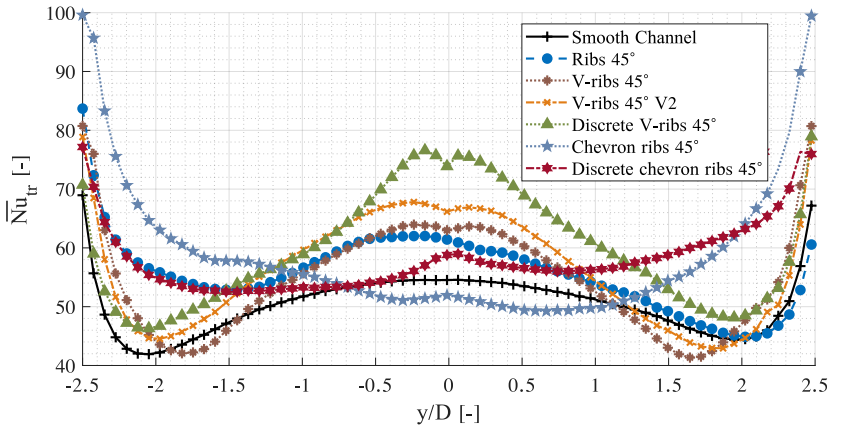

Figure 5.18 – Streamwise-averaged Nusselt number in the transition zone at *Re*=40,000 for the configurations with 45° ribs.

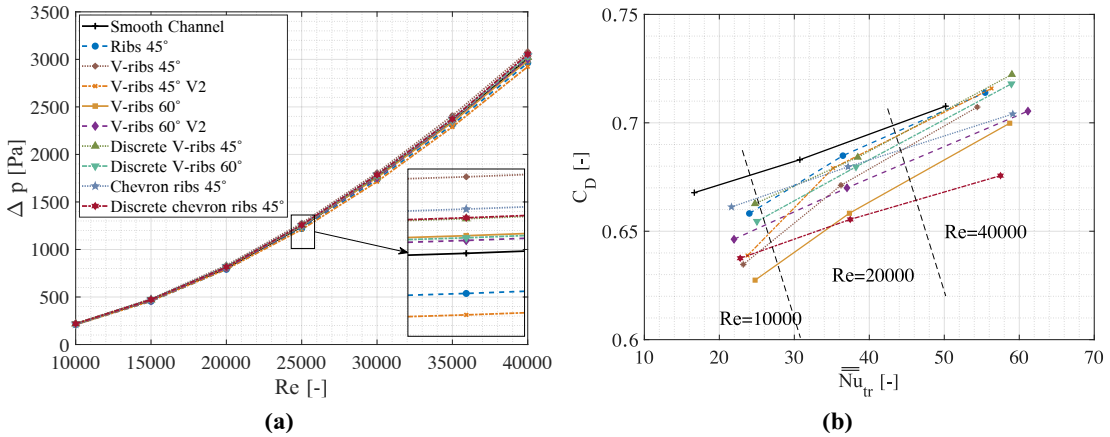

Figure 5.19 – (a) Channel pressure loss as a function of *Re* for the ribbed configurations. (b) Purge hole discharge factor as a function of the mean Nusselt number in the transition zone for the ribbed configurations.

does not seem to be effective since the *Nu* peak is similar to the baseline case. The first two ribs, however, confine the jet between them and alter the shape of its *Nu* pattern on the target plate.

Discrete V- and chevron ribs are obtained by shifting one half of the ribs half a pitch, and have 3 rows of ribs instead of 4. This reduces the interactions with the last jet. In the case of the chevron ribs, however, this somewhat reduces the heat transfer enhancement near the sidewalls since the first rib is less affected by the wall jet flow.

Figure 5.19 (a) shows the pressure drop of the complete channel of the ribbed configuration in comparison with the baseline configuration (blue line). The impact of the addition of the ribs is small in terms of pressure losses, with some configurations actually achieving lower losses than the baseline. This is attributed to the fact that the flow detachment at the last rib eases the flow into the purge hole, as discussed later in Section 5.3.3. Please

note, however, that the accuracy of the Δp measurement is in the order of $\pm 16\ Pa$, and thus a statistically significant difference between the configurations cannot be determined in each case.

Since the addition of the ribs has no effect on the heat transfer levels in the impingement area it is worthwhile to evaluate the performances of the ribbed configurations by focusing on the transition zone and purge hole only. Figure 5.19 (b) depicts the discharge coefficient of the purge hole, which includes the pressure losses of the transition zone, as a function of the area-averaged Nu of transition zone. It can be seen how the ribs allow for an increase of the mean Nu on the target plate; in absolute terms, the average Nusselt number can be increased by a value of between 4 and 9, depending on the configuration. In relative terms, the increase is more pronounced at low Re (30% to 50%) than at high Re (9% to 18%). This does not take into account the increased area which is available for heat transfer due to the addition of the ribs, which act as a heat sink to increase the total heat transfer. All in all, the experimental results show that ribs can increase significantly the mean Nusselt number in the transition zone with a moderate increase of the pressure losses, with some configurations that can actually reduce the losses associated with the purge hole flow, especially at high Reynolds numbers.

5.3.2 Pins

Three pin configurations were selected to be investigated in the test campaign. The first case features staggered vertical pins with a diameter equal to the jet diameter D. This results in a blockage of 40%. A case with 20% blockage was selected for comparison, with the same configuration but diameter equal to $D/2$. A staggered arrangement has been chosen as it was shown to provide higher heat transfer augmentation than inline pins (Sparrow and Lovell, 1980; Chyu et al., 1999). The third case features inclined pins, 2

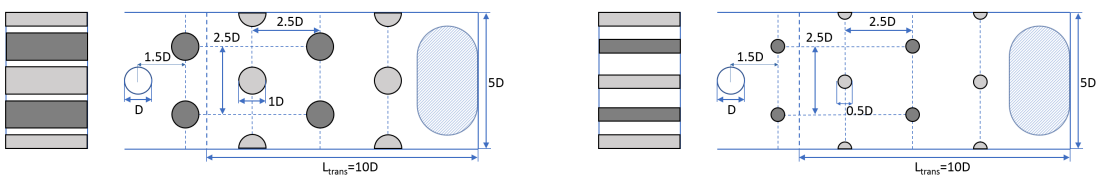

(a) Vertical pins **(b)** Small vertical pins

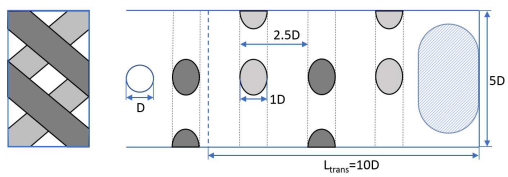

(c) Inclined pins

Figure 5.20 – Schematics of configurations with pins. The white circle is the last impingement hole, while the blue-shaded obround shape is the purge hole.

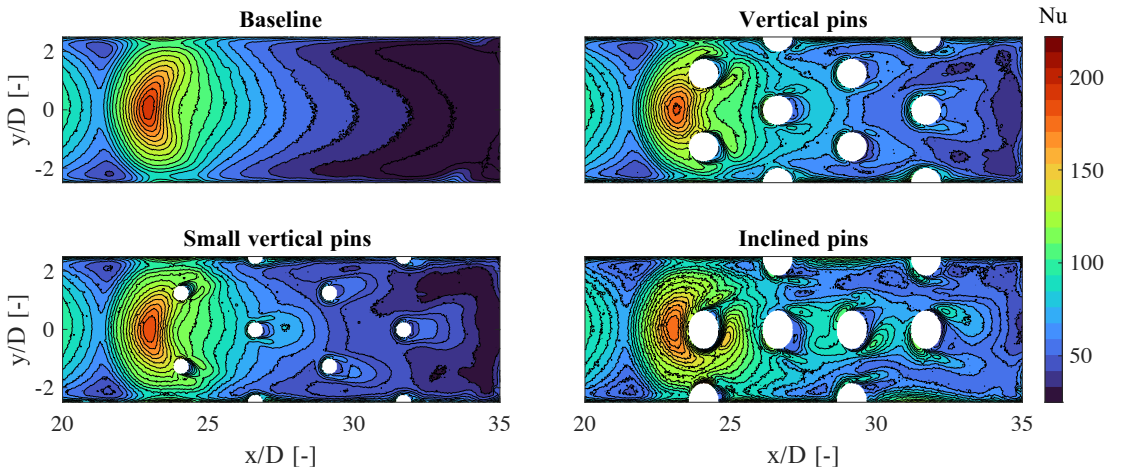

Figure 5.21 – Nusselt number distributions in the downstream part of the 1st channel (last impingement jet and transition zone) at Re=40,000 for the configurations with pins.

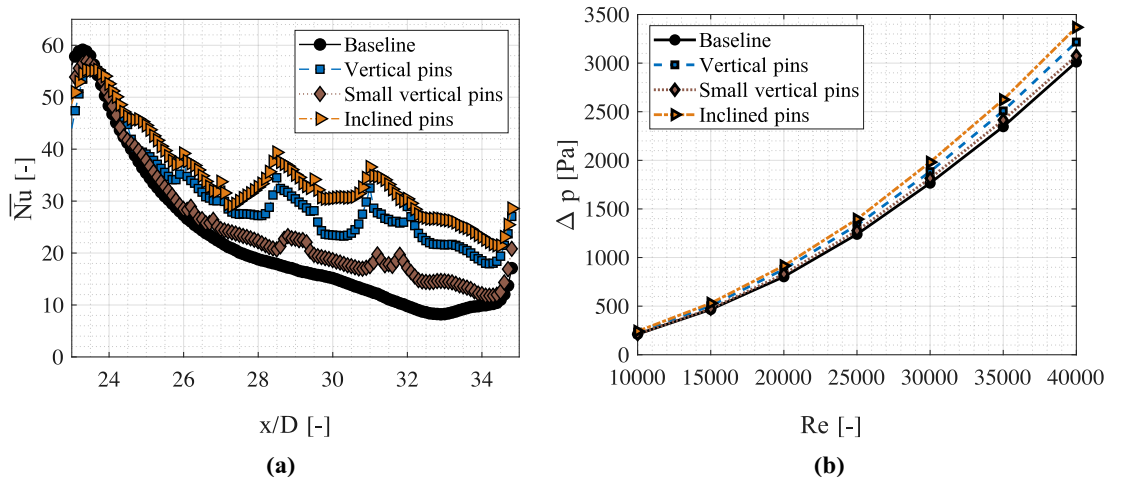

Figure 5.22 – Results of the configurations with pins and comparison with the baseline case. (a) Spanwise-averaged Nu in the transition zone at Re=40,000. (b) Channel pressure drop as a function of the Reynolds number.

pins per row with different direction each row. The inclination angle of approximately 50° is set so that each pin ends on one corner of the channel cross-section on one side of the channel and on the center line of the other side. Although the pin diameter is equal to the first case (1D), the blockage is higher due to the inclination of the pins (approximately 58.5%). This arrangement has been chosen considering the results obtained by VanFossen (1982) on short pins with similar arrangement. Schematics of these configurations are depicted in Fig. 5.20.

Figure 5.21 presents the Nusselt number for the baseline geometry and the pin cases for a Reynolds number equal to 40,000. For all configurations, the first row of pins is very close to the last jet stagnation point, which is about 0.5 jet diameters downstream of the jet hole position due to the crossflow of previous jets. It is debatable if this placement

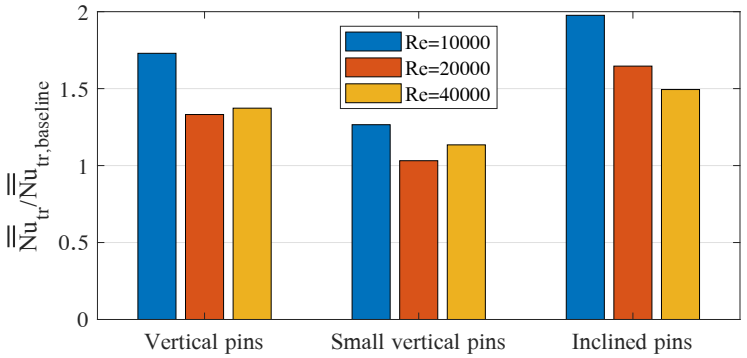

Figure 5.23 – Improvement, with respect to the baseline configuration, of the area-averaged Nusselt number in the transition zone for the configuration with pins.

improves the overall heat transfer, since heat transfer data for the pins themselves are not available. For the vertical pins case, an improvement of the heat transfer coefficient can be clearly seen both upstream and downstream of the pins due to the horseshoe vortex and the pin wake. At the end of the transition zone, a low heat transfer region persists, which is due to the flow turning towards the purge hole, leaving a zone with detached, recirculating low speed flow near the target plate. When reducing the pin diameter, similar observations can be made, but the beneficial effect of the pins is reduced, since the region affected by the presence of the pins is smaller. Inclined pins lead to an increase of the heat transfer coefficient both upstream and downstream of the pin. The Nusselt number patterns are more complex in this case and asymmetrical due to the asymmetric geometry configuration and its effect on the horseshoe vortices. The low heat transfer region at the end of the plate is reduced, but is still present on one side of the plate (upper side in the figure) albeit less pronounced. The reduction can be attributed to the enhanced mixing in the pin wake flows due to the asymmetric configuration of the inclined pins.

Figure 5.22 (a) reports the spanwise-averaged normalized Nusselt number for the last impingement jet and the transition zone. In all cases, the first row of the enhancement features interacts with the last jet impingement zone, reducing slightly the heat transfer values near the stagnation zone. However, the surface of the pin contributes to the overall heat transfer, counterbalancing this reduction. The small vertical pins produce only a marginal improvement in the transition zone over the baseline. The larger vertical pins show a more substantial improvement, which can reach 70% over the baseline (smooth) configuration. Finally, inclined pins show moderately higher heat transfer than the vertical pins.

Compared to the ribs, the improvement over the baseline is higher, and, like in the ribs case, is more pronounced at Re=10,000. The inclined pins almost double the average Nu in the transition zone at low Reynolds number (see Fig. 5.23).

The heat transfer enhancement goes hand in hand with an increase of the pressure losses of the flow. This can be seen in Fig. 5.22 (b), where the losses of the complete channel are plotted as a function of the Reynolds number. The losses are higher than in the case of

ribbed geometries, with higher blockages corresponding to higher losses. A more detailed comparison between different heat transfer enhancement devices is performed in Chapter 6.

5.3.3 Ramps

By inserting a ramp in the transition zone, the cross-section of the channel can be reduced at this location. The effect is that, for a given massflow, the mean flow velocity is increased, resulting in a higher heat transfer at the wall. To illustrate this, as a first approximation, let's consider that the flow in the transition zone is a fully turbulent pipe flow. The heat transfer in a pipe can be modeled with the Dittus-Bolter equation (Incropera et al., 2006):

$$Nu = 0.0023 Re^{0.8} Pr^{0.3} \tag{5.2}$$

Note that a more accurate formula for rectangular channel could have been used, but the Dittus-Bolter equation is adequate for this simple analysis. The Reynolds number here is based on the hydraulic diameter of the channel D_H and the mean flow velocity, which in our case is the crossflow velocity in the transition zone u_{cf}.

$$Re_{D_H} = \frac{u_{cf} D_H}{\nu} \tag{5.3}$$

Assuming a constant Prandtl number, the Reynolds number must be increased in order to increase the Nusselt number. By inserting a ramp, the height of the channel is reduced from H to H_{ramp}; the velocity is thus increased and the hydraulic diameter decreased:

$$\frac{u_{cf,ramp}}{u_{cf}} = \frac{H}{H_{ramp}} \tag{5.4}$$

$$\frac{D_{H,ramp}}{D_H} = \frac{H_{ramp}}{H} \frac{H + Y}{H_{ramp} + Y} \tag{5.5}$$

where Y is the width of the channel. By rearranging, the ratio of Reynolds numbers can be found as:

$$\frac{Re_{D_{H,ramp}}}{Re_{D_H}} = \frac{H + Y}{H_{ramp} + Y} \tag{5.6}$$

and since H_{ramp} is smaller than H, the Reynolds number is increased.

Two types of ramps have been investigated (see Fig. 5.24): one that ends with a round corner at the beginning of the purge hole (short version) and one that continues to the downstream endwall of the channel, with a cutout that matches the purge hole (long

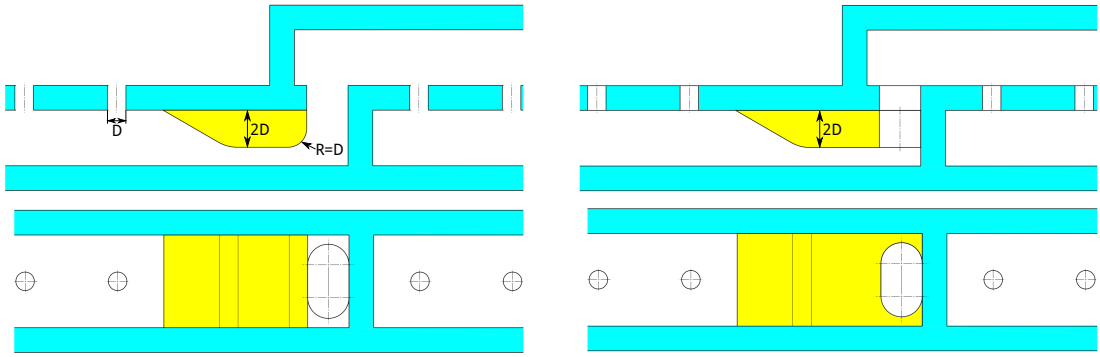

Figure 5.24 – Schematics of the ramp inserts for the reduction of the cross-section in the transition zone. Left: short version. Right: long version. A smaller version of the short version (with height H=1D) is also investigated.

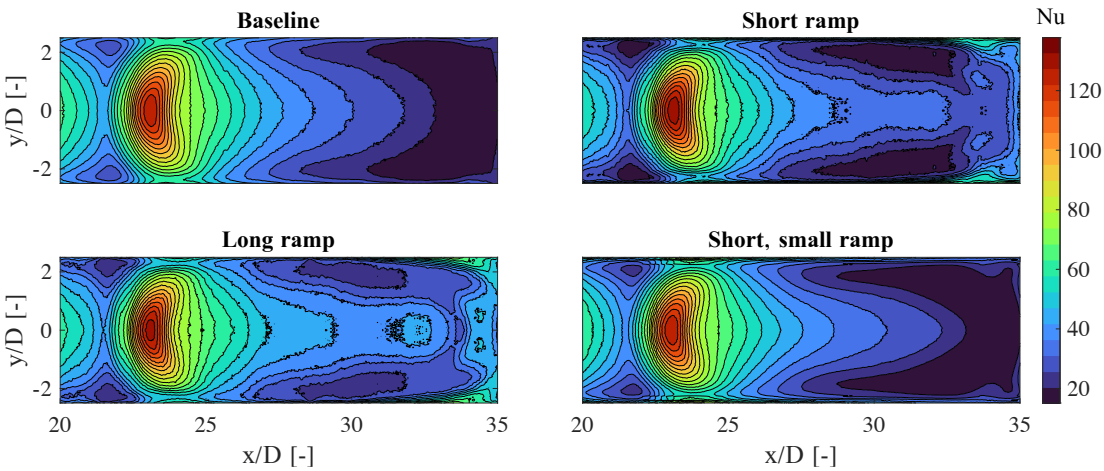

Figure 5.25 – Nusselt number distributions on the downstream part of the 1st channel (last impingement jet and transition zone) at Re=20,000 for the configurations with ramps.

version). The two types of ramp follow very different design considerations: the long ramp is meant to reduce the channel cross-section up to the endwall, thus maximizing the enhancement. The short ramp, on the other end, with the rounded corner, tries to conform to the discharge flow, with the possible drawback of a reduction of the heat transfer in the most downstream part of the channel. The ramps are installed on the impingement plate, opposite the target surface. This choice is dictated by the fact that in a real case scenario, the external wall needs to be kept as thin as possible to maximize the heat transfer, and increasing the wall thickness to install the ramp would further reduce the heat transfer in the transition zone.

All configurations have a ramp angle of 30° and start at the beginning of the transition zone (x/D=25). The maximum height of the ramps is H=2D; since the channel height Z is equal to 3D, the blockage is 67%. For the short version, a variation with a smaller height (H=1D) is also investigated. By using Eq. 5.2 together with Eq. 5.6, the Nu enhancement can be estimated in 11% and 26%, for the ramps with height 1D and 2D, respectively.

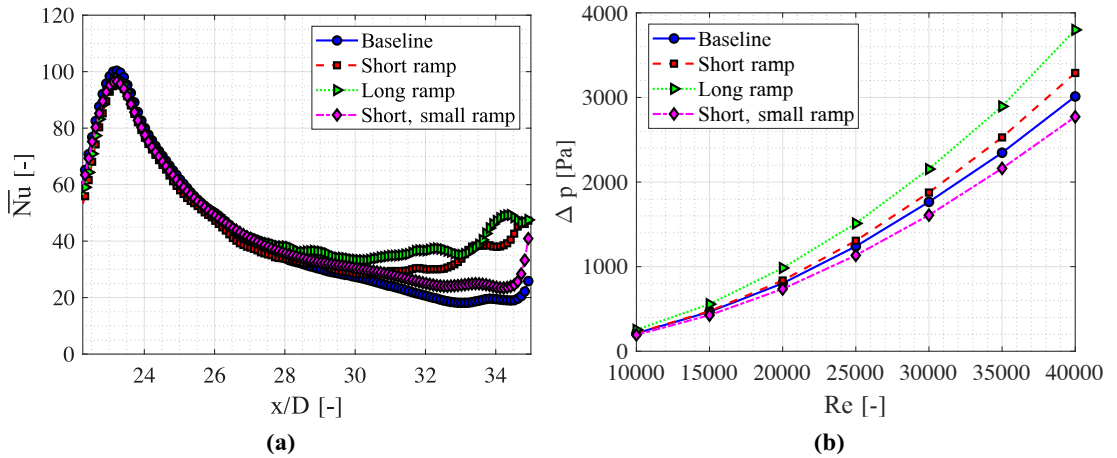

Figure 5.26 – Results of the configurations with ramps and comparison with the baseline case. (a) Spanwise-averaged Nu in the transition zone at Re=20,000. (b) Channel pressure drop as a function of the Reynolds number.

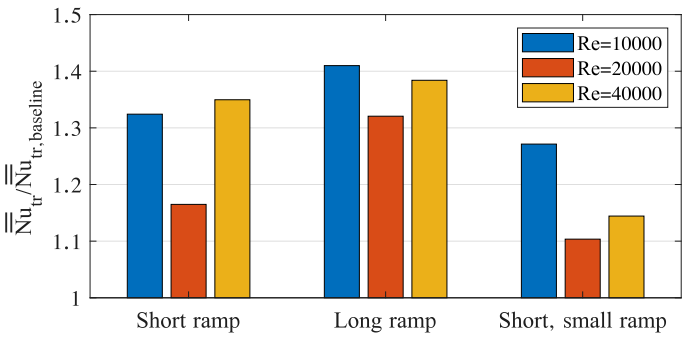

Figure 5.27 – Improvement, with respect to the baseline configuration, of the area-averaged Nusselt number of the transition zone for the configuration with ramps.

Figure 5.25 depicts the Nusselt number distribution in the downstream part of the first channel. In all cases an increase of the heat transfer can be observed. The increase is maximal for the long ramp, and minimal for the smaller version of the short ramp. These findings can be confirmed by looking at the spanwise-averaged data in Fig. 5.26 (a). For the short ramps, however, the Nu levels near the sidewalls actually decrease compared to the baseline. The relative improvements range from 10% to 40%, depending on the geometry and Reynolds number (Fig. 5.27); this is in good agreement with the estimations performed above with the Dittus-Bolter equation, especially considering the simplified analytical approach used.

The short version performs better than the long version with respect to the pressure losses (Fig. 5.26 (b)). This is due to the fact that the rounded corner at the end of the short ramp guides the flow into the purge hole, reducing the flow detachment associated with the sharp corner at the exit of the first channel (see Fig. 5.3 for a visualization of this flow detachment). For the same reason, the smaller version of the ramp actually shows lower losses than the baseline.

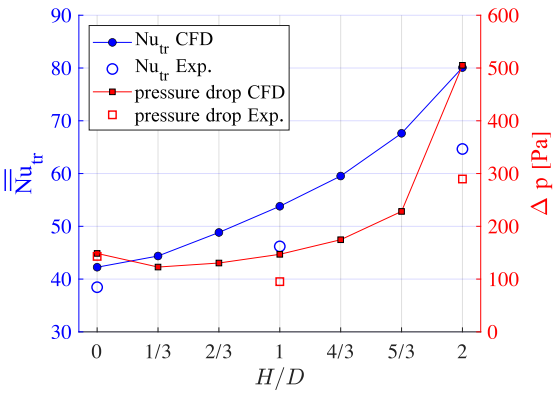

Figure 5.28 – Area-averaged Nu and channel pressure losses as a function of the ramp height H at Re=20,000 obtained through CFD analysis for a configuration featuring a ramp and discrete V-ribs in the transition zone.

To evaluate the influence of the ramp height on the pressure losses and the heat transfer, a sensitivity analysis by means of CFD has been performed. For this study, a geometry featuring both a ramp and discrete V-ribs (presented in detail in the next section) has been chosen. Simulations have been performed using the open source tool SU2 (Economon et al., 2016), solving the low-Mach Navier-Stokes equations (Müller, 1998) with Menter's k-ω shear stress transport (SST) turbulence model (Menter, 1994). The details of the numerical setup are available in Appendix C.

The CFD results (Fig. 5.28) indicate that the heat transfer increases when increasing the height of the ramp, which is expected. The pressure losses, however, have a minimum for a ramp height of 1D, and increase again for lower H. This is due to the fact that for ramp heights smaller than 1D, the rounded corner at the end of the ramp must have a smaller radius, so that the flow separation cannot be reduced as effectively. In the same graph, the available experimental data for the same geometries have been included. For the case without the ramp (H/D=0), the agreement is excellent; when adding the ramp the trend is correctly captured, although in the CFD both the Nu and the pressure drop are underestimated. This shows the need of experimental data for the assessment of the numerical results.

5.4 Combination of heat transfer enhancement devices

It is common to compound several enhancement techniques to improve the average heat transfer coefficient (Han et al., 2012). In the last experimental campaign of this project, some configurations have been designed based on the findings of the previous tests, to try to optimize the thermal performance of the channel while minimizing the impact on the pressure losses.

Firstly, among the ribbed configuration, the discrete V-ribs at 45° show the best performance in terms of heat transfer enhancement with relatively low pressure losses (see

Fig. 5.19 (b) for reference). A combination of these ribs with a ramp could result in further enhancements, especially with a small ramp. It was noted in previous sections how the chevron ribs improve the heat transfer on the sides of the target plate, due to the rotation direction of the vortical flow. Combining them with a ramp, that has been shown to increase the heat transfer near the centerline, could be an effective solution for further enhancements. For consistency with the previous case, and due to their good performance, the discrete chevron ribs have been chosen for this. Both ribbed configurations have been tested with the short ramps (small, H=1D, and large, H=2D).

In addition to these configurations, it was decided to combine pins and ribs, and to do this a solution inspired by a recent patent (Krueckels and Widmer, 2013) has been chosen. This consists of staggered pins, with ribs that connect them on the target plate forming a rhomboidal pattern. This configuration has also been coupled with the small, short ramp, and with bypass holes, with the aim of reducing the pressure losses, that are expected to be high due to the combination of ribs and pins, that occupy a large part of the cross-section, leaving a relatively small passage area for the flow.

5.4.1 Ribs combined with ramps

The addition of a ramp to the configurations with discrete ribs increases the heat transfer coefficient in the transition zone. This is true for both the V-ribs and the chevron ribs (Fig. 5.29). The Nu increase, compared to the configuration without the ramp, is moderate for the small ramp, and stronger for the big ramp case, with Nusselt numbers in the transition zone locally reaching similar values as in the jet stagnation zone.

The relative increase of the Nusselt number due to the addition of the ramp can be assessed more clearly in Fig. 5.30. In this graph a diverging colormap is used to distinguish between values smaller or higher than unity; red colors denote regions of relative improvement and blue colors indicate regions in which Nu decreases. In the impingement area, values very close to one are found, as can be inferred by the light blue or red in the graph, depending if the values are above or below one. The range of values in this area spans from 0.99 to 1.02, which is in line with the repeatability values obtained in the validation of the experimental technique in Section 4.4.1. Therefore, it can be concluded that the addition of the ribs does not affect the Nu distribution in the impingement area. The addition of the ramp improves the heat transfer in a similar manner for both ribs configurations. With the small ramp, the improvement reaches locally 60%, and with the big ramp more than 300%. The complete transition zone sees an improvement, with some exceptions upstream or downstream of the ribs. This can be attributed to the different detachment and reattachment lines of the rib-generated vortex due to the presence of the ramp, which modifies the vortex tube shape by constraining it in the smaller channel height.

The Nusselt number increase compared to the baseline, and to the cases with the respective ribs without the ramp, can be estimated via the spanwise-averaged Nusselt number values

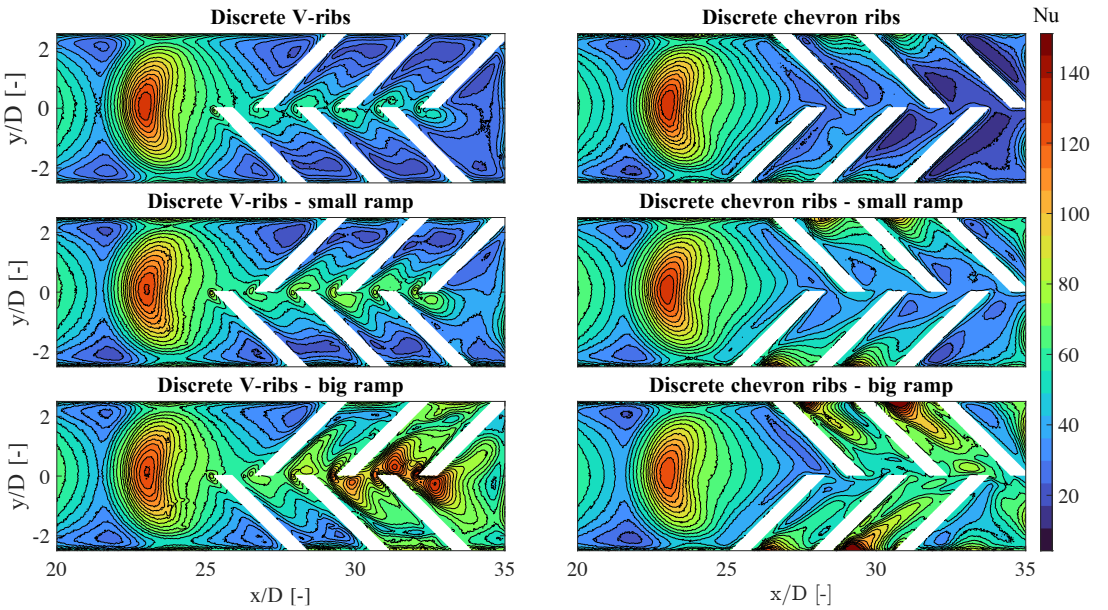

Figure 5.29 – Nusselt number distributions on the downstream part of the 1st channel (last impingement jet and transition zone) at *Re*=20,000 for the configurations with ribs and ramps.

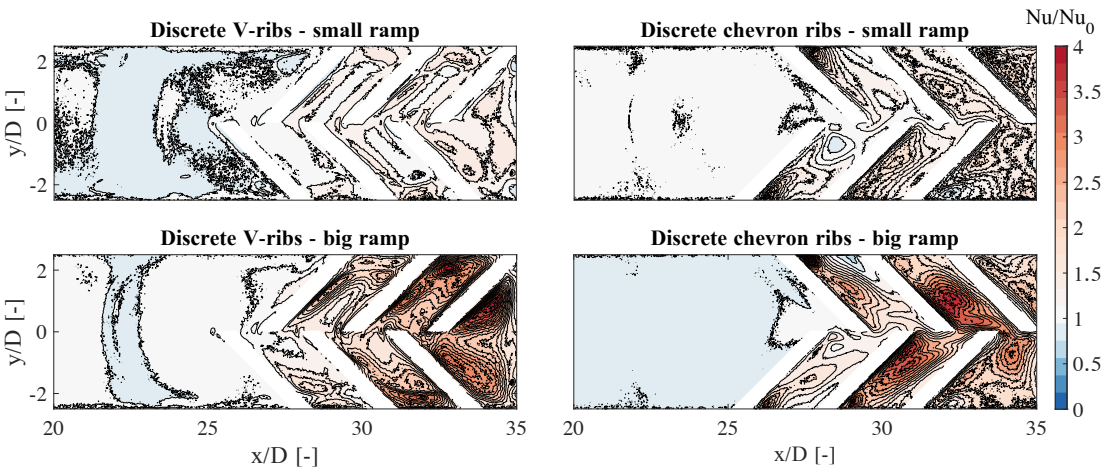

Figure 5.30 – Improvement of the Nusselt number, relative to the corresponding configuration without ramp, at *Re*=20,000 for the configurations with ribs and ramps. Only the downstream part of the 1st channel (last impingement jet and transition zone) is shown.

in Fig. 5.31 (a). The V-ribs, especially when installed with the big ramp, achieve the maximum heat transfer more downstream in the transition zone than the chevron ribs. This is caused by the different flow topology, and the different locations of the flow reattachment lines.

Figure 5.31 (b) reports the pressure measurements for these configurations in comparison with the baseline geometry and the configurations without ramps. As was seen in Section 5.3.1, the pressure losses of the ribbed configurations are very similar to the baseline geometry, only slightly higher. By adding the small ramp, the effect on the pressure losses

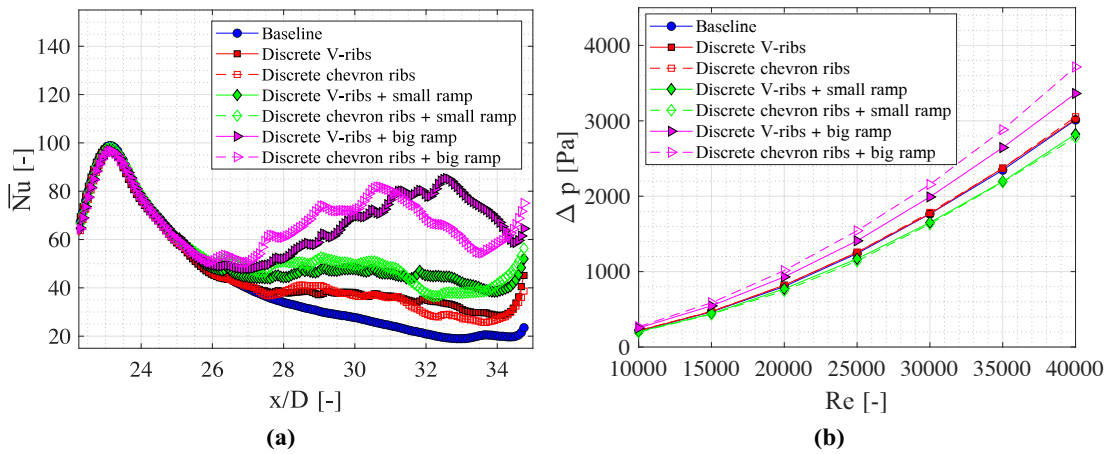

Figure 5.31 – Results of the configurations with ribs and ramps, and comparison with the baseline case. (a) Spanwise-averaged *Nu* in the transition zone at *Re*=20,000. (b) Channel pressure drop as a function of the Reynolds number.

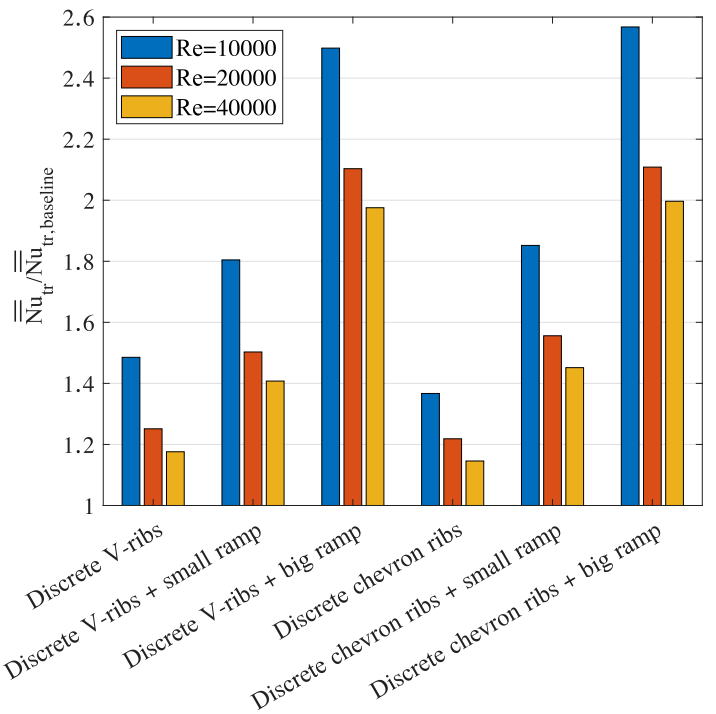

Figure 5.32 – Improvement, with respect to the baseline configuration, of the area-averaged Nusselt number of the transition zone for the configuration with ribs and ramps.

is similar to the addition of a ramp in the smooth channel: by reducing the detachment at the purge hole, the losses can be reduced. The small ramp can therefore be added to the ribbed configurations tested here (and possibly all other ribbed configurations in the test matrix) without penalty. With the bigger ramp, however, the small passage area increases the losses noticeably, with the discrete chevron ribs exhibiting higher losses than the V-ribs.

The area-averaged Nusselt number improvement due to the addition of the small ramp can reach 80% above the baseline (smooth) case and approximately 20% above the ribbed case without ramp at low *Re* (Fig. 5.32). For the bigger ramp, the improvement can exceed 150%, but as mentioned, the impact in terms of pressure losses is significant.

5.4.2 Pin-ribs with ramps or bypass

A schematic of the configuration combining pins and ribs is presented in Fig. 5.33. Results show that the Nusselt number can be increased dramatically in the region between the ribs (see Fig. 5.34). When the small ramp is added to it, the heat transfer levels can reach, locally, the same value as in the jet stagnation zone. For both cases the maximum is located near the sidewall, downstream of the first half-pin. The addition of a bypass – in this case the version with 2 bypass holes has been chosen – does not change the *Nu* level or distribution in the transition zone (see also Fig. 5.35 (b)). However, the average *Nu* in the second channel is reduced between 15% (at *Re*=40,000) and 23% (at *Re*=10,000) due to the lower impingement massflow in the second channel, as was mentioned in Section 5.2.3. If such a reduction is tolerable depends on the specific implementation and on the detailed design of the cooling system, in particular with consideration of the external heat load distribution.

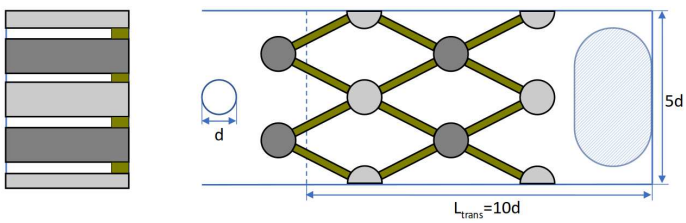

Figure 5.33 – Schematics of the pin-ribs configurations.

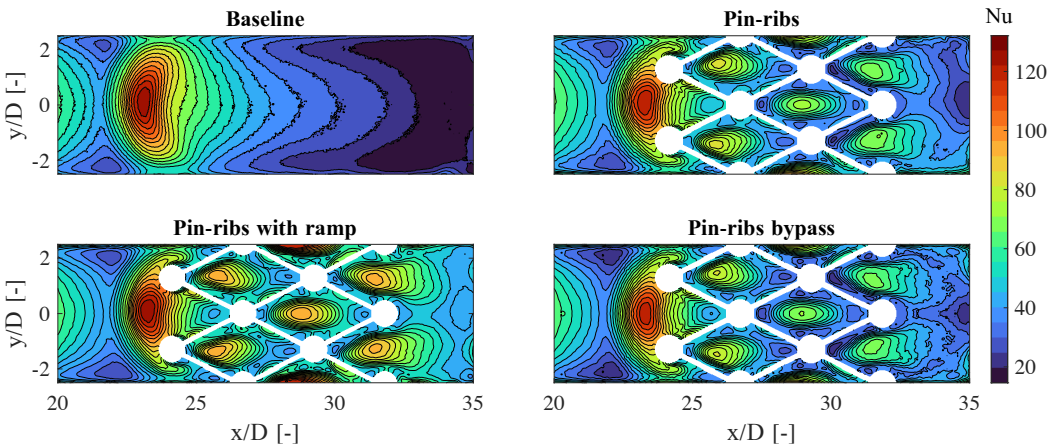

Figure 5.34 – Nusselt number distribution on the downstream part of the 1st channel (last impingement jet and transition zone) at *Re*=20,000 for the configurations with pin-ribs.

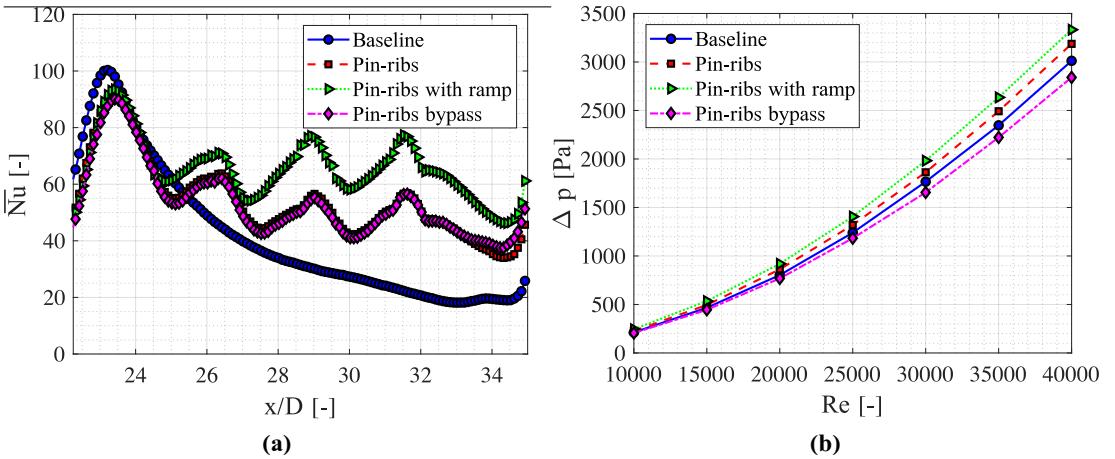

Figure 5.35 – Results of the configurations with pin-ribs, and comparison with the baseline case. (a) Spanwise-averaged Nu in the transition zone at Re=20,000. (b) Channel pressure drop as a function of the Reynolds number.

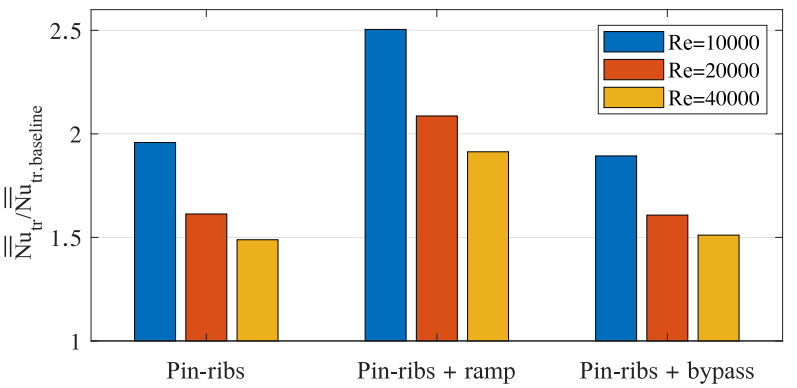

Figure 5.36 – Improvement, with respect to the baseline configuration, of the area-averaged Nusselt number of the transition zone for the configuration with pin-ribs.

Contrary to the previous cases, the addition of a ramp does not reduce the pressure losses, but it increases them instead (see Fig. 5.35 (b)). This is due to the high blockage of the pin-ribs configuration when combined with a ramp. The addition of a bypass achieves a noticeable reduction of the pressure losses, which fall even below the baseline case. The reduction of the heat transfer coefficient in the second channel, however, counterbalances this gain.

In terms of potential improvement, the pin-ribs configuration can almost double the average Nu values (at low Re) in the transition zone compared to the baseline, and with the addition of a ramp it can even achieve an improvement of 150%, similar to the ribbed geometries with the ramp. Finally, adding the bypass reduces slightly the average Nu in the transition zone, but this effect is negligible, especially if compared to the Nusselt number reduction in the impingement area of the second channel caused by the bypass flow.

5.5 Conclusions

In this chapter, the heat transfer characteristics and pressure losses of the investigated geometries have been presented. Results on the smooth geometries have highlighted the issue of the low heat transfer in the transition zone. The addition of heat transfer enhancement features allows to increase the mean Nu in the transition zone to levels similar to those achieved in the impingement area, with a trade-off on the pressure losses or on the average Nu in the second channel.

A comparative analysis of the performances of these cooling solutions is needed to determine the optimal solutions, which will of course be trade-offs between the achievable heat transfer and the acceptable pressure drop along the channel. Such a study is performed in the next chapter.

Chapter 6

Analysis and discussion

Using the data obtained during the experimental campaigns, which was presented in Chapter 5, the performances of a sequential impingement channel in operational conditions are analyzed and compared to a single impingement channel of the same length in Section 6.1. In Section 6.2, all the tested geometries are ranked in a multi-objective way to determine the most promising configurations. The identified solutions are then evaluated in a realistic scenario in Section 6.3, by estimating the efficiency improvement of a gas turbine equipped with sequential impingement channels, using a "0D" blade cooling problem and considering the complete thermodynamic cycle. A preliminary version of the analysis in Section 6.1 was presented at the ASME Turbo Expo 2021 (Gaffuri et al., 2021b).

6.1 Comparison to a single impingement channel

To assess the performance of the sequential impingement channels, the evolution of the coolant and the target plate temperatures along the channel are derived with a simplified analytical approach for a realistic scenario, and the results are compared to a single impingement channel of the same length. In a first step, the baseline channel is evaluated, and in Section 6.3, the same framework will be used for a more in depth evaluation of the "optimal" configurations identified in Section 6.2.

To have a fair comparison with the baseline sequential impingement channel (2 channels with 5 jets), a single impingement channel with 12 holes has to be considered, since the transition zone has the same length as the area cooled by 2 jets. For the same reason, it is considered that the channels have the same jet-to-jet spacing and channel cross-section.

Since no tests have been performed during this project on a 12 holes channel, data from Hossain et al. (2014) are used, which refer to a narrow channel of a single row of 15

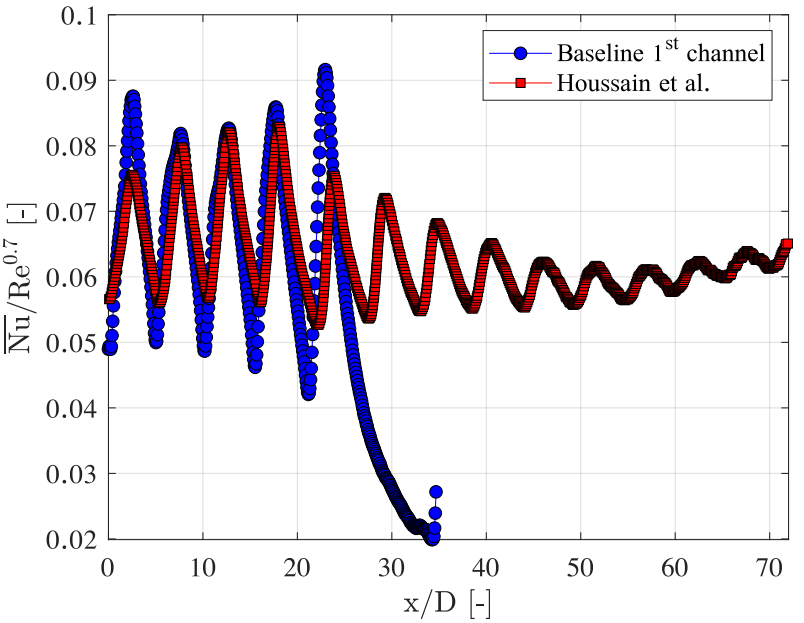

Figure 6.1 – Spanwise-averaged, normalized Nusselt number for the first channel of the baseline sequential impingement configuration (blue) at Re=40,000 and a single channel with 15 holes at Re=30,000 (red, data extracted from Hossain et al. (2014)).

impingement jets. Results of the first 12 jets of this 15 jet channel are exploited in the analysis. This is a reasonable approach, since it has been shown that the addition of more jets downstream does not affect the heat transfer coefficient distribution of the upstream jets (Llucià et al., 2015). Jet-to-jet spacing (X/D=5) and jet-to-plate distance (Z/D=3) are the same as in the baseline case. The main difference is that the width of the channel in Hossain et al. (2014) is Y/D=4 instead of Y/D=5 for the sequential impingement. The results, however, compare well with the present study when normalized by the Reynolds number (Fig. 6.1) for the first five jets: the discrepancy of the minima may be attributed to the different channel width, and the discrepancy of the maxima for jet number 4 and 5 to the different crossflow velocity and to the different outflow orientation. The cause for the discrepancy of the first maximum is unclear, but it has to be noted that the spacing between the first jet and the upstream wall seems to be 5.5 jet diameters in the referenced study according to the graphs, while it is 2.5 jet diameters in the present study. Nevertheless, the area-averaged Nu for the first five holes is very similar between the two studies: $Nu/Re^{0.7}$=0.063 for the single channel, $Nu/Re^{0.7}$=0.067 for the sequential channel. The data need to be normalized by $Re^{0.7}$ since they are not available at the same Re: Hossain et al. (2014) published data at Re=30,000, while the present study has data for Reynolds numbers 20,000 and 40,000.

For the evaluation of the cooling solution, an approach based on an energy balance at each jet is chosen. An actively cooled part is considered, for example the stator vane of the first stage of a gas turbine. The vane is heated on the external surface by a flow at T_{ext}=1800 K with a uniform heat transfer coefficient h_{ext}=2000 W/m^2K, while the coolant at the entry of the channel has a temperature of T_{C_i}=650 K. The temperature

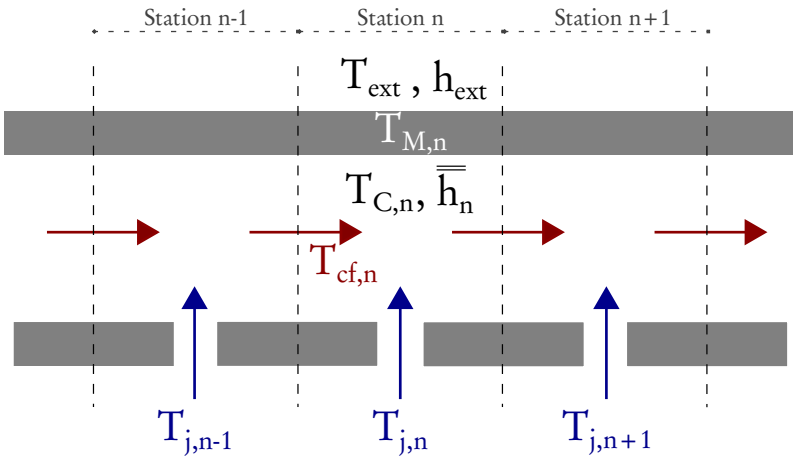

Figure 6.2 – Schematics of the zero-D problem used for the evaluation of the sequential impingement channel.

levels were chosen to correspond roughly to those of Ansaldo GT26 gas turbine, which is used for the evaluation of the possible benefits of the sequential channels for the thermal efficiency of a gas turbine in Section 6.3. The internal surface of the vane is cooled by impingement using either a single narrow impingement channel with 12 jets, or a double sequential impingement channel with 5 jets per channel and a transition zone of length 10 D. The vane wall is considered a lumped capacitance so that the temperature through the thickness can be considered constant. Additionally, the cooling channel is divided in "stations", one for each impinging jet, in which the internal heat transfer coefficient is averaged (see also Fig. 6.2). With these assumptions, the wall and coolant temperatures along the channel can be computed using an energy balance between the external and the internal heat transfer at station n:

$$h_{ext}(T_{ext} - T_{M,n}) = \overline{\overline{h_n}}(T_{M,n} - T_{C,n}) \tag{6.1}$$

In Eq. 6.1, $\overline{\overline{h_n}}$ is the area-averaged heat transfer coefficient of the coolant at the station n, $T_{M,n}$ is the metal blade temperature, and $T_{C,n}$ is the coolant temperature, which is the massflow-averaged temperature between the jet temperature $T_{j,n}$ at the station considered and the temperature of the crossflow $T_{cf,n}$:

$$T_{C,n} = \frac{\dot{m}_{j,n}}{\dot{m}_{j,n} + \dot{m}_{cf,n}} T_{j,n} + \frac{\dot{m}_{cf,n}}{\dot{m}_{j,n} + \dot{m}_{cf,n}} T_{cf,n} \tag{6.2}$$

in which $\dot{m}_{j,n}$ and $\dot{m}_{cf,n}$ are the massflows of the jet and of the crossflow, respectively, at station n.

The crossflow temperature at station n can be computed by adding the heat picked-up at station $n-1$ (of surface area A) to the coolant temperature at station $n-1$:

$$\dot{m}_{n-1} c_p \Delta T = h_{ext}(T_{ext} - T_{M,n-1})A \tag{6.3}$$

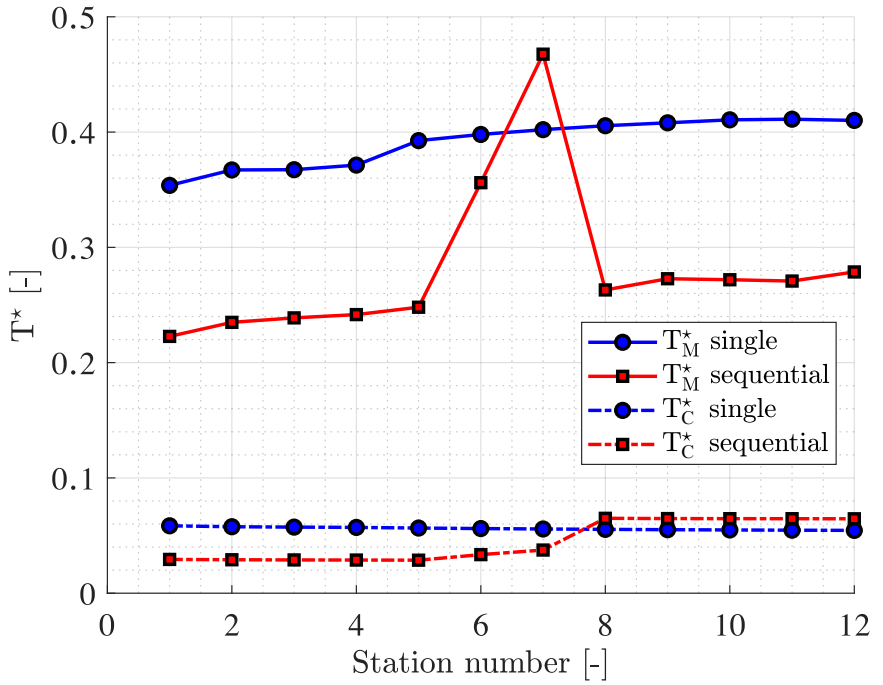

Figure 6.3 – Coolant and metal non-dimensional temperature distribution along the channel according to the analytical model.

$$T_{cf,n} = T_{C,n-1} + \Delta T \tag{6.4}$$

For the sequential channel, the procedure is altered to take into account the different flow conditions: in the transition zone (stations 6-7), there are no jets, so that only the crossflow is considered without addition of "fresh" air. Additionally, in the second channel, the jet temperature is the coolant temperature at the exit of the first channel.

For the comparison between the channel types, the total coolant massflow is kept constant, which means that the jet Reynolds number of the sequential case is higher than in the single channel case, since less jets are fed with coolant air (5 instead of 12).

The resulting metal and coolant temperature along the channel are plotted in the graph of Fig 6.3 in non dimensional form, which corresponds to the following formula:

$$T^{\star} = \frac{T - T_j}{T_{ext} - T_j} \tag{6.5}$$

The jet Re is higher in the sequential case, which results in a better cooling and lower temperatures compared to the single channel case. In the transition zone, however, the metal temperature increases sharply, due to the fact that the heat transfer coefficient is lower and there is no addition of fresh air via the jets. Since it is used 2 times for cooling,

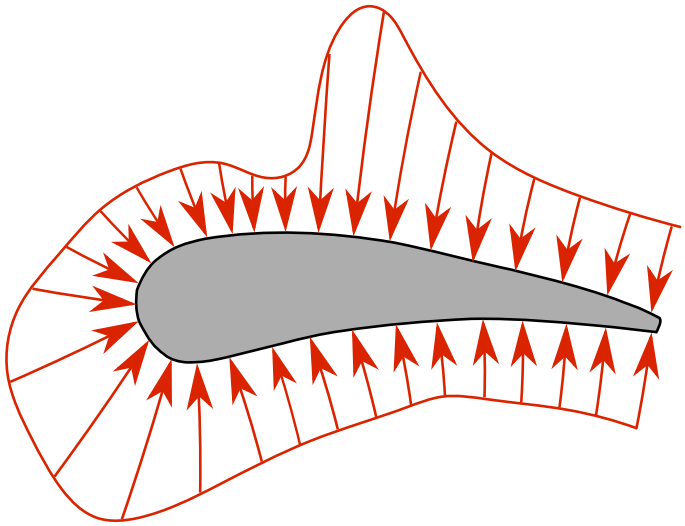

Figure 6.4 – External heat load on a stator vane. Drawn based on a image from Han (2018).

the coolant air temperature at the outlet is higher for the sequential case, which hints at a better use of the coolant. The maximal metal temperature, however, is higher in the sequential case than in the single channel, with the maximum occurring at the end of the transition zone. Additionally, the temperature gradient is very high at the beginning and end of the transition zone; this could result in unacceptable thermal stresses in the blade in operation. If one were to install the baseline sequential channel in a machine equipped with the single channel, the maximal temperature of the metal part to be cooled would be higher, and possibly exceeding the maximum allowable temperature, if the initial design was already at the limits of the feasible temperature range. For this reason, heat transfer enhancement features are required to reduce the metal temperature in the transition zone.

It can be observed in the graph of Fig. 6.3 that the blade temperature tends to increase along the channel; this is to some extent also the case for a long single impingement channel (blue line). While in this example it was considered that the external heat transfer coefficient is constant, in reality it varies along the blade. If the channel is installed in a stator vane in a chordwise direction, the impingement area of the first channel would be at the leading edge, where the heat load is high, and the transition zone would be further downstream where the heat load is somewhat lower, reducing the metal temperature increase. This is true especially for the pressure side of the airfoil (see Fig. 6.4); on the suction side, the maximum occurs after the laminar/turbulent transition and this requires careful analysis during the design of the cooling system to ensure that the maximum temperature is not exceeded. On the other hand, the first stage of the turbine is usually designed with a low degree of reaction R_H, meaning that the enthalpy (and temperature) drop occurs mainly along the stator, which allows for a reduction of the total temperature of the flow in the downstream direction along the chord.

6.2 Multi-objective evaluation of the configurations

With so many different configurations investigated, there is a need to evaluate their performances in an objective way. The performance of a cooling solution depends essentially on two parameters: the average heat transfer coefficient, or Nusselt number, and the pressure differential needed to drive the flow. However, a comparison based on these 2 parameters would fail to take into account some key differences between some of the channels:

- the cooled surface is different for some configurations (e.g. increased number of jets, different length of the transition zone);
- the coolant massflow used depends on the number of jets in the 1st channel for a given Reynolds number.

For a more comprehensive criterion to judge the thermal performance of each configuration, the above 2 points must be included in the evaluation. To do this, correction factors are introduced in the heat transfer performance by multiplying the average Nu by the target area, to favor configurations that cool a bigger surface, and by dividing by the total jet hole area of the 1st channel, which is directly proportional to the total massflow, to favor configurations that use less coolant. The resulting value is non-dimensional and suitable for the comparison of the different configurations.

By considering the findings outlined in the previous chapter, the analysis can be restricted to only certain parts of the channel. First, the Nusselt number distribution in the second channel was found to not depend on the enhancement devices installed in the transition zone, with the exception of the cases with bypasses. The evaluation of the heat transfer capabilities can therefore be restricted to the first channel; of course, if a geometry with a bypass is found to be optimal, this must be taken into account and analyzed further. In the same way, the impingement area of the first channel is generally not affected by the configuration of the transition zone, apart from the last jet in cases where the enhancement devices are installed close to – or upstream of – the stagnation region of the last jet. Therefore an evaluation of the transition zone heat transfer could be sufficient to determine the best performing geometries.

In terms of pressure drop, only the losses between the beginning of the transition zone and the second plenum could be considered, since the discharge coefficient of the impinging jets is similar for all configurations. However, since in some ribbed configurations the first rib is installed upstream of the last jet, some of the losses would not be accounted for if only considering the transition zone and purge hole losses. Therefore the pressure loss of the complete channel is considered for the evaluation. Since experiments have been performed at multiple Reynolds numbers, in order to have a comprehensive evaluation, the data at Re equal to 10,000, 20,000, and 40,000 are averaged to get a single performance value.

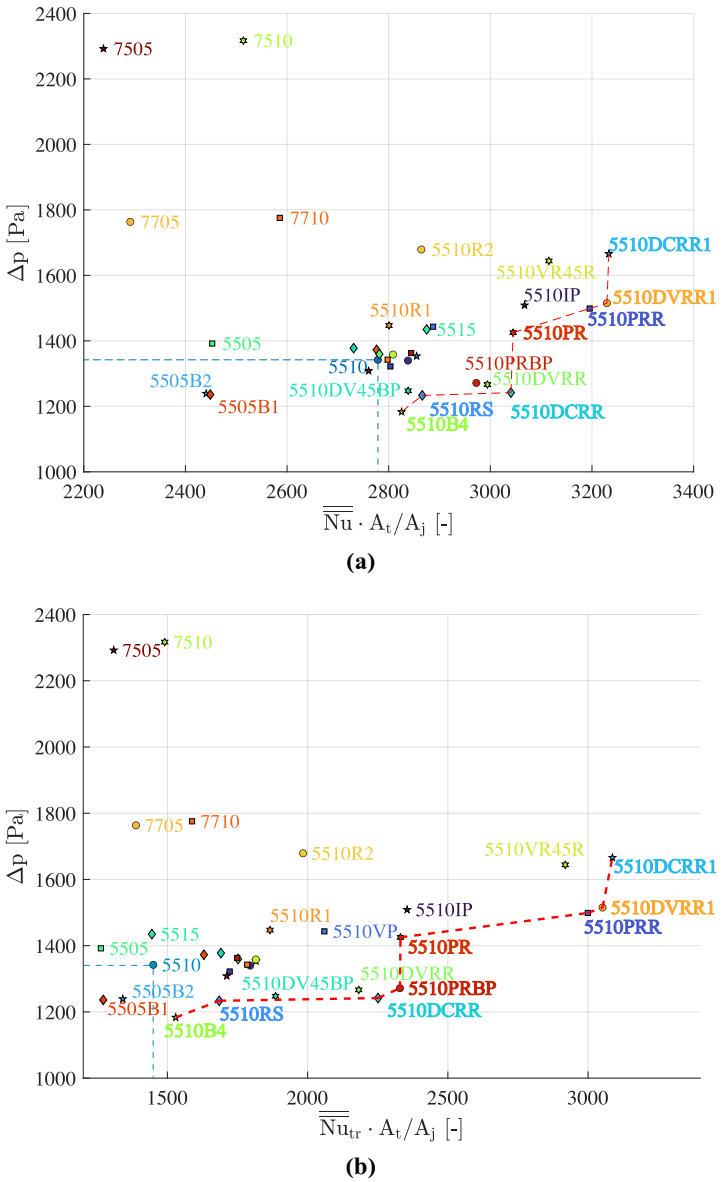

Figure 6.5 – Multi-objective evaluation of the performances of all configurations investigated. The red line represents the Pareto front connecting the optimal configurations, which are marked in bold. The blue dashed line shows the performance of the baseline case. Data are the average of 3 Reynolds numbers. The codenames of the configurations in the graph can be found in Table 3.1 on page 31. Codenames in the central part are not shown for clarity. (a) pressure loss as a function of the "corrected" area-averaged Nu of the 1st channel. (b) pressure loss as a function of the "corrected" area-averaged Nu of the transition zone.

Figure 6.5 shows the channel pressure losses as a function of the area-averaged Nu, corrected as explained above, for all configurations. The labels correspond to the codenames of the geometries which can be found in Table 3.1 on page 31. In the upper graph, the complete first channel is considered for the area-averaged Nu, while in the lower graph, only the transition zone is considered. A hypothetical best configuration would be on the lower right corner of the graphs: low pressure losses and high heat transfer coefficients.

Strictly speaking, the optimal elements in a multi-objective evaluation are the ones that are non-dominated in a Pareto sense. That is, all elements for which a different element with better performances for all objectives cannot be found. In the graphs of Fig. 6.5, the non-dominated configurations are marked in bold and connected with a dashed red curve, which represents the Pareto front for this study. The optimal configurations are essentially the same whether the 1st channel Nu is considered or only the transition zone Nu, confirming the choice of restricting the analysis to the transition zone. The only difference is the presence of the configuration with pin-ribs and bypass in one case but not the other. Since this configuration has much lower average heat transfer in the second channel it was decided to discard it from the optimal solutions.

The configuration with the lowest pressure losses is the one with 4 bypasses (5510B4). For this case, the average Nu in the second channel is lower due to bypassed massflow. However, the reduction is small (less than 2% at Re=40,000 and less than 6% at Re=10,000) so that this solution is interesting if the pressure difference driving the flow is limited. With slightly higher losses, but still lower than the baseline case, the configurations with the small ramp (5510RS) and the discrete chevron ribs with the small ramp (5510DCRR) have very similar pressure losses but the configuration with ribs provides much higher heat transfer. The configuration with pin-ribs exhibits similar average Nu to the discrete chevron ribs with ramp case, but with higher losses and is therefore not very interesting. The next optimal configurations are the pin-ribs with ramp case (5510PRR) and the discrete V-ribs with the big ramp (5510DVRR1); these configurations have similar differences in both pressure and Nu, so both can be considered for further studies. It must be noted that the pin-ribs have a much bigger surface area that can contribute to the heat transfer, so that in practical applications its performance could be on par or better than the ribs case. The configuration with discrete chevron ribs and a big ramp (5510DCRR1) has only slightly better average Nu than the discrete V-ribs with big ramp, but with much higher losses.

In conclusion, by evaluating in a multi-objective way the experimental results some configurations can be selected as optimal and considered for further study:

- 5510B4: configuration with 4 bypass holes between the channels, to minimize the pressure losses.
- 5510DCRR: discrete chevron ribs with small ramp, fairly low losses and high heat transfer.
- 5510PRR: pin-ribs with small ramp, higher Nu with higher losses.
- 5510DVRR1: discrete V-ribs with big ramp, highest Nu with highest losses.

Having identified the optimal configurations, their experimental data can be used to determine the metal temperatures with the procedure used in Section 6.1 for the baseline

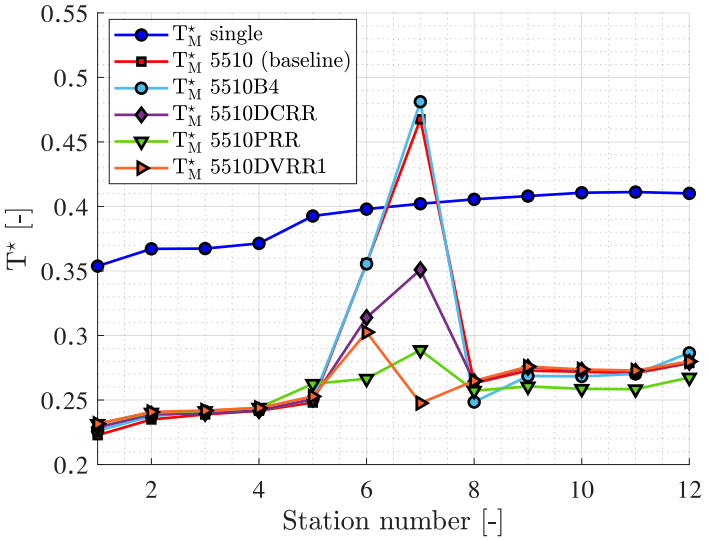

Figure 6.6 – Non-dimensional temperature distribution of the metal along the channel according to the analytical model for a single channel, the baseline sequential channel, and the optimal geometries identified during the analysis.

geometry. The results of this exercise are shown in Fig. 6.6. The geometry with 4 bypass holes (5510B4) does not improve with respect to the baseline in the transition zone. All other optimal configurations show noticeable improvement, and have a maximal temperature lower than the single impingement case. This means that the performance of the gas turbine could be improved by using a sequential impingement configuration instead of a classical one, by either increasing the combustion temperature or reducing the coolant massflow (or a combination thereof) by the amount necessary to bring the metal temperature up to the maximal allowable temperature.

Interestingly, the pin-ribs with ramp configuration (5510DCRR, green line) achieves a very uniform temperature distribution, with only a minor increase in the transition zone (stations 6-7), which is very favorable in terms of the thermal stresses in real operating conditions. It is worth noting how the configuration with discrete V-ribs and big ramp (orange line) achieves low temperature values in the second part of the transition zone (station 7); this is due to the very high Nusselt numbers achieved in that region, which are locally higher than at the stagnation point of the impinging jets.

Of course, for establishing the optimal configuration for deployment in the field, the trade-off between pressure and heat transfer is only part of the equations. Considerations about the feasibility of manufacturing reliably and cost-effectively the parts are also important for obvious reasons. The advent of additive manufacturing allows more freedom in this respect, which must be nevertheless taken into account. Another parameter is the robustness of the cooling solution; for instance very small bypass holes would be prone to clogging if the incoming air is contaminated with particles. These considerations are however out of the scope of this exploratory study, which investigates primarily the thermal performaces of the sequential impingement channels.

6.2.1 Thermal performance

Usually, the performance of a channel featuring heat transfer enhancement devices is evaluated in terms of the thermal performance η_{tp}, which relates the increase in Nusselt number to the increase of friction (Promvonge and Thianpong, 2008):

$$\eta_{tp} = \frac{Nu/Nu_0}{(f/f_0)^{1/3}} \tag{6.6}$$

where Nu is the average Nusselt number of the channel and Nu_0 is the average Nusselt number of a baseline case (smooth channel), possibly found via a correlation (e.g, the Dittus-Boelter equation); f is the friction factor defined as

$$f = \frac{\Delta p}{4\frac{L}{D_H}\frac{1}{2}\rho u^2} \tag{6.7}$$

in which Δp is the pressure loss of the flow over a length L of the channel with hydraulic diameter D_H, and u is the reference velocity. Finally, f_0 is the friction factor of the smooth channel which, again, in some cases could be obtained via a correlation (e.g. Blasius or Filonenko equations, see Incropera et al. (2006)).

Although this approach is commonly used for ribbed channels, it has been also applied to jet impingement flows, for instance by Gritsch et al. (2006) The usefulness of this approach for the channels analyzed in the present study is limited by the fact that the flow is a combination of jet impingement, convection in a smooth or roughened channel and a discharge, which renders the definition of the friction factor ambiguous. Nevertheless, to provide a comparison between the configurations investigated, the thermal performance has been computed by focusing on the transition zone: in Eq. 6.7 the reference length L is the length of the transition zone, u is the average flow velocity in the transition zone (which, for a given Re depends on the number of jets) and Δp is measured from the beginning of the transition zone to the second plenum. Finally, Nu_0 and f_0 refer to the values of the baseline case.

Table 6.1 shows the frictional losses, the heat transfer enhancement, and the thermal performance of all the configurations. The data reported are the average between the 3 Reynolds numbers tested (10,000, 20,000, 40,000), and the configurations are ranked by η_{tp} values. Among the solutions with the highest thermal performance according to this criterion are the pin-ribs configurations, with and without ramp, as well as with the bypass (but with the caveat that the heat transfer in the second channel is lower, which is not considered here) and the ribbed configurations with the small and big ramps. It has to be noted that the configuration with inclined pins fares relatively well for this criterion, whereas in the multi-objective evaluation it was not on the Pareto front. The seven best performing geometries in terms of thermal performance lie on, or near, the Pareto front

channel name	f/f_0	Nu/Nu_0	η_{tp}
5505	1.6140	1.0179	0.8678
7505	1.7369	1.0670	0.8871
5505B1	1.3491	0.9883	0.8945
7705	1.8678	1.1627	0.9441
5505B2	1.3980	1.0617	0.9501
5515	0.6470	0.8568	0.9907
5510R2	1.9814	1.3715	1.0919
7510	0.9497	1.1169	1.1365
5510VPS	0.9860	1.1439	1.1498
5510B4	**0.7880**	**1.0764**	**1.1656**
7710	1.0241	1.1954	1.1861
5510VR45	1.0504	1.2182	1.1971
5510DCR	1.0925	1.2438	1.2076
5510VR45B	1.0356	1.2306	1.2149
5510CR45	1.0125	1.2284	1.2233
5510VR60B	1.0482	1.2469	1.2274
5510BR	1.0034	1.2439	1.2417
5510VR60	1.0877	1.2906	1.2536
5510R1	0.9749	1.2796	1.2901
5510DV60	1.0232	1.3065	1.2955
5510DV45	1.0111	1.3042	1.2987
5510DV45BP	0.8902	1.3554	1.4084
5510VP	1.1283	1.4781	1.4181
5510RS	**0.5460**	**1.1909**	**1.4586**
5510IP	1.3913	1.7055	1.5259
5510VR45R	2.5563	2.0923	1.5285
5510DCRR1	**2.6660**	**2.2243**	**1.6025**
5510PR	**1.0807**	**1.6866**	**1.6440**
5510PRBP	0.9472	1.6707	1.6997
5510DVRR1	**2.1365**	**2.1924**	**1.7003**
5510DVRR	0.7025	1.5717	1.7656
5510PRR	**1.7332**	**2.1680**	**1.8027**
5510DCRR	**0.7046**	**1.6198**	**1.8188**

Table 6.1 – Friction factor, heat transfer enhancement and thermal performance, with respect to the baseline case, for all geometries investigated. Configurations marked in bold are optimal in a Pareto sense according to the multi-objective evaluation of Fig. 6.5.

of the multi-objective evaluation of Fig. 6.5 (configurations marked in bold in Tab. 6.1 are optimal in the multi-objective evaluation). The similarity of the outcome between the multi-objective approach and the thermal performance allows to validate the multi-objective approach against the more commonly used criterion of thermal performance, which for this particular application does not tell the whole story due to the complex flow topology.

6.3 Impact on the thermal efficiency of a gas turbine

In order to estimate the potential of the cooling concept studied in this work, the approach used in Section 6.1 is integrated into a complete cycle of a gas turbine. A cycle based on Ansaldo GT26 gas turbine is considered. The GT26 is a 300MW advanced class gas turbine, which features a so-called sequential combustion strategy, where the first combustion chamber has a very lean mixture, after which the flow is expanded in the high pressure turbine and re-heated in a second combustion chamber. This arrangement is chosen here since it has recently been shown that such a machine can burn mixtures of hydrogen and natural gas, or even pure hydrogen, with only minor modifications (Bothien et al., 2019), and is therefore a good candidate for the evaluation of advanced cooling concepts for turbines that are to be used in a decarbonized electricity grid.

6.3.1 Determination of the thermodynamic cycle

To compute the thermodynamic cycle, publicly available data from Ansaldo and Alstom (the developer of the GT26 turbine, before parts of its gas turbine division where transferred to Ansaldo) have been used. For the missing data, an educated guess has been taken, with minor adjustments to achieve the thermal efficiency and net output power advertised by the manufacturer. The following data and hypotheses are used for the cycle analysis:

- Isentropic losses of η_{sk}=9% in the compressor and η_{st}=7% in the turbines.
- Pressure losses in the combustion chamber: 5%.
- Total massflow $\dot{m}$=650 kg/s.
- Turbine entry temperature (TET, T_{c3}) is 1600 K for the high pressure turbine (HPT) and 1800 K for the low pressure turbine (LPT).
- Overall pressure ratio: $\Pi=\frac{p_{c2}}{p_{c1}}$=34.
- HPT pressure ratio: 0.7
- 20% of the massflow is bypassed for cooling purposes.
- The coolant is used as follows: 12% of the total massflow is used in the LPT (of which 1/3 is used in the 1st stage vanes), 3% in the HPT and 5% is leakage. Coolant use in other components is small and thus neglected.

A representative enthalpy-entropy (h-s) diagram for the cycle of the GT26 machine is shown in Fig. 6.7. The flow is compressed between point 1 and 2, the first combustion chamber brings the flow to the point 3HP, followed by the high pressure turbine (3HP to

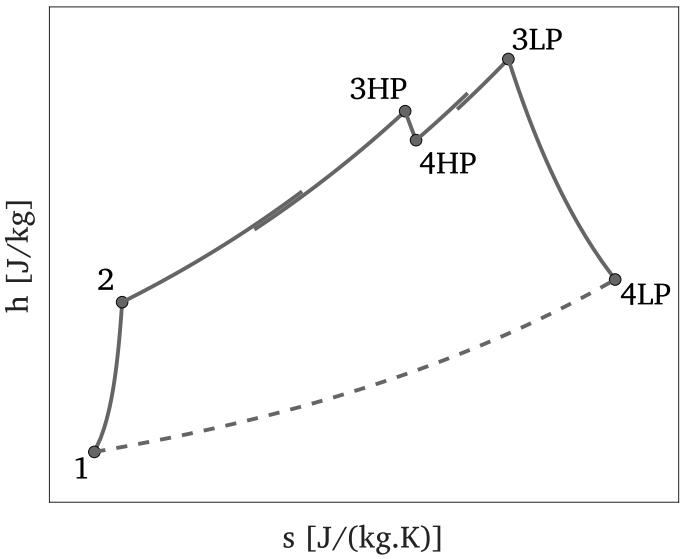

Figure 6.7 – Thermodynamic cycle of the GT26 gas turbine including the losses with the characteristic sequential combustion (segments 3HP-4HP and 3LP-4LP).

4HP), re-heat in a second combustion chamber (4HP to 3LP), and finally the flow passes through the low pressure turbine (3LP to 4LP). The specific work in the different parts of the gas turbine is computed as follows for the compressor and turbines, respectively:

$$e_k = \frac{1}{\eta_{sk}} c_{pk} T_{c1} \left[\left(\frac{p_{c2}}{p_{c1}} \right)^{(\kappa_k - 1)/\kappa_k} - 1 \right] \tag{6.8}$$

$$e_t = \eta_{st} c_{pt} T_{c3} \left[\left(\frac{p_{c4}}{p_{c3}} \right)^{(\kappa_t - 1)/\kappa_t} - 1 \right] \tag{6.9}$$

in which c_p is the specific heat capacity at constant pressure, $\eta_s$is the isentropic efficiency, and κ is the heat capacity ratio – assumed to be 1.4 for the compressor (air) and 1.3 for the turbine (combustion gases). The subscript c denotes the total pressure or total temperature, the subscripts k and t refer to the compressor and turbine, respectively, and the numbered subscripts correspond to the numbers in the cycle of Fig. 6.7.

The specific heat input required to raise the temperature of the flow in the combustion chamber is given by:

$$q_{in} = \frac{c_{pt} + c_{pk}}{2} \left(T_{c3} - T_{c2} \right) \tag{6.10}$$

in which it is assumed that the flow changes its heat capacity linearly with temperature from c_{pk} to c_{pt}.

To find the output power of the machine and its thermal efficiency, the specific values are not enough if the effect of the coolant massflow has to be taken into account. Indeed, since the coolant is bypassed from the compressor, it does not flow through the combustion chamber and does not need to be heated. The coolant is reintroduced in the turbine (via

film cooling) and some assumptions are required to determine its contribution to the work done in the turbines. The following simplifying hypotheses are made:

- The coolant in the HPT contributes to the work done in the LPT but not in the HPT.
- The coolant in the LPT does not contribute to the turbine work at all.
- The leakage flows do not produce any work on the turbine.
- The coolant injection does not alter the gas properties of the core flow of the turbine.

Additionally, to simplify the calculations, the massflow of the fuel is not considered for the massflow of the turbine. With these assumptions, the power generated or absorbed by each component of the machine can be computed simply by multiplying the specific work e_k, e_t and the specific heat input q_{in} by the respective massflows.

The useful power $\dot{E}_u$ can be found by subtracting the power required by the compressor from the power generated by the turbines. The thermal efficiency η_{th} follows directly from this and is defined as the ratio of the useful power $\dot{E}_u$ to the heat input rate $\dot{Q}$ in the combustion chambers.

For the cycle considered and the above mentioned assumptions, a thermal efficiency of 41.00% is found, with a useful power of 282.6 MW.

6.3.2 Effect of the integration of the sequential cooling

To estimate the benefits of using a sequential impingement channel in the GT26 gas turbine, all the impingement channels in the stator vanes of the first stage of the LPT are changed from single impingement channels like the one analyzed in Section 6.1 to the optimal sequential channels identified in Section 6.2.

The coolant massflow needed to have the same metal temperature as for the single impingement case is found using the approach of Section 6.1, for the optimal sequential impingement channels identified previously. With the new coolant massflow, the efficiency of the machine can then be computed with the same approach as in Section 6.3.1.

Table 6.2 reports the results of the thermodynamic cycle computation integrating the coolant massflow reduction enabled by the better performing cooling configurations. The thermal efficiency can be increased from 41.00% to 41.29% in the case of the pin-ribs with the ramp. This represents a relative improvement of the thermal efficiency of 0.71%, which is highly significant for a mature technology like a gas turbine. The discrete V-ribs with the big ramp achieve almost the same performance, while the discrete chevron ribs with the small ramp show smaller improvement (+0.39%, efficiency 41.16%) but with lower pressure losses.

channel name	impingement coolant reduction [%]	total coolant reduction [%]	$\dot{E}_u$ [MW]	η_{th} [%]
single impingement	-	-	282.6	41.00
5510DCRR	29.36	5.87	284.5	41.16
5510PRR	52.14	10.43	286.0	41.29
5510DVRR1	47.68	9.54	285.7	41.26

Table 6.2 – GT26 gas turbine performances with the optimal sequential impingement channels.

In the present analysis, the coolant massflow has been reduced to achieve the same maximum metal temperature as in the single impingement case, while keeping the turbine entry temperature (TET) constant. Alternatively, TET could have been increased while keeping the coolant massflow constant, provided that that the parts which are cooled with other methods than impingement do not exceed the maximum allowable temperature. In practice, a combination of reduction of coolant massflow and increase of TET is needed to achieve optimal performances.

The choice of the channel type between the ones identified as optimal depends also on the pressure difference available to drive the flow. If the pressure losses at the required Reynolds number are higher than the available pressure difference, the coolant massflow would be lower than expected, leading to lower thermal performances. In this case it could be better to opt for a configuration with lower losses (e.g. the channel 5510DCRR identified above). This should not be the case though, since multi-pass roughened channels, which are commonly used for rotor blade cooling, have higher pressure drop than impingement. In any case, the combustor configuration of the GT26 machine analyzed here is very favorable for the inclusion of the sequential channels, since the sequential impingement concept could be used only after the second combustor, like in the present analysis, where the pressure is lower and there is ample margin with respect to the pressure differential between inlet and outlet of the cooling channels.

From a manufacturing point of view, the use of a sequential impingement channel complexifies the production of the blade via advanced casting, due to the inclusion of the second plenum. However, with the move to additive manufacturing in the foreseeable future, at least for the static parts, this point is of little importance.

In the results of Table 6.2, it can be noticed that the power delivered by the machine is also increasing when using the sequential channels. This is due to the fact that more massflow is going through the combustion chamber; this means that more fuel massflow is consumed, but this is more than counterbalanced by the increased work extracted from the flow in the turbine. This additional power density is an important factor for jet engines, where the thrust-to-weight ratio of the engine is a fundamental parameter to be taken into account for optimizing the overall efficiency of the aircraft. Indeed, in aircraft design, changes in the weight of a component cause a cascading effect on the design of other parts. In this instance, reducing the engine weight reduces the maximum lift required, which

enables the designer to reduce the wing surface area, thus reducing the drag of the plane, and with it, the required power of the engines, creating a feedback loop enabling much more savings than for the engine alone. In the same way, the weight reduction enables the use of a lighter landing gear, creating another feedback loop of weight reduction.

Chapter 7

Conclusions and outlook

In this chapter, the main findings are summarized. An outlook of the open points and recommendations on the directions in which to focus the future research in this topic are given in Section 7.2.

7.1 Conclusions

Narrow impingement channels achieve very high heat removal from the external wall of the turbine blades, especially in modern, integrally cast blades, in which complex channels can be integrated in the external wall. The reduction of the thickness of the external wall allows a further increase of the heat transfer. However, if the number of jets in the impingement channel is relatively high, the crossflow of the spent air interacts with the most downstream jets, reducing the achievable heat transfer coefficient in the aft part of the channel. In order to minimize this negative effect, several modifications of the channel geometry have been proposed in the literature, which achieved minor improvements (see the literature review in Chapter 2). In the present study, a more radical solution has been explored, which consists of separating a long channel in two parts, in which the spent air of the first channel is discharged in an additional plenum to be re-used in the second. By doing so, the crossflow is "reset" and the impinging flow in the second channel has similar topology as the first, albeit with a reduction in heat transfer performances due by the higher temperature of the cooling air.

No previous studies regarding this type of sequential channels were available in the scientific literature at the beginning of this project, and therefore, the main achievement of this thesis is the determination of the performances of sequential impingement channels. The analysis has relied mainly on experiments, since numerical simulations of impinging jets using conventional RANS techniques still lack the required accuracy in terms of heat transfer coefficient prediction, especially at and near the stagnation point of the jets where the Nusselt number is generally overestimated by as much as 20%. In order to tackle the sequential geometries, a new experimental technique has been developed. Indeed, the

commonly used transient liquid crystal thermography technique, which relies on a step change in the flow temperature to drive the experiment, is not suited to the sequential channels, especially those that feature a bypass flow between the channels: using the conventional technique, a three temperature problem needs to be solved, which would highly complicate the experimental procedure and reduce the accuracy of the results.

In light of this, the main achievements of this thesis may be summarized as follows:

- *The experimental investigation of sequential narrow impingement channels, the detailed analysis of their performances, and the determination of the critical points.*
- *The mitigation of the identified critical points, namely the low heat transfer region in the transition zone, by channel modifications to locally increase the Nusselt number.*
- *The estimation of the possible gains in terms of efficiency of the complete gas turbine by the inclusion of sequential impingement channels in the internal cooling system of the hot parts of the turbine.*
- *The development of a transient measurement technique based on a time-varying surface heat flux suitable for the experimental investigation of the sequential channels.*

Experiments have been performed on a scaled-up geometry to allow for a high resolution of the results on the target plates, as well as to avoid any compressibility effects. The channels selected have a relatively simple geometry compared to the channels installed in a real turbine blade, and consist on a rectangular section and planar target plate. This allows the determination of the main characteristics of the sequential channels. The flow conditions have been selected to achieve a jet Reynolds number in the range 10,000-40,000, which is comparable to the impingement cooling flows achieved in a real gas turbine cooling system. This allows direct use of the obtained experimental data for the design of the gas turbine internal cooling system and for its performance estimation. The experimental results also give some insight into a couple of peculiar aspects of the investigated geometries which have not been researched previously. The use of ribs or pins to augment the effect of impingement has been extensively investigated in the literature, but usually the enhancement features are installed in the proximity of the impingement zone of the jets; in the present research the enhancement features are installed downstream of the impingement area in the transition zone. This is similar to a classical ribbed channel, but the incoming flow is different since it is influenced by the wall-jet flow of the last impinging jet and the vortical structures generated by the interaction between the crossflow and the jets. Additionally, the discharge of the first channel is located on the surface opposite the target plate; literature studies generally consider that the flow exits the channel in a direction parallel to the crossflow.

7.1.1 Main findings

The new experimental technique was validated against literature data on a testcase consisting of a single jet impinging on a flat surface. The accuracy and repeatability of the new technique are in line or superior than state of the art transient techniques based on a step change in the flow temperature, with the new method achieving an accuracy of between 6% and 9% depending on the location on the plate.

Test results on the baseline case showed that the basic concept of the sequential impingement is sound. The Nusselt number levels in the second channel are similar in magnitude to the first. It must be noted, however, that the reference temperature for the derivation of the Nusselt number is based on the jet velocity, so that the heat pickup in the first channel is not taken into account. The actual performances will depend on the external heat load distribution. The distribution of the peak Nu values at the jet stagnation points differs slightly between the channels and this can be attributed to the different massflows of the individual jets caused by the differing feeding mechanism: an ideal plenum, at constant pressure, for the first channel; a flow discharging from the first channel into the second plenum, for the second channel, which results in a pressure variation in the streamwise direction. The discharge coefficient of the impingement holes is higher than what is usually found for round jets: this is achieved by chamfering the edges of the holes. To discharge the flow into the second plenum, an obround hole has been selected. Its high surface area allows for low pressure losses, in absolute terms, compared to the impingement part of the channel. Its discharge coefficient, however, is relatively low, mainly due to the fact that a sharp edge causes a detachment of the discharge flow. The addition of a rounded corner for some cases with a cross-section reduction allows to reduce these aerodynamic losses.

An analytical evaluation of the performances of the baseline channel in a real case scenario highlighted the need to increase the heat transfer coefficient in the transition zone, which is not cooled by impingement but only by the convection of the crossflow. The use of ribs allowed a moderate increase of the average Nusselt number of approximately 20% with a negligible increase of the pressure losses. The enhancement is higher, in relative terms, for the low Reynolds number case (Re=10,000). This holds true for all enhancement features. Discrete ribs provide marginally more improvement than the conventional counterpart. Pins, due to their higher blockage, pay a penalty in terms of pressure losses, but still marginal with respect to the overall pressure drop of the channel. The gains in terms of heat transfer capabilities in the transition zone is higher than in the case of ribs, showing 50% higher values than the smooth channel, and can reach 100% improvement in the case of inclined pins at low Reynolds number. Reducing the cross-section of the channel in the transition zone to achieve higher flow velocity increases the heat transfer by 10% to 40%, depending on the amount of reduction of the channel height and the type of the ramp insert. By carefully designing the ramp profile, especially the rounded corner upstream of the purge hole, the pressure losses can be decreased compared to the baseline by reducing the detachment of the discharge flow. The addition of a bypass to let some of the crossflow

of the first channel pass in the second impingement channel without going through the intermediate plenum allows to reduce the overall pressure losses. The jet flow caused by the bypass, which is located near the target plate, increases the local Nusselt number in the most upstream part of the second channel. The reduction of the massflow going through the impingement holes of the second channel, however, reduces the area-averaged Nu of the second channel. The reduction is less important when the number of bypass holes is increased (keeping the total bypass hole area constant). However, the size of the bypass holes cannot be reduced indefinitely, since at real scale, the bypass holes would become so small as to be difficult to manufacture and prone to clogging. If the bypass hole is in the centerline of the channel, the interaction with the first jet of the second channel reduces the Nusselt number at the jet stagnation.

By compounding several of the aforementioned enhancement features, the performances of the impingement channel can be further improved. In the last experimental campaign, configurations with both pins and ribs, both pins and ramps, and even pins with ribs and ramps have been investigated. These configurations are found to be optimal or near the optimum in a multi-objective evaluation, confirming the potential of compounding more enhancement devices, with the discrete ribs with a big cross-section reduction and the pin-ribs with ramp achieving the highest heat transfer in the transition zone, while the discrete ribs with the small cross-section reduction achieve a combination of relatively high heat transfer and low losses. The addition of a bypass can reduce the overall pressure losses, with an impact on the average Nusselt number in the second channel due to the lower jet velocity caused by the reduction of the massflow that passes through the second plenum.

The published experimental results could prove useful for the design of novel cooling arrangements for turbine blades, vanes and for the casing. Some findings will prove useful during the detailed design phase and will depend on the specific case, for example the possibility of adding bypass holes if the pressure difference available to drive the flow is not sufficient to achieve the required velocity. The wide variety of cooling solutions reported in this work allows for the optimal choice of the channel configuration according to the boundary conditions of the specific case: available pressure drop and external heat flux distribution. Additionally, the data presented in this work could be used to improve and validate qualitatively and quantitatively the numerical tools for complex flow situations that combine impinging flows, obstacles in the wall-jet region and discharge into a second plenum that needs resolution of a free shear layer.

An analytical heat transfer problem using conditions similar to what is commonly found in a first stage stator vane has been performed to estimate the temperature distribution of a part actively cooled by a sequential impingement channel. This showed the need to increase the heat transfer in the transition zone. The optimal geometries can achieve a relatively uniform temperature distribution, which is favorable for the minimization of the thermal stresses. In particular, the pin-ribs with ramp configuration exhibits a small temperature increase in the downstream direction with small gradient and a maximum temperature in the second part of the transition zone slightly higher than the average

temperature. The identified optimal configurations achieve lower metal temperatures than the single narrow impingement channel with the same coolant massflow.

The potential improvement of the thermal efficiency of a gas turbine has been estimated by computing the thermodynamic cycle of a machine and by varying the coolant massflow with the constraint of keeping the same maximum metal temperature as when using a traditional narrow impingement channel. This analysis showed that two of the optimal configurations – the discrete V-ribs with a big ramp and the pin-ribs with a small ramp – achieve a potential improvement of almost 0.7% (from 41.00% to 41.29%) in terms of thermal efficiency of the engine. At the same time, the total power of the machine is increased by using more of the flow in the hot gas path.

The efficiency improvements enabled by this novel cooling arrangement are important for future gas turbines, which are planned to be used in a power storage scheme, in which synthetic gas or hydrogen are produced in times of excess electricity production to be later used in gas turbines to meet the peak demand. On the one hand it is important to maximize the efficiency of the conversion from electricity and back, and on the other hand, a more performing cooling system is required to cope with the specific challenges of burning hydrogen in a gas turbine: higher flame speed, higher adiabatic flame temperature, and higher heat transfer coefficients due to the different composition of the combustion products.

7.2 Recommendations for future investigations

The present work investigated the concept of sequential impingement channels in an exploratory way on simplified geometries, consisting of a rectangular channel cross-section and an obround purge hole. A wide range of different enhancement devices has been tested, in order to find the most adapted to the problematic. In the future, a more detailed analysis should be undertaken, using the most promising enhancement features, on a channel configuration that is closer to the real case scenario. In particular, if the channel is installed in a vane, the airfoil curvature should be taken into account, since for example the coolant flow could detach from the target plate in the transition zone on a convex surface; similarly, the discharge into the purge hole would exhibit lower losses if the surface is concave. State-of-the-art cooling solutions include impingement cooling, convective cooling and film cooling, this raises the question of how to integrate film cooling holes in the sequential channels. The critical point is how to place the ejection holes, and how this affects the cooling capacity of the channel downstream of these holes. Indeed, if a substantial part of the massflow is ejected, the thermal performances of the second channel would be impacted. Therefore, future studies should focus on the complete system including film cooling and/or effusion cooling.

Pins and ribs increase the available area for the heat exchange and contribute to the overall heat transfer. This study only considered their contribution to the heat transfer of the

target plate due to the flow mixing caused by increased turbulence and vortical flow. The performance evaluation is thus conservative with respect to the contribution of the enhancement features. Future studies should consider the full contribution of pins and ribs to assess more accurately the potential of the sequential impingement channels.

The present study showed that the pressure losses of the complete channel are higher than for the single impingement channel. Although the losses associated with the two impingement passages do not have the potential for significant further reductions, the discharge into the second plenum can be improved. Future studies should focus on these pressure losses, by varying the surface area and shape of the purge hole. This could be performed with the use of numerical tools and a shape optimization framework. In the same spirit, the shape of the enhancing features identified here (pins, ribs, ramps) have a potential for optimization using state-of-the-art techniques, for instance using CFD coupled with an adjoint approach (Brezillon and Gauger, 2004), or by using surrogate models based on a kriging interpolation method (Xing et al., 2020) or on convolutional neural networks (Bardi, 2019; Sun and Wang, 2019). Future work should focus on multi-objective optimizations, by considering both the heat transfer enhancement and the pressure losses. To accomplish the numerical optimization effectively, further research in the field of turbulence modeling is needed, in order to be able to predict with the necessary accuracy the heat transfer coefficients near the stagnation points of the impinging jets when using a RANS approach. Of course, large eddy simulations (LES) achieve adequate results, but the high computational cost makes it a non starter for an actual optimization framework considering today's computational power.

Appendix A

Derivation of the semi-infinite model

The one-dimensional heat conduction equation reads:

$$\frac{\partial^2 T(z,t)}{\partial z^2} = \frac{1}{\alpha}\frac{\partial T(z,t)}{\partial t} \tag{A.1}$$

The following initial and boundary conditions are considered: the solid is initially at ambient temperature:

$$T(z, t = 0) = T_i \tag{A.2}$$

At the fluid-solid interface (z=0), a surface heat flux, linearly increasing in time, is applied, which is convected into the flow and conducted into the solid:

$$-k\frac{\partial T(z=0,t)}{\partial z} - h[T_{aw} - T(z=0,t)] = q_0 t \tag{A.3}$$

In the general case in which the jet temperature is not at the same temperature as the ambient ($T_g \neq T_i$), the entrainment effect needs to be considered. Using the definition of Goldstein et al. (1990), the entrainment effect is defined as:

$$\eta_e = \frac{T_{aw} - T_r}{T_g - T_i} \tag{A.4}$$

where T_r is the recovery temperature. Assuming a recovery factor of $r = 1$ as in Baughn et al. (1991) and small Ma numbers, T_r in Eq. A.4 can be assumed to be equal to T_i.

Combining Eq. A.3 and A.4, and rearranging:

$$-k\frac{\partial T(z=0,t)}{\partial z} + h(T(z=0,t)) - q_0 t = hT_i - \eta_e h[T_i - T_g] \tag{A.5}$$

For the second boundary condition, the plate is considered semi-infinite:

$$T(z \to \infty, t) = T_i \tag{A.6}$$

To solve Eq. A.1 one can move to the Laplace space. Equation A.1 in Laplace space reads:

$$\frac{\partial^2 \overline{T}}{\partial x^2} - \frac{1}{\alpha} s \overline{T} = -\frac{1}{\alpha} T_i \tag{A.7}$$

and the boundary condition A.3:

$$-k \frac{\partial \overline{T}(0, s > 0)}{\partial z} + h(\overline{T}(0, s)) - \frac{q_0}{s^2} = \frac{h T_i}{s} - \frac{\eta_e h [T_i - T_g]}{s} \tag{A.8}$$

in which the bar indicates the Laplace transform of the function.

The general solution of Eq. A.7 is the sum of the general solution of the homogeneous portion of the equation and a particular solution of the non-homogeneous problem:

$$\overline{T} = \overline{T}_H + \overline{T}_{NH} = C_1 \mathrm{e}^{\sqrt{\frac{s}{\alpha}} z} + C_2 \mathrm{e}^{-\sqrt{\frac{s}{\alpha}} z} + \frac{T_i}{s} \tag{A.9}$$

where T_i/s is a solution of the non-homogeneous problem. The constant C_1 must be 0, because T, and thus $\overline{T}$, must be bounded as $x \to \infty$. The constant C_2 can be determined by noting that Eq. A.9 has to fulfill the boundary condition A.8.

$$C_2 = \frac{\frac{h}{k}(T_i - \eta_e (T_i - T_g) - T_i)}{s(\sqrt{\frac{s}{\alpha}} + \frac{h}{k})} + \frac{q_0/k}{s^2(\sqrt{\frac{s}{\alpha}} + \frac{h}{k})} \tag{A.10}$$

which, inserted into A.9, gives the solution in Laplace space:

$$\overline{T} = \frac{-\frac{h}{k} \eta_e (T_i - T_g)}{s(\sqrt{\frac{s}{\alpha}} + \frac{h}{k})} \mathrm{e}^{-\sqrt{\frac{s}{\alpha}} z} + \frac{q_0/k}{s^2(\sqrt{\frac{s}{\alpha}} + \frac{h}{k})} \mathrm{e}^{-\sqrt{\frac{s}{\alpha}} z} + \frac{T_i}{s} \tag{A.11}$$

To obtain the solution in the temporal space, the inverse transform of each one of the three terms on the right hand side of Eq. A.11, (T_1, T_2, and T_3 in the following) must be found. For better overview, in the following the terms $a = \frac{z}{2\sqrt{\alpha t}}$, $b = \frac{hz}{k} + \alpha t \frac{h^2}{k^2}$, and $c = \frac{h}{k}\sqrt{\alpha t}$ are used.

The first term corresponds to the convection due to the difference between the flow temperature and the initial plate temperature. The inverse Laplace transform is obtained from Carslaw and Jaeger (1959, p. 72) and reads:

$$T_1(z, t) = -\eta_e (T_i - T_g) \left[\mathrm{erfc}\,(a) - \mathrm{e}^b \mathrm{erfc}(a + c) \right] \tag{A.12}$$

The second term corresponds to the effect of the applied heat flux. The inverse transform can be found using expression 16 in Carslaw and Jaeger (1959, Appendix 5). To obtain an expression equivalent to the referenced work, one can perform the substitution $g = \sqrt{\frac{s}{\alpha}}$:

$$\overline{T}_2(z,s) = \frac{\frac{q_0}{k/\alpha^2} e^{gz}}{g^4\left(g + \frac{h}{k}\right)} \tag{A.13}$$

The inverse Laplace transform of A.13 reads

$$T_2(z,t) = \frac{q_0}{k\alpha^2}\left[\frac{\alpha}{(-\frac{h}{k})^3} e^b \operatorname{erfc}\{a+c\} - \frac{\alpha}{(-\frac{h}{k})^3}\sum_{r=0}^{2}(-2c)^r\, i^r \operatorname{erfc}\{a\}\right] \tag{A.14}$$

Term three is simply the initial temperature, and the inverse transform is straightforward:

$$T_3(z,t) = T_i \tag{A.15}$$

Combining Eq. A.12, A.14 and A.15 leads to the final solution:

$$\begin{aligned} T(z,t) - T_i = &- \eta_e (T_i - T_g)\left[\operatorname{erfc}(a) - e^b \operatorname{erfc}(a+c)\right] + \\ &+ \frac{q_0}{k\alpha^2}\left[\frac{\alpha}{(-\frac{h}{k})^3} e^b \operatorname{erfc}(a+c) - \frac{\alpha}{(-\frac{h}{k})^3}\sum_{r=0}^{2}(-2c)^r\, i^r \operatorname{erfc}(a)\right] \end{aligned} \tag{A.16}$$

In Eq. A.14 and A.16, the term $i^r \operatorname{erfc}(a)$ denotes the r$^{\text{th}}$ successive integration of the complementary error function, which can be defined iteratively as follows (see Carslaw and Jaeger, 1959, Appendix 2):

$$i^n \operatorname{erfc}(x) = \int_x^\infty i^{n-1} \operatorname{erfc}(\xi)\, d\xi \tag{A.17}$$

$$i^0 \operatorname{erfc}(x) = \operatorname{erfc}(x) \tag{A.18}$$

For values of n equal to 1 and 2, Eq. A.17 can be solved by integrating by parts, leading to the following expressions:

$$i^1 \operatorname{erfc}(x) = \frac{1}{\sqrt{\pi}} \exp(-x^2) - x \operatorname{erfc}(x) \tag{A.19}$$

$$i^2 \operatorname{erfc}(x) = \frac{1}{4}\left[\operatorname{erfc}(x) - 2x(i^1 \operatorname{erfc}(x))\right] \tag{A.20}$$

For the particular case in which the flow is at ambient temperature, T_g=T_i, Eq. A.16 becomes:

$$T(z,t) = T_i + \frac{q_0}{k\alpha^2}\left[\frac{\alpha}{(-\frac{h}{k})^3}\mathrm{e}^b\mathrm{erfc}(a+c) - \frac{\alpha}{(-\frac{h}{k})^3}\sum_{r=0}^{2}(-2c)^r\, i^r\mathrm{erfc}(a)\right] \tag{A.21}$$

Appendix B

Nusselt number correlation for a jet impinging on a flat surface

With the data obtained during the validation of the experimental method (see Section 4.4), the correlation of Goldstein and Franchett (1988), which covers only specific jet-to-plate distances, can be extended to arbitrary distances in the interval $4 \leq Z/D \leq 10$ for a jet perpendicularly impinging a surface.

For normal jets, the referenced correlation takes the form:

$$\frac{Nu}{Re^{0.7}} = A \exp\left(-0.37(r/D)^{0.75}\right) \tag{B.1}$$

The parameter A depends on the jet-to-plate distance Z/D, and is defined only at 3 distances. To extend the correlation to arbitrary Z/D , Eq. B.1 is fitted to the data; in this way, the value A that best fits the data is obtained for each experiment. A quadratic function of Z/D provides a good fit of the parameter A for the available data:

$$A = -0.0012(Z/D)^2 + 0.012(Z/D) + 0.1267 \tag{B.2}$$

Table B.1 shows a comparison of the value of parameter A found using Eq. B.2 with the values given in Goldstein and Franchett (1988); there is a good agreement at these distances. Goldstein and Franchett predict slightly higher values at Z/D=4 than at Z/D=6, while Eq. B.2 predicts the same level at both distances, with a maximum at Z/D=5. Nusselt number levels, however, are almost constant for Z/D in the range $[4, 6]$, as is also noted in Goldstein and Franchett (1988). One can thus conclude that the extension of the correlation proposed here is consistent with the original formulation for the case of jets impinging normally to a flat surface.

Z/D	A (present work)	A (Goldstein and Franchett)
4	0.156	0.159
6	0.156	0.155
10	0.127	0.123

Table B.1 – Values of parameter A predicted by Eq. B.2 and by Goldstein and Franchett (1988).

The extended form of the correlation reads:

$$\frac{Nu}{Re^{0.7}} = \left(-0.0012(Z/D)^2 + 0.012(Z/D) + 0.1267\right) \exp\left(-0.37(r/D)^{0.75}\right) \qquad \text{(B.3)}$$

Appendix C

CFD analysis

For exploring some details of the flow field, especially the discharge flow into the purge hole and the effect of ramps, supporting CFD computations have been performed. The simulations have been run using the open source tool SU2 (Economon et al., 2016), using unstructured meshes with prism layers at the wall to fully resolve the boundary layer with $y+$ values lower than 1. The low-Mach Navier-Stokes equations (Müller, 1998), closed with Menter's k-ω shear stress transport (SST) turbulence model (Menter, 1994), are solved using a finite volume scheme. The low-Mach approximation allows to model the flow as incompressible, thus avoiding the convergence problems of the compressible Navier-Stokes equations at low Mach number, while allowing for variations in density, which is an important point for flow simulations in which heat transfer plays a role. In practice the density is determined from a state equation which depends on the transported quantities , i.e. temperature and pressure (Economon, 2018). The convective fluxes are solved using a central 2^{nd} order scheme and the viscous fluxes with a 1^{st} order upwind scheme. The solution is advanced in time using an Euler implicit scheme, and a V-type multigrid strategy is used to accelerate the convergence.

The baseline geometry has been chosen for the validation. Three meshes with different refinements have been generated to perform a mesh study at Re=20,000. The iterative process converges steadily after a transient phase in which the solver adapts the inlet pressure to conform to the specified inlet velocity (Fig.C.1).

Figure C.2 shows the in-plane velocity vectors superposed to traces created with the line integer convolution filter of the visualization tool Paraview. The main features of the flow are apparent: the pattern of the horseshoe vortices upstream of the jets, the vortical features spanning the complete channel height, and the discharge flow. The physics seems correctly captured. Figure C.3 shows the Nusselt number pattern on both target plates. The values at the stagnation point are highly overestimated, as can be judged from Fig. C.4, which compares the streamwise-averaged data with the experiments. Refining the meshes reduces the discrepancy, but it is still in the order of 40% at the stagnation. In the wall jet region the values are very similar to the experiments, so the issue of the

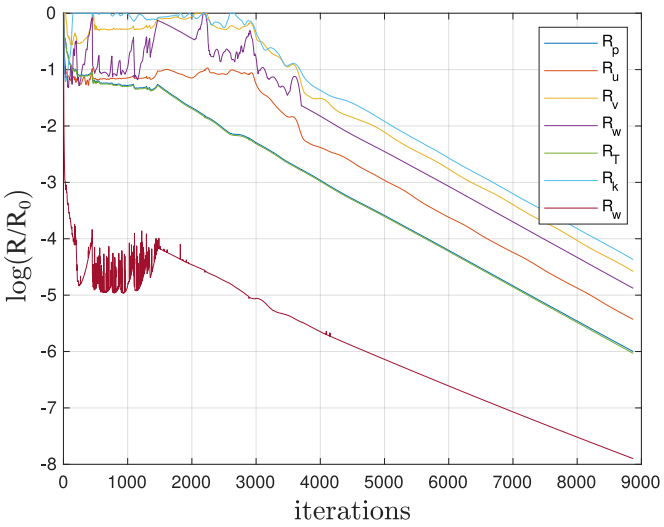

Figure C.1 – Convergence of the relative residuals.

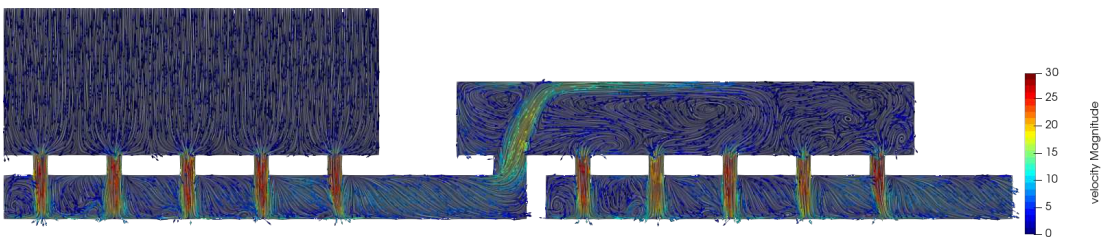

Figure C.2 – In-plane velocity vectors and line integral convolution in the central plane for the fine mesh at Re=20,000.

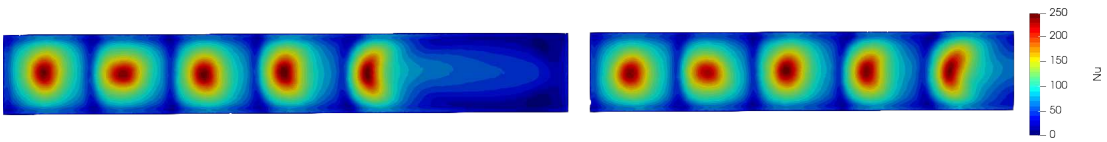

Figure C.3 – Nusselt number distribution on the target plates for the fine mesh at Re=20,000.

prediction of the heat transfer coefficient with the RANS methodology is limited to the jet flow, consistently with literature findings.

The jet holes where not chamfered in the numerical modeling, to avoid the very small surface elements that are needed to resolve such small features. For this reason the discharge coefficient of the jets is found to be lower than in the experiments, approximately 0.7 and slightly lower than literature data for this configuration (approximately 0.75). The analysis focuses on the purge hole data by measuring the pressure difference between the beginning of the transition zone and the second plenum. While the experiments rely on pressure data at the surface, in the CFD the pressure is computed as the area-average of the cross-section. Table C.1 shows the pressure difference at Re=20,000 and the comparison

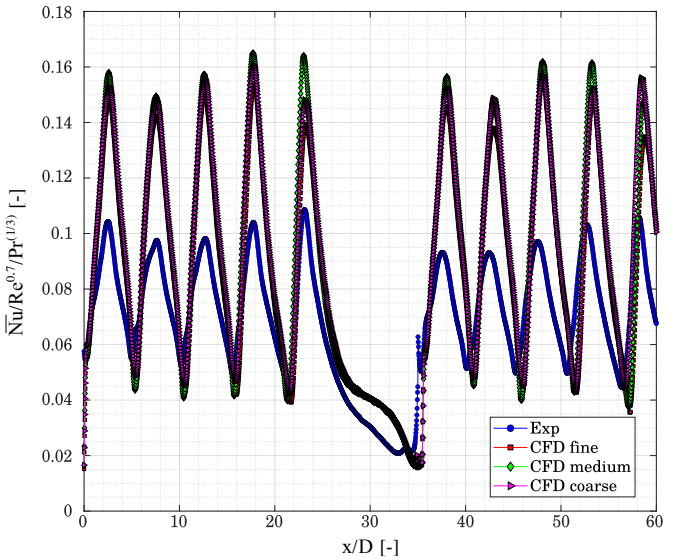

Figure C.4 – Spanwise-averaged, normalized Nusselt number at Re=20,000 for the 3 meshes and comparison with the experimental data.

coarse grid	medium grid	fine grid	experiment
142 *Pa*	146 *Pa*	153 *Pa*	140 *Pa*

Table C.1 – Pressure loss of the transition zone and discharge hole for the 3 CFD meshes and the experiments.

with the experimental data. The values are in line with the experiments and this hints at a correct simulation of the main flow features in this region, namely the detachment in the purge hole and the shear flow in the second plenum.

Since the support simulations are performed for the analysis of the transition zone flow and for the discharge in the purge hole, the present CFD procedure can be considered valid in this regard. However, CFD results should not be used to predict the Nusselt number at the jet stagnation point, since the relative error is high.

Appendix D

Picture of the test rig

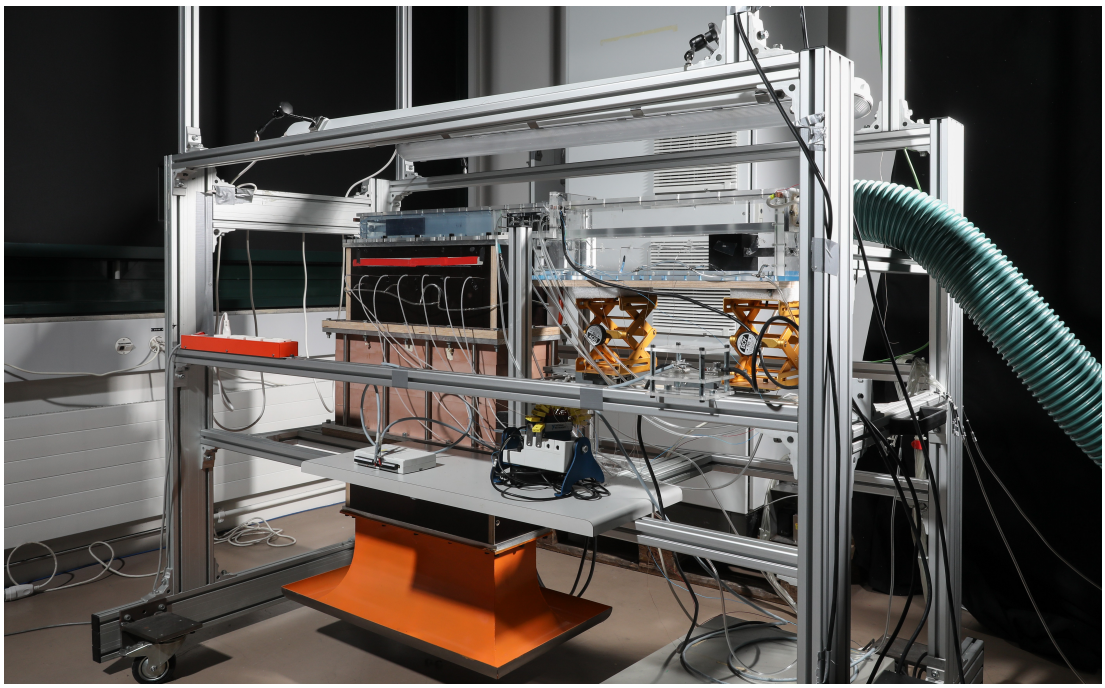

Figure D.1 – Impingement heat transfer test facility. ©*Alain Herzog*

Bibliography

Al-aqal, O. M. (2003). *Heat transfer distributions on the walls of a narrow channel with jet impingement and cross flow*. PhD thesis, University of Pittsburgh.

Ansu, U., Godi, S. C., Pattamatta, A., and Balaji, C. (2017). Experimental investigation of the inlet condition on jet impingement heat transfer using liquid crystal thermography. *Experimental Thermal and Fluid Science*, 80:363–375.

Ay, H., Jang, J., and Yeh, J.-N. (2002). Local heat transfer measurements of plate finned-tube heat exchangers by infrared thermography. *International Journal of Heat and Mass Transfer*, 45(20):4069–4078.

Bailey, J. C. and Bunker, R. S. (2002). Local heat transfer and flow distributions for impinging jet arrays of dense and sparse extent. volume 3 of *Turbo Expo: Power for Land, Sea, and Air*, pages 855–864.

Ballal, D. R. and Zelina, J. (2004). Progress in aeroengine technology (1939–2003). *Journal of Aircraft*, 41(1):43–50.

Bardi, F. (2019). Aerodynamic shape optimization via surrogate modelling with convolutional neural networks. Master's thesis, EPFL, Lausanne, Switzerland.

Baughn, J. W., Hechanova, A. E., and Yan, X. (1991). An experimental study of entrainment effects on the heat transfer from a flat surface to a heated circular impinging jet. *Journal of Heat Transfer*, 113(4):1023–1025.

Baughn, J. W. and Shimizu, S. (1989). Heat transfer measurements from a surface with uniform heat flux and an impinging jet. *Journal of Heat Transfer*, 111(4):1096–1098.

Beltaos, S. and Rajaratnam, N. (1973). Plane turbulent impinging jets. *Journal of Hydraulic Research*, 11(1):29–59.

Boelter, L. M. K. (1946). *Heat transfer notes*. Univ of California Press.

Boonloi, A. (2014). Effect of flow attack angle of V-ribs vortex generators in a square duct on flow structure, heat transfer, and performance improvement. *Modelling and Simulation in Engineering*, 2014:985612.

Bothien, M. R., Ciani, A., Wood, J. P., and Fruechtel, G. (2019). Toward decarbonized power generation with gas turbines by using sequential combustion for burning hydrogen. *Journal of Engineering for Gas Turbines and Power*, 141(12):121013.

Brack, S., Poser, R., and von Wolfersdorf, J. (2016). An approach to consider lateral heat conduction effects in the evaluation process of transient heat transfer measurements using TLC. *International Journal of Thermal Sciences*, 107:289–302.

Brdlik, P. and Savin, V. (1965). Heat transfer between an axisymmetric jet and a plate normal to the flow. *Journal of Engineering Physics*, 8(2):91–98.

Brezillon, J. and Gauger, N. (2004). 2D and 3D aerodynamic shape optimisation using the adjoint approach. *Aerospace Science and Technology*, 8(8):715–727.

Buttsworth, D. R., Elston, S. J., and Jones, T. V. (1998). Directional sensitivity of skin friction measurements using nematic liquid crystal. *Measurement Science and Technology*, 9(11):1856–1865.

Caggese, O., Gnaegi, G., Hannema, G., Terzis, A., and Ott, P. (2013). Experimental and numerical investigation of a fully confined impingement round jet. *International Journal of Heat and Mass Transfer*, 65:873–882.

Carlomagno, G. M. and Cardone, G. (2010). Infrared thermography for convective heat transfer measurements. *Experiments in Fluids*, 49:1187–1218.

Carslaw, H. and Jaeger, J. (1959). *Conduction of Heat in Solids (Second Edition)*. Oxford University Press, Oxford.

Chambers, A. C., Gillespie, D. R., Ireland, P. T., and Dailey, G. M. (2005). The effect of initial cross flow on the cooling performance of a narrow impingement channel. *Journal of Heat Transfer*, 127(4):358–365.

Chambers, A. C., Gillespie, D. R. H., Ireland, P. T., and Kingston, R. (2010). Enhancement of impingement cooling in a high cross flow channel using shaped impingement cooling holes. *Journal of Turbomachinery*, 132(2):021001.

Chen, L., Brakmann, R. G., Weigand, B., Rodriguez, J., Crawford, M., and Poser, R. (2017). Experimental and numerical heat transfer investigation of an impingement jet array with V-ribs on the target plate and on the impingement plate. *International Journal of Heat and Fluid Flow*, 68:126–138.

Cho, H. H., Wu, S. J., and Kwon, H. J. (1999). Local heat/mass transfer measurements in a rectangular duct with discrete ribs. *Journal of Turbomachinery*, 122(3):579–586.

Choi, M., Yoo, H. S., Yang, G., Lee, J. S., and Sohn, D. K. (2000). Measurements of impinging jet flow and heat transfer on a semi-circular concave surface. *International Journal of Heat and Mass Transfer*, 43(10):1811–1822.

Chyu, M. and Natarajan, V. (1996). Heat transfer on the base surface of threedimensional protruding elements. *International Journal of Heat and Mass Transfer*, 39(14):2925–2935.

Chyu, M. K., Hsing, Y. C., Shih, T. I.-P., and Natarajan, V. (1999). Heat transfer contributions of pins and endwall in pin-fin arrays: Effects of thermal boundary condition modeling. *Journal of Turbomachinery*, 121(2):257–263.

Chyu, M. K., Oluyede, E. O., and Moon, H.-K. (2007). Heat transfer on convective surfaces with pin-fins mounted in inclined angles. volume 4 of *Turbo Expo: Power for Land, Sea, and Air*, pages 861–869.

Claretti, R., Hossain, J., Harrington, J., Bernstein, J., Verma, S., and Kapat, J. (2013). Heat transfer study on multiple walls of an impingement channel with variable jet heights. In *ASME 2013 Heat Transfer Summer Conference*, volume 55492, page V003T08A002.

Cooper, T. E., Field, R. J., and Meyer, J. F. (1975). Liquid crystal thermography and its application to the study of convective heat transfer. *Journal of Heat Transfer*, 97(3):442–450.

Denholm, P., O'Connell, M., Brinkman, G., and Jorgenson, J. (2015). Overgeneration from solar energy in california. A field guide to the duck chart. Technical report, National Renewable Energy Lab (NREL), Golden, CO (United States).

Downs, J. P. and Fedock, J. A. (2012). Air cooled turbine airfoil with sequential impingement cooling. US Patent 8,322,988.

Downs, J. P. and Landis, K. K. (2009). Turbine cooling systems design: Past, present and future. In *Turbo Expo: Power for Land, Sea, and Air*, volume 3, pages 819–828.

Dubey, R. (2009). Microencapsulation technology and applications. *Defence Science Journal*, 59(1):82.

Economon, T. D. (2018). Simulation and Adjoint-based Design for Variable Density Incompressible Flows with Heat Transfer. In *2018 Multidisciplinary Analysis and Optimization Conference*. American Institute of Aeronautics and Astronautics.

Economon, T. D., Palacios, F., Copeland, S. R., Lukaczyk, T. W., and Alonso, J. J. (2016). Su2: An open-source suite for multiphysics simulation and design. *AIAA Journal*, 54(3):828–846.

Ekkad, S. V. and Han, J.-C. (2000). A transient liquid crystal thermography technique for gas turbine heat transfer measurements. *Measurement Science and Technology*, 11(7):957–968.

Ekkad, S. V., Ou, S., and Rivir, R. B. (2004). A transient infrared thermography method for simultaneous film cooling effectiveness and heat transfer coefficient measurements from a single test. *Journal of Turbomachinery*, 126(4):597–603.

Fechter, S., Terzis, A., Ott, P., Weigand, B., Von Wolfersdorf, J., and Cochet, M. (2013). Experimental and numerical investigation of narrow impingement cooling channels. *International Journal of Heat and Mass Transfer*, 67:1208–1219.

Fénot, M., Trinh, X. T., and Dorignac, E. (2019). Flow and heat transfer of a compressible impinging jet. *International Journal of Thermal Sciences*, 136:357–369.

Fiebig, M., Valencia, A., and Mitra, N. (1993). Wing-type vortex generators for fin-and-tube heat exchangers. *Experimental Thermal and Fluid Science*, 7(4):287–295.

Florschuetz, L., Truman, C., and Metzger, D. (1981). Streamwise flow and heat transfer distributions for jet array impingement with crossflow. In *ASME 1981 International Gas Turbine Conference and Products Show*.

Forthmann, E. (1934). Turbulent jet expansion. NACA Technical Memorandum 789, National Advisory Committee for Aeronautics.

Gaffuri, M., Ott, P., Naik, S., and Henze, M. (2021a). Experimental investigation of sequential narrow impingement channels for turbine cooling. In *Proceedings of 14th European Conference on Turbomachinery Fluid Dynamics & Thermodynamics*.

Gaffuri, M., Ott, P., Naik, S., and Henze, M. (2021b). Heat transfer enhancement in a double sequential impingement channel. In *Proceedings of ASME Turbo Expo 2021 Turbomachinery Technical Conference and Exposition*.

Gaffuri, M., Terzis, A., Ott, P., Retzko, S., and Henze, M. (2018). Evaluation of heat transfer coefficients for an impingement cooling cascade: Experimental challenges and preliminary results. In *XXIV Biannual Symposium on Measuring Techniques in Turbomachinery*.

Gallandat, N., Mutschler, R., Vernay, V., Yang, H., and Züttel, A. (2018). Experimental performance investigation of a 2 kW methanation reactor. *Sustainable Energy & Fuels*, 2(5):1101–1110.

Gau, C. and Chung, C. (1991). Surface curvature effect on slot-air-jet impingement cooling flow and heat transfer process. *Journal of Heat Transfer*, 113(4):858–864.

Gillespie, D. R. H., Wang, Z., Ireland, P. T., and Kohler, S. T. (1998). Full surface local heat transfer coefficient measurements in a model of an integrally cast impingement cooling geometry. *Journal of Turbomachinery*, 120(1):92–99.

Goldstein, R. and Cho, H. H. (1995). A review of mass transfer measurements using naphthalene sublimation. *Experimental Thermal and Fluid Science*, 10(4):416–434.

Goldstein, R., Chyu, M., and Hain, R. (1985). Measurement of local mass transfer on a surface in the region of the base of a protruding cylinder with a computer-controlled data acquisition system. *International Journal of Heat and Mass Transfer*, 28(5):977–985.

Goldstein, R. and Franchett, M. (1988). Heat transfer from a flat surface to an oblique impinging jet. *Journal of Heat Transfer*, 110(1):84–90.

Goldstein, R. J., Sobolik, K. A., and Seol, W. S. (1990). Effect of entrainment on the heat transfer to a heated circular air jet impinging on a flat surface. *Journal of Heat Transfer*, 112(3):608–611.

Gritsch, M., Schönwälder, D., and Estaun-Echavarren, C. (2006). Thermal performance of enhanced combustor liner impingement cooling schemes. In *Proceedings of the 11th International Symposium on Transport Phenomena and Dynamics of Rotating Machinery*.

Gutmark, E., Wolfshtein, M., and Wygnanski, I. (1978). The plane turbulent impinging jet. *Journal of Fluid Mechanics*, 88(4):737–756.

Gutmark, E. and Wygnanski, I. (1976). The planar turbulent jet. *Journal of Fluid Mechanics*, 73(3):465–495.

Hada, S., Takata, K., Iwasaki, Y., Yuri, M., and Masada, J. (2015). High-efficiency gas turbine development applying 1600 ˚C class "J" technology. *Mitsubishi Heavy Industries Technical Review*, 52(2):2.

Han, J. and Park, J. (1988). Developing heat transfer in rectangular channels with rib turbulators. *International Journal of Heat and Mass Transfer*, 31(1):183–195.

Han, J.-C. (2018). Advanced cooling in gas turbines 2016 - Max Jakob memorial award paper. *Journal of Heat Transfer*, 140(11). 113001.

Han, J.-C., Dutta, S., and Ekkad, S. (2012). *Gas turbine heat transfer and cooling technology*. CRC press.

Han, J. C., Zhang, Y. M., and Lee, C. P. (1991). Augmented heat transfer in square channels with parallel, crossed, and V-shaped angled ribs. *Journal of Heat Transfer*, 113(3):590–596.

Häring, M. (1995). *Experimentelle Untersuchung der örtlichen Wärmeübergangszahl an Gasturbinenschaufeln anhand der Sublimationstechnik im kompressiblen Strömungsbereich*. PhD thesis, EPFL, Lausanne, Switzerland.

Hartsel, J. (1972). Prediction of effects of mass-transfer cooling on the blade-row efficiency of turbine airfoils. In *10th Aerospace Sciences Meeting*, page 11.

He, C. and Liu, Y. (2018). Jet impingement heat transfer of a lobed nozzle: Measurements using temperature-sensitive paint and particle image velocimetry. *International Journal of Heat and Fluid Flow*, 71:111–126.

Heskestad, G. (1965). Hot-wire measurements in a plane turbulent jet. *Journal of Applied Mechanics*, 32(4):721–734.

Hippensteele, S. A., Russell, L. M., and Stepka, F. S. (1983). Evaluation of a method for heat transfer measurements and thermal visualization using a composite of a heater element and liquid crystals. *Journal of Heat Transfer*, 105(1):184–189.

Hisatomi, T. and Domen, K. (2019). Reaction systems for solar hydrogen production via water splitting with particulate semiconductor photocatalysts. *Nature Catalysis*, 2(5):387–399.

Ho, C.-M. and Gutmark, E. (1987). Vortex induction and mass entrainment in a small-aspect-ratio elliptic jet. *Journal of Fluid mechanics*, 179:383–405.

Hoogendoorn, C. (1977). The effect of turbulence on heat transfer at a stagnation point. *International Journal of Heat and Mass Transfer*, 20(12):1333–1338.

Horlock, J., Watson, D., and Jones, T. (2001). Limitations on gas turbine performance imposed by large turbine cooling flows. *J. Eng. Gas Turbines Power*, 123(3):487–494.

Hossain, J., Tran, L. V., Kapat, J. S., Fernandez, E., and Kumar, R. (2014). An experimental study of detailed flow and heat transfer analysis in a single row narrow impingement channel. In *Proceedings of ASME Turbo Expo: Power for Land, Sea and Air*, volume 5A: Heat Transfer.

Incropera, F. P., DeWitt, D. P., Bergman, T. L., Lavine, A. S., et al. (2006). *Fundamentals of heat and mass transfer*. Wiley New York, sixth edition.

Ireland, P. T. and Jones, T. V. (1987). The response time of a surface thermometer employing encapsulated thermochromic liquid crystals. *Journal of Physics E: Scientific Instruments*, 20(10):1195–1199.

Jones, R. B. (2017). Multiple wall impingement plate for sequential impingement cooling of a turbine hot part. US Patent 9,683,444.

Jones, R. B., Fedock, J. A., Goebel, G. E., Krueger, J. J., Rawlings, C. K., and Memmen, R. L. (2013). Industrial stator vane with sequential impingement cooling inserts. US Patent 8,500,405.

Jones, T. V. and Hippensteele, S. A. (1988). High-resolution heat-transfer-coefficient maps applicable to compound-curve surfaces using liquid crystals in a transient wind tunnel. NASA Technical Memorandum 89855, NASA.

Jonsson, M., Charbonnier, D., Ott, P., and von Wolfersdorf, J. (2008). Application of the transient heater foil technique for heat transfer and film cooling effectiveness measurements on a turbine vane endwall. In *Proceedings of ASME Turbo Expo: Power for Land, Sea and Air*, pages 443–453, Berlin, Germany.

Kiener, C., Kreutzer, A., Salcher, M., Hockley, C., and Küsters, Y. (2019). Burner tip for fitting in a burner with air duct system and fuel channel system. US Patent App. 16/472,575.

Kim, T., Jung, E. Y., Bang, M., Lee, C., Moon, H. K., and Cho, H. H. (2021). Heat transfer measurements for array jet impingement with castellated wall. In *ASME Turbo Expo 2021: Turbomachinery Technical Conference and Exposition*, pages GT2021–60201.

Kingsley-Rowe, J. R., Lock, G. D., and Owen, J. M. (2005). Transient heat transfer measurements using thermochromic liquid crystal: lateral-conduction error. *International Journal of Heat and Fluid Flow*, 26(2):256–263.

Klein, E. J. and Margozzi, A. P. (1969). Exploratory investigation on the measurement of skin friction by means of liquid crystals. NASA Technical Memorandum X-1774, NASA.

Kline, S. J. (1953). Describing uncertainty in single sample experiments. *Mechanical Engineering*, 75(1):3–8.

Kotsovinos, N. E. (1978). A note on the conservation of the axial momentum of a turbulent jet. *Journal of Fluid Mechanics*, 87(1):55–63.

Krueckels, J. and Widmer, M. (2013). Rotor blade and guide vane airfoil for a gas turbine engine. Patent number EP2886797B1.

Kuethe, A. M. (1933). *Investigations of turbulent mixing regions*. PhD thesis, California Institute of Technology.

Kuzia, A. (2019). Schub für neuen euro-fighter. *Flug Revue*, (8):60–62.

Kwak, J. S. (2008). Comparison of analytical and superposition solutions of the transient liquid crystal technique. *Journal of Thermophysics and Heat Transfer*, 22(2):290–295.

Kyprianidis, K. G. (2011). Future aero engine designs: An evolving vision. In Benini, E., editor, *The Impact of Climate Change on the United States Economy*, pages 3–24. IntechOpen, Rijeka.

Lee, J. J., Dutton, J. C., and Jacobi, A. M. (2007). Application of temperature-sensitive paint for surface temperature measurement in heat transfer enhancement applications. *Journal of Mechanical Science and Technology*, 21(8):1253–1262.

Ling, J. P. C. W., Ireland, P. T., and Turner, L. (2004). A technique for processing transient heat transfer, liquid crystal experiments in the presence of lateral conduction. *Journal of Turbomachinery*, 126(2):247–258.

Liu, K. (2017). A combustor assembly with impingement plates for redirecting cooling air flow in gas turbine engines. *WO patent*, (2017190967A1).

Liu, K. and Zhang, Q. (2020a). A novel multi-stage impingement cooling scheme — part I: Concept study. *Journal of Turbomachinery*, 142(12):121008.

Liu, K. and Zhang, Q. (2020b). A novel multi-stage impingement cooling scheme — part II: Design optimization. *Journal of Turbomachinery*, 142(12):121009.

Livesey, R. G. (1998). Flow of gases through tubes and orifices. In Lafferty, J. M., editor, *Foundations of Vacuum Science and Technology*, chapter 2, pages 81–140. Wiley & Sons.

Livingood, J. N. and Hrycak, P. (1973). Impingement heat transfer from turbulent air jets to flat plates: a literature survey. NASA Technical Memorandum X-2778, NASA.

Llucià, S., Terzis, A., Ott, P., and Cochet, M. (2015). Heat transfer characteristics of high crossflow impingement channels: Effect of number of holes. *Proceedings of the Institution of Mechanical Engineers, Part A: Journal of Power and Energy*, 229(5):560–568.

Lytle, D. and Webb, B. (1994). Air jet impingement heat transfer at low nozzle-plate spacings. *International Journal of Heat and Mass Transfer*, 37(12):1687–1697.

Ma, H., Wang, Z., Wang, L., Zhang, Q., and Bao, Y. (2016). Ramp heating in high-speed transient thermal measurement with reduced uncertainty. *Journal of Propulsion and Power*, 32(5):1190–1198.

Martin, H. (1977). Heat and mass transfer between impinging gas jets and solid surfaces. In *Advances in Heat Transfer*, volume 13, pages 1–60. Elsevier.

Martínez-Filgueira, P., Zulueta, E., Sánchez-Chica, A., Fernández-Gámiz, U., and Soriano, J. (2019). Multi-objective particle swarm based optimization of an air jet impingement system. *Energies*, 12(9):1627.

Mayhew, J. E., Baughn, J. W., and Byerley, A. R. (2003). The effect of freestream turbulence on film cooling adiabatic effectiveness. *International Journal of Heat and Fluid Flow*, 24(5):669–679.

McDaniel, C. and Webb, B. (2000). Slot jet impingement heat transfer from circular cylinders. *International Journal of Heat and Mass Transfer*, 43(11):1975–1985.

McKenzie, A. (1966). An investigation for flare dimensions for standard and annular air meters. *Report, CD Derby, UK, Rolls-Royce Plc.*

Medici, V., Salani, M., Nespoli, L., Giusti, A., Derboni, M., Vermes, N., Rizzoli, A. E., and Rivola, D. (2017). Evaluation of the potential of electric storage using decentralized demand side management algorithms. *Energy Procedia*, 135:203–209. 11th International Renewable Energy Storage Conference, IRES 2017, 14-16 March 2017, Düsseldorf, Germany.

Meginnis, G. B. (1972). Transpiration cooling. US Patent 3,698,834.

Menter, F. R. (1994). Two-equation eddy-viscosity turbulence models for engineering applications. *AIAA journal*, 32(8):1598–1605.

Meola, C. (2009). A new correlation of Nusselt number for impinging jets. *Heat Transfer Engineering*, 30(3):221–228.

Metzger, D., Florschuetz, L., Takeuchi, D., Behee, R., and Berry, R. (1979). Heat transfer characteristics for inline and staggered arrays of circular jets with crossflow of spent air. *Journal of Heat Transfer*, 101(3):526–531.

Metzger, D. E. (1962). Spot cooling and heating of surfaces with high velocity impinging air jets. Part 1. Slot jets on plane surfaces. Technical report, Standford Univ.

Metzger, D. E. and Larson, D. E. (1986). Use of melting point surface coatings for local convection heat transfer measurements in rectangular channel flows with 90-deg turns. *Journall of Heat Transfer*, 108(1):48–54.

Miller, N., Siw, S. C., Chyu, M. K., and Alvin, M. A. (2013). Effects of jet diameter and surface roughness on internal cooling with single array of jets. In *ASME Turbo Expo 2013: Power for Land, Sea, and Air*, page V03AT12A038.

Modak, M., Garg, K., and Sahu, S. K. (2017). Theoretical and experimental study on heat transfer characteristics of normally impinging two dimensional jets on a hot surface. *International Journal of Thermal Sciences*, 112:174–187.

Moffat, R. (1988). Describing the uncertainties in experimental results. *Experimental Thermal and Fluid Science*, 1:3–17.

Müller, B. (1998). *Low-Mach-number asymptotics of the Navier-Stokes equations*, pages 97–109. Springer Netherlands, Dordrecht.

Naik, S., Stephan, B., and Henze, M. (2021). GT36 turbine developement and full-scale validation. In *ASME Turbo Expo 2021: Turbomachinery Technical Conference and Exposition*, pages GT2021–60201.

Newton, P. J., Yan, Y., Stevens, N. E., Evatt, S. T., Lock, G. D., and Owen, J. (2003). Transient heat transfer measurements using thermochromic liquid crystal. part 1: An improved technique. *International Journal of Heat and Fluid Flow*, 24(1):14–22.

Obot, N. T. and Trabold, T. A. (1987). Impingement heat transfer within arrays of circular jets: Part 1—effects of minimum, intermediate, and complete crossflow for small and large spacings. *Journal of Heat Transfer*, 109(4):872–879.

Orcutt, M. (2016). Airplanes are getting lighter thanks to 3d-printed parts. *MIT Technology Review*.

Park, J., Han, J., Huang, Y., Ou, S., and Boyle, R. (1992). Heat transfer performance comparisons of five different rectangular channels with parallel angled ribs. *International Journal of Heat and Mass Transfer*, 35(11):2891–2903.

Park, J. S., Kim, K. M., Lee, D. H., Cho, H. H., and Chyu, M. (2010). Heat transfer in rotating channel with inclined pin-fins. *Journal of Turbomachinery*, 133(2). 021003.

Plank, W. L., Downs, J. P., and Fedock, J. A. (2012). Air cooled turbine airfoil with sequential impingement cooling. US Patent 8,167,537.

Poser, R. and von Wolfersdorf, J. (2009). Liquid crystal thermography for transient heat transfer measurements in complex internal cooling systems. *Heat Transfer Research*, 42:1–13.

Poser, R. and von Wolfersdorf, J. (2010). Transient liquid crystal thermography in complex internal cooling systems. In Coletti, F. and Arts, T., editors, *Internal cooling in turbomachinery*, number 2010-05 in VKI Lecture Series. von Karman Institute for Fluid Dynamics.

Promvonge, P. and Thianpong, C. (2008). Thermal performance assessment of turbulent channel flows over different shaped ribs. *International Communications in Heat and Mass Transfer*, 35(10):1327–1334.

Rao, Y. (2018). Heat transfer from arrays of impinging jets with large jet-to-jet spacing. *Journal of Heat Transfer*, 140(7):072201 (10 pages).

Rao, Y., Liu, Y., and Wan, C. (2018). Multiple-jet impingement heat transfer in double-wall cooling structures with pin fins and effusion holes. *International Journal of Thermal Sciences*, 133:106–119.

Ratto, L., Satta, F., and Tanda, G. (2018). An experimental and numerical study of endwall heat transfer in a turbine blade cascade including tangential heat conduction analysis. *Heat and Mass Transfer*, 54(6):1627–1636.

Reda, D. C., Wilder, M. C., Farina, D. J., and Zilliac, G. (1997). New methodology for the measurement of surface shear stress vector distributions. *AIAA Journal*, 35(4):608–614.

Ricklick, M., Kapat, J., and Heidmann, J. (2010). Sidewall effects on heat transfer coefficient in a narrow impingement channel. *Journal of Thermophysics and Heat Transfer*, 24(1):123–132.

Ruden, P. (1933). Turbulente ausbreitungsvorgänge im freistrahl. *Naturwissenschaften*, 21:375–378.

Sang-Joon, L., Jung-Ho, L., and Dae-Hee, L. (1994). Local heat transfer measurements from an elliptic jet impinging on a flat plate using liquid crystal. *International Journal of Heat and Mass Transfer*, 37(6):967–976.

Sarkar, D., Jain, A., Goldstein, R., and Srinivasan, V. (2016). Corrections for lateral conduction error in steady state heat transfer measurements. *International Journal of Thermal Sciences*, 109:413–423.

Satta, F. and Tanda, G. (2014). Measurement of local heat transfer coefficient on the endwall of a turbine blade cascade by liquid crystal thermography. *Experimental Thermal and Fluid Science*, 58:209–215.

Schack, A. (1969). *Der industrielle Wärmeübergang*. Verlag Stahleisen.

Schmid, J., Gaffuri, M., Terzis, A., Ott, P., and von Wolfersdorf, J. (2021). Transient liquid crystal thermography using a time varying surface heat flux. *International Journal of Heat and Mass Transfer*, 179:121718.

Schultz, D. L. and Jones, T. (1973). Heat-transfer measurements in short-duration hypersonic facilities. Technical report, Advisory Group for Aerospace Research and Development.

Siebold, M. (2019). Additive manufacturing for serial production of high-performance metal parts. *Mechanical Engineering*, 141(05):49–50.

Sparrow, E. and Lovell, B. (1980). Heat transfer characteristics of an obliquely impinging circular jet. *Journal of Heat Transfer*, 102(2):202–209.

Sparrow, E. and Molki, M. (1982). Effect of a missing cylinder on heat transfer and fluid flow in an array of cylinders in cross-flow. *International Journal of Heat and Mass Transfer*, 25(4):449–456.

Squire, H. and Trouncer, J. (1944). Round jets in a general stream. Technical Report 1974, Aeronautical Research Council, London, UK.

Stasiek, J. A. and Kowalewski, T. A. (2002). Thermochromic liquid crystals applied for heat transfer research. *Opto - Electronics Review*, Vol. 10, No. 1:1–10.

Sun, G. and Wang, S. (2019). A review of the artificial neural network surrogate modeling in aerodynamic design. *Proceedings of the Institution of Mechanical Engineers, Part G: Journal of Aerospace Engineering*, 233(16):5863–5872.

Tembhurne, S., Nandjou, F., and Haussener, S. (2019). A thermally synergistic photoelectrochemical hydrogen generator operating under concentrated solar irradiation. *Nature Energy*, 4(5):399–407.

Terzis, A. (2014). *Detailed heat transfer distributions of narrow impingement channels for integrally cast turbine airfoils*. PhD thesis.

Terzis, A., Bontitsopoulos, S., Ott, P., von Wolfersdorf, J., and Kalfas, A. I. (2016a). Improved accuracy in jet impingement heat transfer experiments considering the layer thicknesses of a triple thermochromic liquid crystal coating. *Journal of Turbomachinery*, 138(2):021003.

Terzis, A., Ott, P., Cochet, M., von Wolfersdorf, J., and Weigand, B. (2015). Effect of varying jet diameter on the heat transfer distributions of narrow impingement channels. *Journal of Turbomachinery*, 137(2).

Terzis, A., Ott, P., von Wolfersdorf, J., Weigand, B., and Cochet, M. (2014a). Detailed heat transfer distributions of narrow impingement channels for cast-in turbine airfoils. *Journal of Turbomachinery*, 136(9):091011. 091011.

Terzis, A., Skourides, C., Ott, P., von Wolfersdorf, J., and Weigand, B. (2016b). Aerothermal investigation of a single row divergent narrow impingement channel by particle image velocimetry and liquid crystal thermography. *Journal of Turbomachinery*, 138(5):051003.

Terzis, A., von Wolfersdorf, J., Weigand, B., and Ott, P. (2012). Thermocouple thermal inertia effects on impingement heat transfer experiments using the transient liquid crystal technique. *Measurement Science and Technology*, 23(11):115303.

Terzis, A., Wagner, G., von Wolfersdorf, J., Ott, P., and Weigand, B. (2014b). Hole staggering effect on the cooling performance of narrow impingement channels using the transient liquid crystal technique. *Journal of Heat Transfer*, 136(7).

Thema, M., Bauer, F., and Sterner, M. (2019). Power-to-gas: Electrolysis and methanation status review. *Renewable and Sustainable Energy Reviews*, 112:775–787.

Torbatinezhad, A., Rahimi, M., Ranjbar, A., and Gorzin, M. (2021). Performance evaluation of PV cells in HCPV/T system by a jet impingement/mini-channel cooling scheme. *International Journal of Heat and Mass Transfer*, 178:121610.

Torkaman, A., Vogel, G., and Houck, L. (2021). Design, developement and vallidation of additively manufactured first stage turbine vane for class F industrial gas turbine. In *ASME Turbo Expo 2021: Turbomachinery Technical Conference and Exposition*, pages GT2021–60201.

Tran, L. V. and Slabaugh, C. D. (2019). On correlated measurements in the transient thermochromic liquid crystals technique with multiple indicators. *International Journal of Heat and Mass Transfer*, 137:229–241.

Uysal, U., Li, P. W., Chyu, M. K., and Cunha, F. J. (2006). Heat transfer on internal surfaces of a duct subjected to impingement of a jet array with varying jet hole-size and spacing. *Journal of Turbomachinery*, 128(1):158–165.

Van der Meer, T. H. (1991). Stagnation point heat transfer from turbulent low reynolds number jets and flame jets. *Experimental Thermal and Fluid Science*, 4(1):115–126.

Van Treuren, K. W., Wang, Z., Ireland, P., Jones, T. V., and Kohler, S. (1996). Comparison and prediction of local and average heat transfer coefficients under an array of inline and staggered impinging jets. In *Turbo Expo: Power for Land, Sea, and Air*, volume 78750, page V004T09A005.

Vandervort, C., Leach, D., Walker, D., and Sasser, J. (2019). Commercialization and fleet experience of the 7/9HA gas turbine combined cycle. In *Turbo Expo: Power for Land, Sea, and Air*, volume 58608, page V003T08A006.

VanFossen, G. J. (1982). Heat-transfer coefficients for staggered arrays of short pin fins. *Journal of Engineering for Power*, 104(2):268–274.

Viskanta, R. (1993). Heat transfer to impinging isothermal gas and flame jets. *Experimental Thermal and Fluid Science*, 6(2):111–134.

Vogel, G., Graf, A., von Wolfersdorf, J., and Weigand, B. (2003). A novel transient heater-foil technique for liquid crystal experiments on film-cooled surfaces. *Journal of Turbomachinery*, 125(3):529–537.

Vogel, G. and Weigand, B. (2001). A new evaluation method for transient liquid crystal experiments. *Proceedings of the 35th National Heat Transfer Conference*.

von Wolfersdorf, J. (2007). Influence of lateral conduction due to flow temperature variations in transient heat transfer measurements. *International Journal of Heat and Mass Transfer*, 50(5):1122–1127.

Waidmann, C., Poser, R., Göhring, M., and von Wolfersdorf, J. (2018). First operation of a rotating test rig for transient thermochromic liquid crystal heat transfer experiments. In *XXIV Biannual Symposium on Measuring Techniques in Turbomachinery*.

Waidmann, C., Poser, R., and von Wolfersdorf, J. (2013). Application of thermochromic liquid crystal mixtures for transient heat transfer measurements. In *10th European Conference on Turbomachinery Fluid dynamics & Thermodynamics*. European Turbomachinery Society.

Walz, D. R. (1964). Spot cooling and heating of surfaces with high velocity impinging air jets. Part 2. Circular jets on plane and curved surfaces, slot jets on curved surfaces. Technical report, Stanford Univ.

Ward, J., Oladiran, M., and Hammond, G. (1991). Effect of nozzle inclination on jet impingement heat transfer in a confined cross flow. *Fundamentals of Forced Convective Heat Transfer*, pages 25–31.

Weigand, B. and Spring, S. (2011). Multiple jet impingement - a review. *Heat Transfer Research*, 42(2).

Winterton, R. H. (1998). Where did the Dittus and Boelter equation come from? *International Journal of Heat and Mass Transfer*, 41(4-5):809–810.

Wright, L. M., Fu, W.-L., and Han, J.-C. (2004). Thermal performance of angled, V-shaped, and W-shaped rib turbulators in rotating rectangular cooling channels (AR=4:1). *Journal of Turbomachinery*, 126(4):604–614.

Wulf, C., Linßen, J., and Zapp, P. (2018). Review of power-to-gas projects in Europe. *Energy Procedia*, 155:367–378.

Xing, J., Luo, Y., and Gao, Z. (2020). A global optimization strategy based on the Kriging surrogate model and parallel computing. *Structural and Multidisciplinary Optimization*, pages 1–13.

Zuckerman, N. and Lior, N. (2006). Jet impingement heat transfer: Physics, correlations, and numerical modeling. *Advances in Heat Transfer*, 39:565–631.

Michele Gaffuri
Route Aloys-Fauquez 109
1018 Lausanne
email: michele.gaffuri@epfl.ch

Nationality Swiss
Year of birth 1980

Work Experience

2017 – present	**Doctoral assistant** at the **Doctoral Program in Energy**, Swiss Federal Institute of Technology (EPFL), Lausanne, Switzerland • ExPerimental assessment of novel jet cooling configurations for gas turbine blades and vanes
2015 – 2017	**Scientist** at the Group of Thermal Turbomachinery (GTT), **Swiss Federal Institute of Technology (EPFL)**, Lausanne, Switzerland • Design and numerical analysis of mechanical heart valves
2013 – 2016	**Design Engineer** at AEDS Sàrl, Martigny-Croix, Switzerland • Design and analysis of aircraft systems
2010 – 2013	**Research engineer** at the **German Aerospace Centre (DLR)**, Brunswick, Germany • Multidisciplinary design and optimisation of transport and supersonic aircraft • Design of high-lift systems
2005 – 2010	**Aerodynamic Engineer** at the Numerical Engineering Laboratory (LIN), **Swiss Federal Institute of Technology (EPFL)**, Lausanne, Switzerland • Numerical aerodynamic analysis of supersonic aircraft, (re-)entry capsules and suborbital planes

Education

2005	**Master of Science** in mechanical engineering at EPFL, Lausanne, Switzerland
2000 – 2005	**Mechanical engineering studies** at EPFL, Lausanne, Switzerland.
1995 – 1999	**High school** at Liceo Cantonale, Mendrisio, Switzerland

Computing Skills

OS	Linux, Windows
Productivity	MS Office, Libreoffice, Latex
Programming	Matlab, python and bash, LabVIEW intermediate level in C, Fortran basic skills in C++, julia
3D modeling	CATIA, SolidWorks, I-DEAS, FreeCAD
Grid generators	ICEM-CFD, Solar, Centaur
Simulations	ANSYS, COMSOL Multiphysics, TAU, NSMB, CFD++, SU2

Personal

Languages	**Italian**	Mother tongue
	English	Very good knowledge (written and oral)
	French	Very good knowledge (written and oral)
	German	Good knowledge (written and oral)
	Spanish	Basic skills
Other	**Sport**	Football, cycling, running, hiking

PUBLICATIONS

J. Schmid, M. Gaffuri, A. Terzis, P. Ott, J. von Wolfersdorf, ***Transient Liquid Crystal Thermography Using a Time Varying Surface Heat Flux***, *International Journal of Heat and Mass Transfer*. 2021-07-28.

M. Gaffuri, P. Ott, S. Naik, M. Henze, ***Heat Transfer Enhancement in a Double Sequential Impingement Channel***, ASME Turbo Expo 2021, virtual, online, June 7-11, 2021.

M. Gaffuri, P. Ott, S. Naik, M. Henze, ***Experimental investigation of sequential narrow impingement channels for turbine cooling***, 14th European Confernce on Turbomachinery Fluid Dynamics & Thermodynamics, Gdansk, Pologne, April 12-16, 2021.

J. Schmid, M. Gaffuri, A. Terzis, P. Ott, J. von Wolfersdorf, ***Accuracy improvement of the transient heater foil technique for heat transfer tests: preliminary results***, XXV Biannual Symposium on Measuring Techniques in Turbomachinery, Santorini, GR, September 21-2, 2020.

M. Gaffuri, A. Terzis, P. Ott, ***Narrow Impingement Channels: Recent Advancements and Future Directions***, ETC13 – European Turbomachinery Conference, Lausanne, CH, April 8-12, 2019.

M. Gaffuri, A. Terzis, P. Ott, S. Retzko, M. Henze, ***Evaluation of Heat Transfer Coefficients for an Impingement Cooling Cascade: Experimental Challenges and Preliminary Results***, XXIV Biannual Symposium on Measuring Techniques in Turbomachinery, Prague, CZE, August 29-31, 2018.

M. Schuermann, M. Gaffuri, P. Horst, ***Multidisciplinary Pre-Design of Supersonic Aircraft***, CEAS Aeronautical Journal, Volume 6, Issue 2, pp 207–216, 2015.

M. Schuermann, M. Gaffuri, P. Horst, ***Extensions to aircraft pre-design for supersonic aircraft***, 52nd Aerospace Sciences Meeting and Exhibition, National Harbor, Maryland (USA), 2014.

M. Gaffuri, J. Brezillon, D. Kwak, K. Ohira, G. Carrier, ***Comparison of CFD solvers for low speed vortex dominated flows***, 31st AIAA Applied Aerodynamics Conference, S. Diego (USA), 2013.

D. Kwak, K. Ohira M. Gaffuri, and J. Brezillon, ***CFD Validation for the Supersonic Transport Configuration at Low-Speed and High Alpha Flight Condition***, 31st AIAA Applied Aerodynamics Conference, S. Diego (USA), 2013.

K. Ohira, D. Kwak, J. Brezillon and M. Gaffuri, ***Investigation of Eddy Viscosity Turbulence Models on the Vortical Flow over the Highly Swept and Low Aspect Ratio Wing***, 51st AIAA Aerospace Sciences Meeting, Grapevine (USA), 2013.

J.-E. Lombard, P. Leyland, M. Gaffuri, and Y. Wohlhauser, ***Vortical Flow Patterns for High Lift for High Speed Aircraft Concepts***, 5th European Conference for Aeronauticas and Space Sciences (EUCASS), Munich, Germany, July 1-5, 2013.

M. Gaffuri and J. Brezillon, ***High lift devices design of supersonic transport aircraft based on 3D computational fluid dynamics***, 6th European Congress on Computational Methods in Applied Sciences and Enegeneering (ECCOMAS), Vienna (Austria), 2012.

D. Kwak, M. Gaffuri, K. Ohira and J. Brezillon, ***Numerical Study of the Reynolds Number Effect on Low Aspect Ratio Wings at Low Speed***, 28th International Congress of the Aeronautical Sciences (ICAS), Brisbane (Australia), 2012.

M. Gaffuri and J. Brezillon, ***Unstructured mesh capabilities for supersonic wing design at low speed conditions***, ECCOMAS Thematic Conference CFD & OPTIMIZATION, Antalya (Turkey), 2011.

R. Savajano, R. Sobbia, M. Gaffuri, and P. Leyland, ***Reduced Chemical Kinetic Model for Titan Entries***, International Journal of Chemical Engineering, 2011.

R. von Kaenel, S. Sanchi, J.B. Vos, M. Gaffuri, P. Leyland, T. Walloschek, P. Binetti, ***IXV CFD simulations for wind tunnel rebuilding and extrapolation to flight***, Sixth European Symposium on Aerothermodynamics for Space Vehicles, Versailles (France), 2008.